CONTROLLED SOURCE SEISMIC INVESTIGATION OF THE CRUSTAL STRUCTURE BENEATH EREBUS VOLCANO AND ROSS ISLAND, ANTARCTICA

by

Shoba Maraj

Submitted in Partial Fulfillment

of the Requirements for the Degree of

Master of Science in Geophysics (Solid Earth)

New Mexico Institute of Mining and Technology

Socorro, New Mexico

June, 2011

ABSTRACT

Ross Island, Antarctica, is located within the intraplate West Antarctic Rift System (WARS), which is an area of active crustal extension. Mount Erebus, located on Ross Island is one of the few volcanoes on Earth that has a persistent, convecting lava lake. Marine geophysical observations north of Ross Island have identified the north-south trending Terror Rift within the older and broader Victoria Land Basin, which is a component of the WARS. Mount Erebus and Ross Island are circumstantially associated with the Terror Rift and its thin (∼20 km) crust. The nature and extent of the Terror Rift in controlling the evolution of Ross Island volcanism and the on-going eruptive activity of Erebus volcano are unknown.

A controlled-source seismic experiment (Tomo-Erebus, TE) was undertaken during the 2008-2009 Austral summer field season to examine the shallow magmatic system beneath Erebus volcano (TE-3D) and the deeper crustal structure beneath Ross Island (TE-2D). This work investigates the TE-2D component, which was designed to produce a two-dimensional *P* wave velocity model along a 76 km east-west profile across Ross Island. For TE-2D, 21 seismic recorders (Ref Tek 130) with three-component 4.5 Hz geophones (Sercel L-28-3D) were deployed along a 77-km east-west line between Capes Royds and Crozier. For TE-3D, 79 similar instruments were deployed in a 3 x 3 km square around the crater of Erebus, an array of 8 permanent short-period and broadband sensors and 23 three-component sensors (Guralp CMG-40T, 30s-100 Hz) were positioned around the flanks and summit of Erebus. Sixteen chemical shots were used, of which fifteen shots used between 75 to 600 kg of ANFO, with the largest shots at the ends of the profile. The remaining shot was detonated in the sea (McMurdo Sound) using 200 kg of dynamite. Although the station spacing is $\sim$4 km, the data generally have a high signal to noise ratio with clear first arrivals across the array.

Forward modeling ray tracing was used to develop 1D and 2D *P* wave velocity models. 1D velocity models developed for 3 sources show up to $\sim$3 layers of increasing velocity down to depths of $\sim$6 km depth. Both the 1D models and the models from previous work were used as the starting model for *P* wave tomographic inversion. While the tomography models show general agreement to the 1D, 2D and previous models, robust features not seen in the other models are resolved. These include anomalously low velocities at very shallow depths below the summit of the volcano, as well as an area of relatively high velocity below Mount Terror. The low velocities in the summit region approach the velocity of phonolitic lava and may be indicative of a shallow magma chamber. While the inversion models have low resolution due to limited raypath coverage, they will be useful models for any future inversion modeling conducted on the island and demonstrate the need for future data collection in the Ross Island region.

Keywords: Mount Erebus; Ross Island; Seismic Tomography

ACKNOWLEDGMENTS

I would like to thank my advisor, Rick Aster, for all of his help. I would also like to thank the rest of my committee, Cathy Snelson and Phil Kyle for their guidance over the last two years.

This research was funded by NSF grants ANT-0538414 and ANT-0838817. All instrumentation was provided by IRIS PASSCAL.

Thanks to all of my fellow graduate students for their support, both with work and otherwise, especially Hunter Knox, Jonathan MacCarthy, Julien Chaput, Melissa Kammerer, Maya El Hariri and Rebecca Garcia. Lastly, Erwann, my family and friends.

This thesis was typeset with LaTeX[1] by the author.

[1] The LaTeX document preparation system was developed by Leslie Lamport as a special version of Donald Knuth's TeX program for computer typesetting. TeX is a trademark of the American Mathematical Society. The LaTeX macro package for the New Mexico Institute of Mining and Technology thesis format was written for the Tech Computer Center by John W. Shipman.

CONTENTS

LIST OF TABLES **v**

LIST OF FIGURES **vi**

INTRODUCTION **1**

1. BACKGROUND **3**

1.1 Previous Geochemical Studies 3

1.2 Previous Geophysical Studies 4

2. DATA COLLECTION **9**

2.1 2007-2008 Field Season 9

2.2 2008-2009 Field Season 10

3. METHODS **14**

3.1 1D Forward Models 14

3.2 2D Forward Models 19

3.3 Tomography 21

4. DISCUSSION **35**

CONCLUSION **42**

REFERENCES **45**

A. SHOT DATA **48**

B. BROADBAND STATION DATA **49**

C. SHORT-PERIOD STATION DATA **50**

D. SHOT GATHERS **53**

E. TOMOGRAPHIC INVERSION CODE **62**

F. TOMOGRAPHY IMAGES **70**

LIST OF TABLES

2.1 Shot information from the 2007-2008 field season. 10

3.1 Uncertainty in time corresponding to weights assigned during picking. 24

LIST OF FIGURES

1.1 Map of Ross Sea region. Volcanics are shown in dark red. The Terror Rift, stretching from Mount Morning (MM), and Ross Island can be seen within the Victoria Land Basin. The Eastern and Central Basins are also indicated on the map (*Worner*, 1999). 5

1.2 *Dibble et al.* (1994) model showing velocity structure below Mount Erebus. Cross section goes from New Harbour through Erebus and Windless Bight. This model is derived from seismic surveys conducted below McMurdo Sound by *McGinnis et al.* (1983) and *Northey et al.* (1975), a seismic survey by *Beaudoin et al.* (1992) of the Ross Ice Shelf, a seismic survey by *Stern et al.* (1991) of Windless Bight, and several studies of isostatic subsidence. 6

1.3 Map of Ross Island. Black line is the location of the cross-section from Figure 1.2. Shots locations are shown as red stars, and stations used are shown as black triangles. 7

2.1 Map of Ross Island showing the station deployment. All ETS stations were deployed during the 2008-2009 field season, ETB stations were deployed during the 2007-2008 field season, and Permanent Network stations were deployed during the 1999-2000 field season. The TE-2D survey used the 21 ETS stations that are along the 76 km East-West profile across the island. 11

2.2 Zoomed in map of Mount Erebus showing the station deployment. Twelve of the sixteen shots used during the 2008-2009 field season can be seen, as well as the configuration of 79 ETS instruments that were deployed primarily for the TE-3D experiment. 12

3.1 1D Forward Model from Shot 4001 Cape Crozier. The best fit solution has 4 layers, with an initial layer that is just over 2 km thick, and has a velocity of a just over 3 km/s. The second layer is about 1 km thick and has a velocity of 4 km/s. The third layer is 5 km thick and has a velocity of 6 km/s that increases with depth. The fourth layer begins at about 9 km depth with a velocity of more than 8 km/s. 15

3.2 1D Forward Model from Shot 4002 Cape Royds. The best fit to the time-depth data resulted in a model that has an initial velocity of 3 km/s from the surface to 2 km depth. The second layer was from 2 4 km depth and had a velocity of 3.5 km/s. The third layer had a depth of roughly 4 8 km, with a velocity of 5 km/s. The last layer began at 8 km/s and the velocity of this layer slowly increased with depth. 16

3.3 1D Forward Model from Shot 4003 Crozier 2. Even though this was very close to the Cape Crozier shot, there are large differences in the near surface profile. The energy from the Cape Crozier shot did not carry to all of the seismic recorders and so this location was re-shot, using more explosives. There is a velocity of just below 3 km/s down to a depth of 1 km. There is a velocity of 5 km/s between the depths of 1-3 km, and a velocity of 5.5 km/s from the depths of 3 km 6.5 km, and then a velocity of 6.5 km/s from the depth of 6.5 km down. 17

3.4 1D Forward Model East and West from Shot 4004 FANG. These models were split up into west and east of the shot location. The east model shows velocities of just below 3 km/s down to 1 km below the surface. From 1 3 km depth, the second layer has a velocity of almost 5 km/s. A third layer of extends from 3 6.5 km below the surface with a velocity of 5.5 km/s. Below this depth we have a layer at a constant velocity of 6.5 km/s. For the west model, there was a velocity of just below 4 km/s down to a depth of 4 km, and then a constant velocity of 5 km/s. 18

3.5 2D Forward Model across Ross Island. Three shots were used to create this model, which are represented by red stars. West shot is at Cape Royds, shot at summit of Erebus volcano is at Fang, and east shot is Cape Crozier shot. 20

3.6 Travel-time fits for 2D forward model showing synthetic and observed data from the Cape Royds shot (blue) and the Cape Crozier shot(green). Only two of the three shots used are shown for simplicity. Straight lines represent the travel-time information from rays shot through the model, while the points represent the observed travel time data. 21

3.7 Stations that roughly lie along the East-West profile. These stations include the ETB, ETS and Permanent Network stations that lie along the east-west transect. All of these stations were considered for the tomography 24

3.8 Distribution of raypaths of station-shot pairs from 3.7 in map view. Only raypaths within 2 km perpedicular to transect or less than 20 $^\circ$ from the transect were used. All raypaths used are shown in red, and all raypaths not used are shown as black lines. Ultimately, 363 raypaths were used. 25

3.9 Gradient velocity model showing circular input raypaths as white lines. Velocity gradient is shown in km/s. Topography of Ross Island is shown as a black line, and areas without raypath coverage are shown in gray. 26

3.10 RMS Error for input gradient model. Input gradient model is based on the work of *Dibble et al.* (1994). The starting RMS for raypaths through this model is 0.634, which represents the residual between observed travel times (red) and calculated travel times (blue) . . . 27

3.11 L-Curve showing subtle corner at $\alpha = 586.5514$. Open circles represent values of the regularization parameter whose models do not converge. 28

3.12 Best Model from tomographic inversion. Velocities are shown in km/s. 30

3.13 RMS Error between observed and calculated travel times for α = 586.5514. Again, the observed travel times are in red, and calculated travel times are shown in blue. 31

3.14 Velocity perturbation that was superimposed over gradient velocity model in order to do checkerboard test. Input velocity pertubation is also a velocity gradient. 32

3.15 Input Checkerboard model with 35 km checkers, that was composed of the velocity perturbations from Figure 3.14 superimposed over the velocity gradient model of Figure 3.9. 33

3.16 Result of checkerboard inversion using 35 km checkers for $\alpha = 462$. Evidence of checkerboard is only seen in the near surface, especially in areas that had the densest raypath coverage. 34

4.1 Best tomography model. (a) shows very low velocities of less than 3 km/s at the summit of Erebus volcano, (b) relatively high velocities below Mount Terror. Both features are in areas of high raypath coverage, and thus are the among the best resolved areas of the model. 36

4.2 Comparison of velocity profiles from the 2D tomographic images (red line) with the *Dibble et al.* (1994) model (blue line) at Erebus. The models are identical from above 1 km above sea level to 7 km below sea level. The summit velocities of this study are much lower than the previous model. 39

4.3 Comparison of velocity profiles from this study with studies from Vesuvius. The short-dashed line is from *Vilardo et al.* (1996), the long-dashed line is from *De Natale et al.* (1998) and *Capuano et al.* (1999), the solid line is from *Lomax et al.* (2001). The red line is the 1D profile east of the Fang shot, and the blue line is the 1D profile west of the Fang shot. 41

4.4 Comparison between the 2D and tomography models. In areas of poor raypath coverage, the inversion model is comparable to the 2D model. However, in areas of higher raypath coverage, such as in the near surface, especially in the summit region of Mount Erebus, the resolution greatly increases. 44

D.1 Shot gather from the Windless Bight (4000) shot 53

D.2 Shot gather from the Cape Crozier (4001) shot 54

D.3 Shot gather from the Cape Royds (4002) shot 54

D.4 Shot gather from the Crozier 2 (4003) shot 55

D.5 Shot gather from the FANG (4004) shot 55

D.6 Shot gather from the Cones2 (4005) shot 56

D.7 Shot gather from the Cones (4006) shot 56

D.8 Shot gather from the CORR13 (4007) shot 57

D.9 Shot gather from the Transw 2 (4008) shot 57

D.10 Shot gather from the Sunshine Valley Corner SW (4009) shot 58

D.11 Shot gather from the HoleH (4010) shot 58

D.12 Shot gather from the Stinky (13) (4011) shot 59

D.13 Shot gather from the Black (19) (4012) shot 59

D.14 Shot gather from the Tower (17) (4013) shot 60

D.15 Shot gather from the Fog (15) (4014) shot 60

D.16 Shot gather from the Stuck (11) (4015) shot 61

F.1 Residual Norm versus number of Iterations 70

F.2 Solution Seminorm versus number of Iterations 71

F.3 RMS Error for α = 1634.9197, First Iteration 72

F.4 Velocity model for α = 1634.9197, First Iteration 72

F.5 RMS Error for α = 1634.9197, Second Iteration 73

F.6 Velocity model for α = 1634.9197, Second Iteration 73

F.7 RMS Error for α = 1634.9197, Third Iteration 74

F.8 Velocity model for α = 1634.9197, Third Iteration 74

F.9 RMS Error for α = 1160.6255, First Iteration 75

F.10 Velocity model for α = 1160.6255, First Iteration 75

F.11 RMS Error for α = 1160.6255, Second Iteration 76

F.12 Velocity model for α = 1160.6255, Second Iteration 76

F.13 RMS Error for α = 1160.6255, Third Iteration 77

F.14 Velocity model for α = 1160.6255, Third Iteration 77

F.15 RMS Error for α = 824.562, First Iteration 78

F.16 Velocity model for α = 824.562, First Iteration 78

F.17 RMS Error for α = 824.562, Second Iteration 79

F.18 Velocity model for $\alpha = 824.562$, Second Iteration 79
F.19 RMS Error for $\alpha = 824.562$, Third Iteration 80
F.20 Velocity model for $\alpha = 824.562$, Third Iteration 80
F.21 RMS Error for $\alpha = 586.5514$, First Iteration 81
F.22 Velocity model for $\alpha = 586.5514$, First Iteration 81
F.23 RMS Error for $\alpha = 586.5514$, Second Iteration 82
F.24 Velocity model for $\alpha = 586.5514$, Second Iteration 82
F.25 RMS Error for $\alpha = 586.5514$, Third Iteration 83
F.26 Velocity model for $\alpha = 586.5514$, Third Iteration 83
F.27 RMS Error for $\alpha = 417.8337$, First Iteration 84
F.28 Velocity model for $\alpha = 417.8337$, First Iteration 84
F.29 RMS Error for $\alpha = 417.8337$, Second Iteration 85
F.30 Velocity model for $\alpha = 417.8337$, Second Iteration 85
F.31 RMS Error for $\alpha = 417.8337$, Third Iteration 86
F.32 Velocity model for $\alpha = 417.8337$, Third Iteration 86
F.33 RMS Error for $\alpha = 297.9803$, First Iteration 87
F.34 Velocity model for $\alpha = 297.9803$, First Iteration 87
F.35 RMS Error for $\alpha = 297.9803$, Second Iteration 88
F.36 Velocity model for $\alpha = 297.9803$, Second Iteration 88
F.37 RMS Error for $\alpha = 297.9803$, Third Iteration 89
F.38 Velocity model for $\alpha = 297.9803$, Third Iteration 89
F.39 RMS Error for $\alpha = 212.5295$, First Iteration 90

F.40 Velocity model for $\alpha = 212.5295$, First Iteration 90
F.41 RMS Error for $\alpha = 212.5295$, Second Iteration 91
F.42 Velocity model for $\alpha = 212.5295$, Second Iteration 91
F.43 RMS Error for $\alpha = 212.5295$, Third Iteration 92
F.44 Velocity model for $\alpha = 212.5295$, Third Iteration 92
F.45 RMS Error for $\alpha = 151.4196$, First Iteration 93
F.46 Velocity model for $\alpha = 151.4196$, First Iteration 93
F.47 RMS Error for $\alpha = 151.4196$, Second Iteration 94
F.48 Velocity model for $\alpha = 151.4196$, Second Iteration 94
F.49 RMS Error for $\alpha = 151.4196$, Third Iteration 95
F.50 Velocity model for $\alpha = 151.4196$, Third Iteration 95
F.51 RMS Error for $\alpha = 107.7181$, First Iteration 96
F.52 Velocity model for $\alpha = 107.7181$, First Iteration 96
F.53 RMS Error for $\alpha = 107.7181$, Second Iteration 97
F.54 Velocity model for $\alpha = 107.7181$, Second Iteration 97
F.55 RMS Error for $\alpha = 107.7181$, Third Iteration 98
F.56 Velocity model for $\alpha = 107.7181$, Third Iteration 98
F.57 RMS Error for $\alpha = 76.5233$, First Iteration 99
F.58 Velocity model for $\alpha = 76.5233$, First Iteration 99
F.59 RMS Error for $\alpha = 76.5233$, Second Iteration 100
F.60 Velocity model for $\alpha = 76.5233$, Second Iteration 100
F.61 RMS Error for $\alpha = 76.5233$, Third Iteration 101

F.62 Velocity model for $\alpha = 76.5233$, Third Iteration 101

This thesis is accepted on behalf of the faculty of the Institute by the following committee:

Richard Aster, Advisor

I release this document to the New Mexico Institute of Mining and Technology.

Shoba Maraj Date

INTRODUCTION

Ross Island is located in the West Antarctic Rift System, which has experienced two distinct periods of extension. The earliest rifting phase began in the Late Cretaceous, and occurred over a broad area (*Huerta and Harry*, 2007). This resulted in the formation of three large basins in the Ross Sea - The Eastern basin, the Central basin and the Victoria Land basin (Fig. 1.1). The second phase of extension occurred during the Cenozoic (*Huerta and Harry*, 2007). This extension was much more focused and occurred primarily within the Victoria Land basin, resulting in the formation of the Terror Rift (Fig. 1.1).

Mount Erebus is a 3794 m active volcano located on Ross Island, which is also the site of two extinct volcanoes. The formation of a proto-Erebus is estimated to have begun 1.3Ma (*Esser et al.*, 2004). A persistently convecting phonolitic lava lake was first sighted in December 1972 (*Giggenbach et al.*, 1973), but there are several reports of its existence from as early as the beginning of the 20th century (*Giggenbach et al.*, 1973).

The northern extent of the Terror Rift is at Mount Melbourne (*Cooper et al.*, 1987), and although previous studies have located the Terror Rift within the Victoria Land Basin, the rift's southern extent is still unknown. While Ross Island is also located within the Victoria Land Basin, any interaction between the Terror Rift and the island are unknown. The main objective of this study is to gain a greater understanding of the crustal structure beneath Ross Island in order to determine how the island and volcano are affected by rifting, Mount Erebus provides a great opportunity to learn more about lava lakes and shallow magma systems in a unique environment. Much is still unknown regarding Antarctic geology; however, the continent is ideal for studying seismology, as it has very low-level background and human noise. Erebus volcano has persistent low-level activity, which enables the continuous deployment of instruments with low risk of danger to human life or destruction of instruments.

CHAPTER 1

BACKGROUND

1.1 Previous Geochemical Studies

This work aims to characterize the crustal structure beneath Ross Island. Ross Island is the site of four volcanoes, of which Mount Erebus is the only one still active. The lava from Mount Erebus has evolved from basanite to trachyte to phonolite (*Harpel et al.*, 2004). Geochemical investigations reveal that the 23.5% of the parental basanite magma forms the residual phonolitic magma during fractional crystallization (*Kyle et al.*, 1994). More than 1000 km^3 of phonolitic lava has been calculated to have erupted from Mount Erebus in the last 250 ka (*Esser et al.*, 2004). This, however, does not also account for the more than 1000 km^3 of basanite that erupted pre-250 ka (*Esser et al.*, 2004). The result is that a very large magma chamber, or system of many small magma chambers, must exist at depth. The geochemical signatures of the erupted lava on Ross Island present a very complex picture. *Rocholl et al.* (1995) determined that samples Victoria Land Basin trended towards Mid-Ocean ridge basalt (MORB) signatures with time, suggesting that they were not crustally contaminated and theorized an old, flattened plume head as the cause for the shift in magma composition with time. *Rocchi et al.* (2005) countered the plume theory by saying that geochemical signatures could be affected by metasomatisation. They claimed that strike-slip transtension is responsible for decompression melting that resulted in the large volume of magma generated. This conclusion is also reached by *Nardini et al.* (2009). Gas emission studies on the lava lake suggest a cyclical convection of the lake where lava rises from depth, enters the lake, degasses and then sinks (*Oppenheimer et al.*, 2009). The very high CO2 emission rate measured suggests that the magma is coming from a deep mantle source (*Eschenbacher*, 1998).

1.2 Previous Geophysical Studies

Geophysical studies of Mount Erebus have mostly involved using passive sources such as lava lake eruptions or small earthquakes e.g. (*Kyle et al.*, 1982; *Aster et al.*, 2003, 2008). The first deployment of seismometers began in December 1974 with a deployment of five vertical (Mark 1) seismometers within one km of the lava lake . These seismometers measured lava lake explosions and other types of volcanic events. Previous controlled-source investigations of Mount Erebus have been carried out in the past (*Rowe*, 1988), (*Dibble et al.*, 1994) that focused mainly on Mount Erebus, or were marine seismic surveys in McMurdo Sound or the Ross Sea e.g. (*McGinnis et al.*, 1985; *Cooper et al.*, 1987; *Beaudoin et al.*, 1992). The work of *Dibble et al.* (1994) consisted of a seismic line that ran from Cape Royds on the western side of Ross Island, to Mount Erebus and then south-east towards Windless Bight (Fig. 1.3). The experiment had six large shots fired into eight stations that were located around Mount Erebus. The resulting velocity profile (Fig. 1.2) found a low velocity zone and lateral velocity changes across the volcano. The study by *McGinnis et al.* (1985) consisted of several seismic refraction and reflection profiles West of Ross Island. In particular, a 200 km long seismic reflection profile that ran North-South, located $\sim$ 20 km West of Cape Royds. They found average crustal thicknesses of 21km. A detailed seismic structure

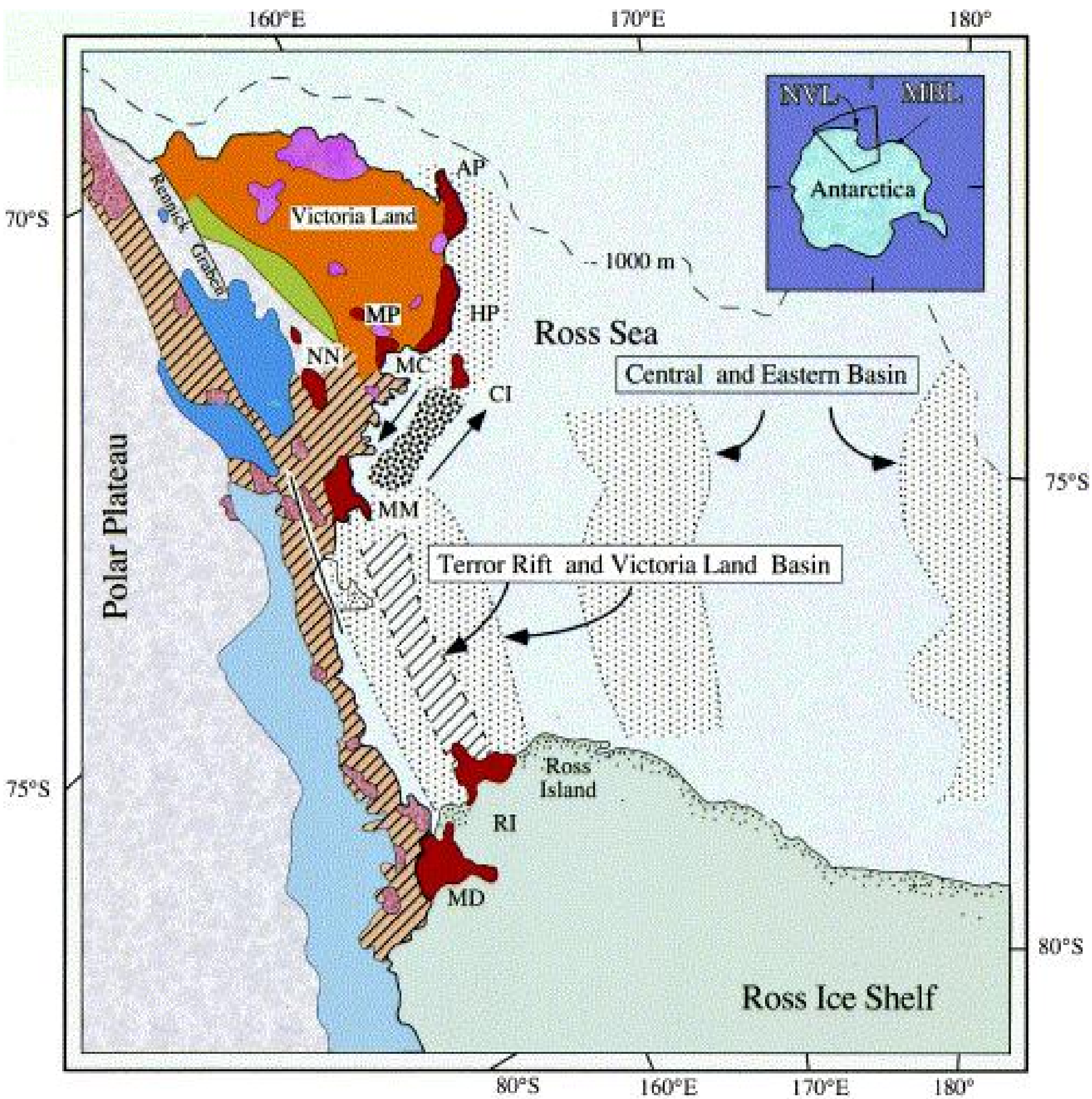

Figure 1.1: Map of Ross Sea region. Volcanics are shown in dark red. The Terror Rift, stretching from Mount Morning (MM), and Ross Island can be seen within the Victoria Land Basin. The Eastern and Central Basins are also indicated on the map (*Worner*, 1999).

and stratigraphy study performed in 1987 used multichannel marine seismic reflection data and showed the Terror Rift as narrow over the northern part of the Western Ross Sea, and more complex and diffuse over its southern extent. This

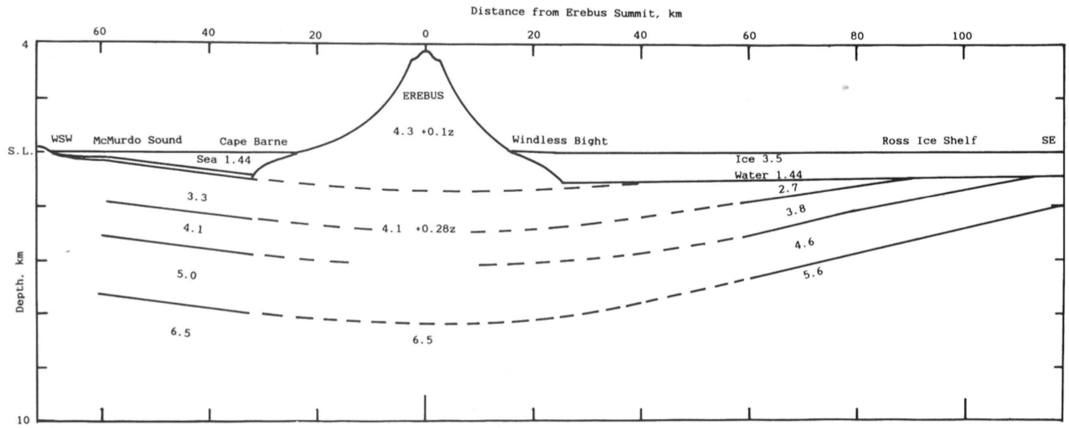

Figure 1.2: *Dibble et al.* (1994) model showing velocity structure below Mount Erebus. Cross section goes from New Harbour through Erebus and Windless Bight. This model is derived from seismic surveys conducted below McMurdo Sound by *McGinnis et al.* (1983) and *Northey et al.* (1975), a seismic survey by *Beaudoin et al.* (1992) of the Ross Ice Shelf, a seismic survey by *Stern et al.* (1991) of Windless Bight, and several studies of isostatic subsidence.

study located the Terror Rift up to within ∼50 km north of Ross Island (*Cooper et al.*, 1987). Their study found a depth to the Moho of ∼ 18 km (*Cooper et al.*, 1987). Both a 31.1 km seismic refraction profile and a 58 km long seismic reflection profile were investigated in the study by *Beaudoin et al.* (1992). The profiles were located approximately 60 km south-east of Mount Erebus, and were ∼ 15 km away from Ross Island at its closest point. Thirteen shots were used, ranging in size from 7.5 to 55 kg of explosives. The depth to the Moho was found to be ∼21 km.

Aeromagnetic and gravity data have also been acquired in the region e.g.(*Wilson et al.*, 2007; *Behrendt*, 1999; *Ferraccioli and Bozzo*, 1999), but generally have poor resolution over Ross Island. They do, however, hint towards many small volcanic centers located south of Ross Island, and a large volume of volcanic sediments beneath the McMurdo Ice Sheet. Recent tomographic work has been published

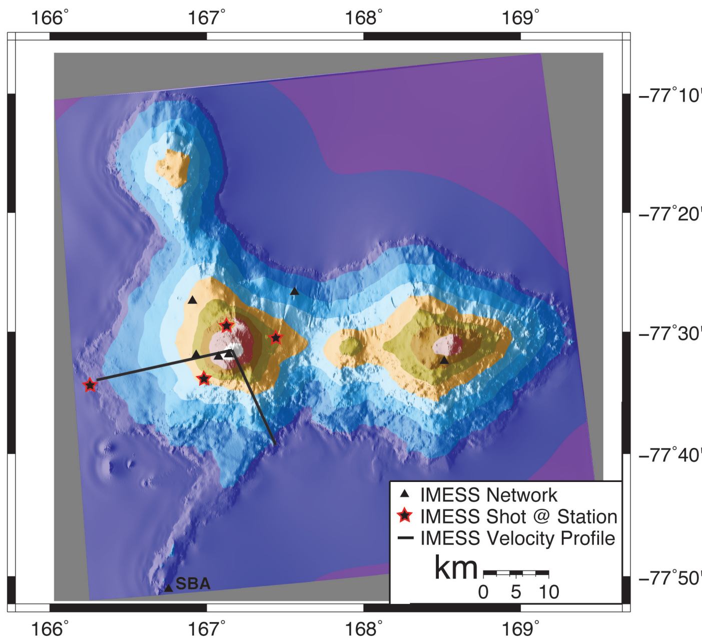

Figure 1.3: Map of Ross Island. Black line is the location of the cross-section from Figure 1.2. Shots locations are shown as red stars, and stations used are shown as black triangles.

(*Finotello et al.*, 2011), (*Watson et al.*, 2006), *Lawrence et al.* (2006) that incorporates data from the Transantarctic Mountains Seismic Experiment (TAMSEIS). A low velocity anomaly was found below Ross Island in the work of *Watson et al.* (2006). He found a thermal anomaly corresponding to temperatures that were roughly 200-300 K above normal below Ross Island that decreased both north and south along strike, away from Ross Island. A crustal thickness of 20±2 km was found by *Lawrence et al.* (2006) below Ross Island, in his analysis of both receiver functions, surface wave phase velocities and airborne gravity data. However, using the same dataset and stations, crustal thicknesses of between 19-27 km were found below Ross Island by *Finotello et al.* (2011) in his analysis of receiver functions. He suggests that the discrepancy between his results and those of *Lawrence et al.* (2006) are due to different V_s values chosen. This lack of consensus illustrates the relevance of this work and others like it that attempt to determine the crustal thickness near Ross Island.

CHAPTER 2

DATA COLLECTION

2.1 2007-2008 Field Season

During the 2007-2008 austral summer field season, a temporary deployment of 23 broadband seismometers occurred. These seismic recorders were Guralp CMG 40-T seismometers with a sampling rate of 100 samples per second. Each station included a Reftek 6 channel DAS with 4 GB of memory. These stations each had two marine batteries that were recharged with solar panels. These 23 broadband seismic recorders were deployed in two concentric circles around the summit of Erebus volcano at elevations of roughly 2000m and 3000m (Figure 2.1). Only data from several of these broadband stations that lay along the 2D profile were used in this work. Nine short-period vertical component Texan data-loggers were deployed on the summit in a fairly linear trend running north-south on the western side of the summit, and then towards the north-east (Figure 2.2). These Texans had 4.5 Hz geophones and recorded the three shots. However, this particular type of seismic recorder was not used in subsequent seasons due to limited battery life and thus deployment. This deployment was, at that time, the densest deployment of stations on Ross Island.

Three explosions were used as active sources for this array. In order to reduce the chances of a shot blowout, the holes for the explosives was drilled

	ANFO (kg)	Boosters (kg)	Number of caps
Drill Site #1 West			
Hole 1	75	1.6	2
Hole 2	62.5	1.6	2
Hole 3	62.5	1.6	2
Fang			
Hole 1	100	3.6	2
Hole 2	100	3.6	2
Hole 3	100	4	2
Cones			
Hole 1	0	11.2	2
Hole 2	117	1.6	2
Hole 3	117	1.6	2
Hole 4	116	1.6	2

Table 2.1: Shot information from the 2007-2008 field season.

down to 10m depth, and filled with ANFO and deployed. Table 2.1 shows the number of shot locations and amounts of ANFO, boosters and caps used in all the shots. These stations complemented the eight permanent network stations that had already been deployed on Ross Island. In addition to recording the active source explosions, the array also recorded icequakes, lava lake explosions and teleseismic earthquakes.

2.2 2008-2009 Field Season

This field season was a very ambitious year in terms of the station deployment. Two experiments were planned, Tomo-Erebus 2D and 3D. The 3D survey consisted of 79 RefTek 130s that had a 24-bit resolution and a sampling rate of 200 samples per second. These were used with three-component Sercel L-28-3D 4.5 Hz geophones. These were arranged in a 3 x 3 km grid on the summit and crater of Erebus. This was in addition to the 23 broadband seismometers that had been

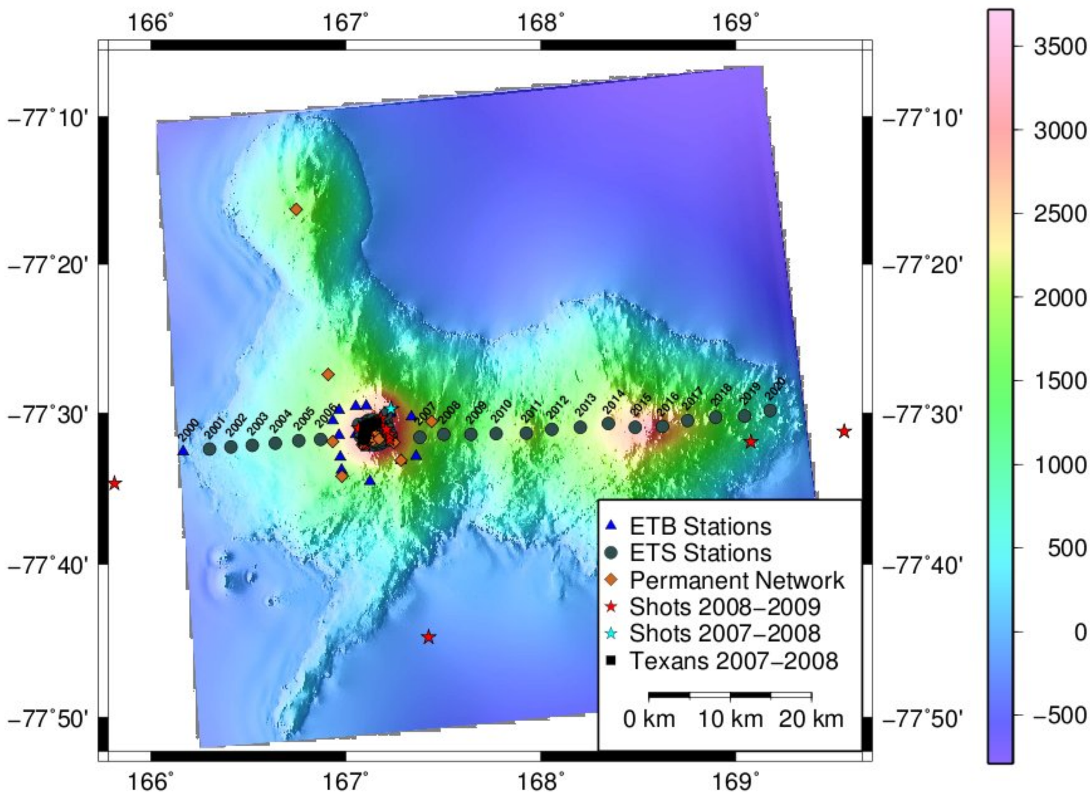

Figure 2.1: Map of Ross Island showing the station deployment. All ETS stations were deployed during the 2008-2009 field season, ETB stations were deployed during the 2007-2008 field season, and Permanent Network stations were deployed during the 1999-2000 field season. The TE-2D survey used the 21 ETS stations that are along the 76 km East-West profile across the island.

deployed around the summit during the previous field season.

The 2D survey was consisted of 21 seismic recorders that were identical to the ones used in the 3D survey. The 76 km long profile was in an east-west trend from Cape Royds to Cape Crozier. These stations had a spacing of approximately 4 km. For the fifteen onland chemical blasts, holes of a diameter of 20 cm were drilled between 7-15 meters depth in the snow. The holes were then filled with

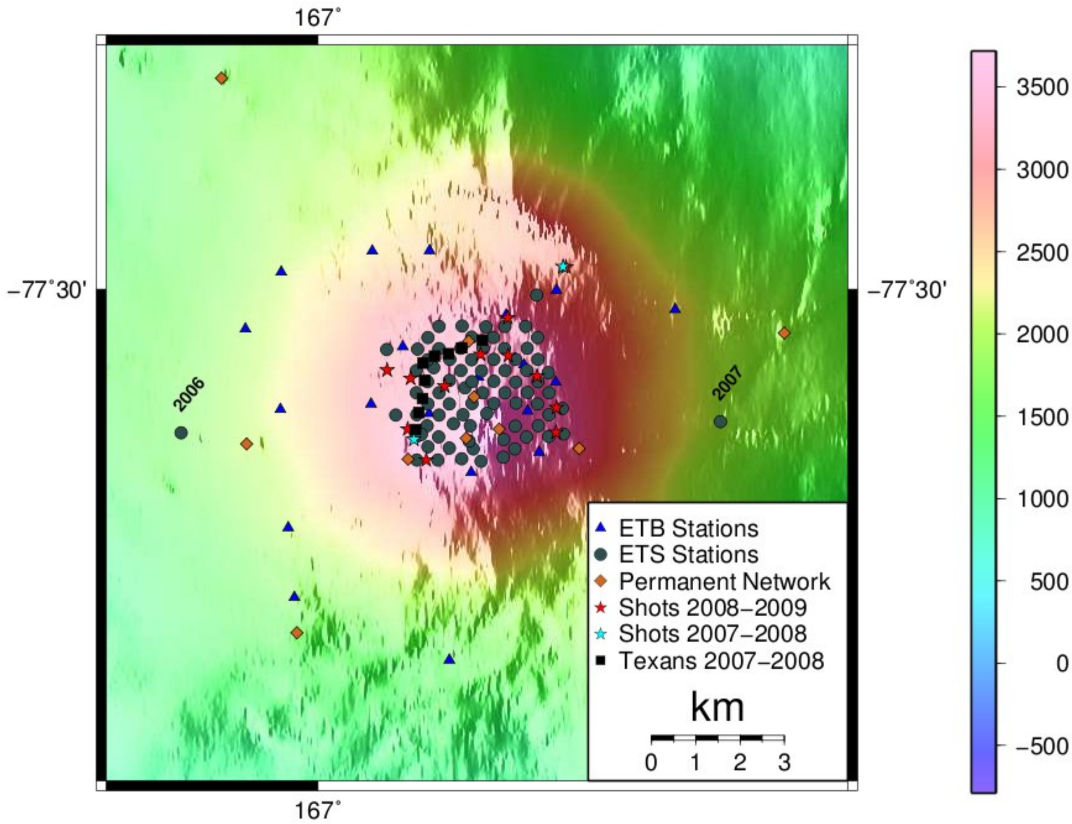

Figure 2.2: Zoomed in map of Mount Erebus showing the station deployment. Twelve of the sixteen shots used during the 2008-2009 field season can be seen, as well as the configuration of 79 ETS instruments that were deployed primarily for the TE-3D experiment.

between 75-600 kg of ANFO (Ammonium Nitrate and Fuel Oil), packed with snow and left for 24 hours to cinter. Table 3 has all the amounts of ANFO used for each shot. There was an additional sea shot carried out in McMurdo Sound that used 200 kg of dynamite. This shot was found to have the clearest and strongest first *P* wave arrivals that were recorded on all stations.

The data and field notes were brought back to New Mexico Tech for processing. The data processing initially involved organizing the data and reviewing all data logs such as power output, GPS locations and temperature readings. It was necessary to perform this step before interpreting the data, so that any suspicious readings could be identified and addressed. Once this quality control step had been completed, the data were converted into a miniseed format and an Antelope database was populated. The data were then combined with the Antelope database. Finally, the integrity of the database was verified and a dataless seed volume was generated. This volume, along with the data in miniseed format, was then sent to IRIS PASSCAL's Data Management Center (DMC).

After the data had been reviewed, inital processing began. First, the 2D data were converted to a SEG Y format and input into ProMAX processing software. Very minimal filtering was performed here, using a Butterworth bandpass filter to pass frequencies between 0.5 and 10 Hz. These filters are designed by inputting frequency-slope-frequency-slope, and the filter used on the data was 0.5-1-10-40. Appendix D shows the shot gathers for all shots. All first *P* wave arrivals for each station and shot were picked and pick files were created in ProMAX for four stations. These files were then used in the 1D and 2D forward modeling.

CHAPTER 3

METHODS

Forward modeling is computationally easier to perform, but less accurate than inverse modeling. It provides a relatively quick, simplistic model of a portion of the Earth. As inverse models require an input starting model, it is therefore useful to create a forward models for that purpose. 1D forward models were made for four shots, Cape Royds at the west, FANG at the summit, and both shots at Cape Crozier on the east of the island. 1D forward models provide information on the crustal structure only directly below the shot location. Thus, they are best for describing the velocity structure of the upper-crust. These models were compared with the *Dibble et al.* (1994) model as well as being then used as the starting model for the 2D seismic tomographic inversion. A 2D forward model was also developed along the profile. The 1D forward models were very useful in developing the 2D model.

3.1 1D Forward Models

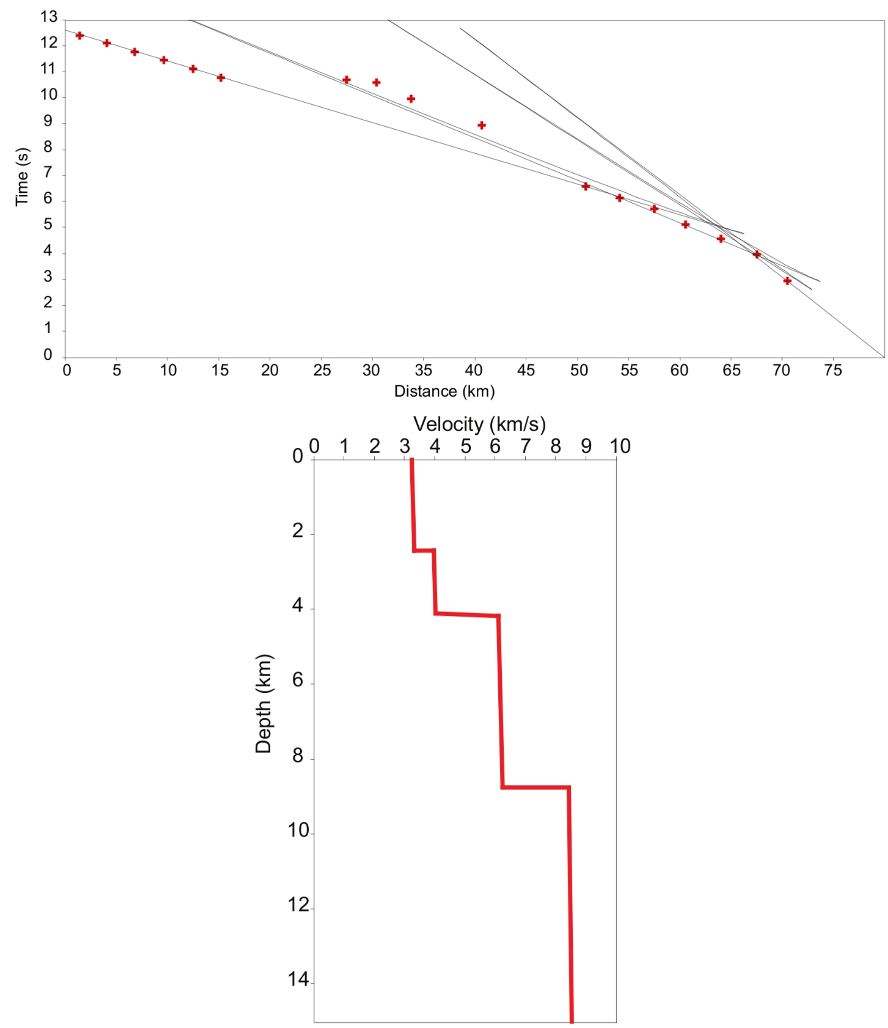

Figure 3.1: 1D Forward Model from Shot 4001 Cape Crozier. The best fit solution has 4 layers, with an initial layer that is just over 2 km thick, and has a velocity of a just over 3 km/s. The second layer is about 1 km thick and has a velocity of 4 km/s. The third layer is 5 km thick and has a velocity of 6 km/s that increases with depth. The fourth layer begins at about 9 km depth with a velocity of more than 8 km/s.

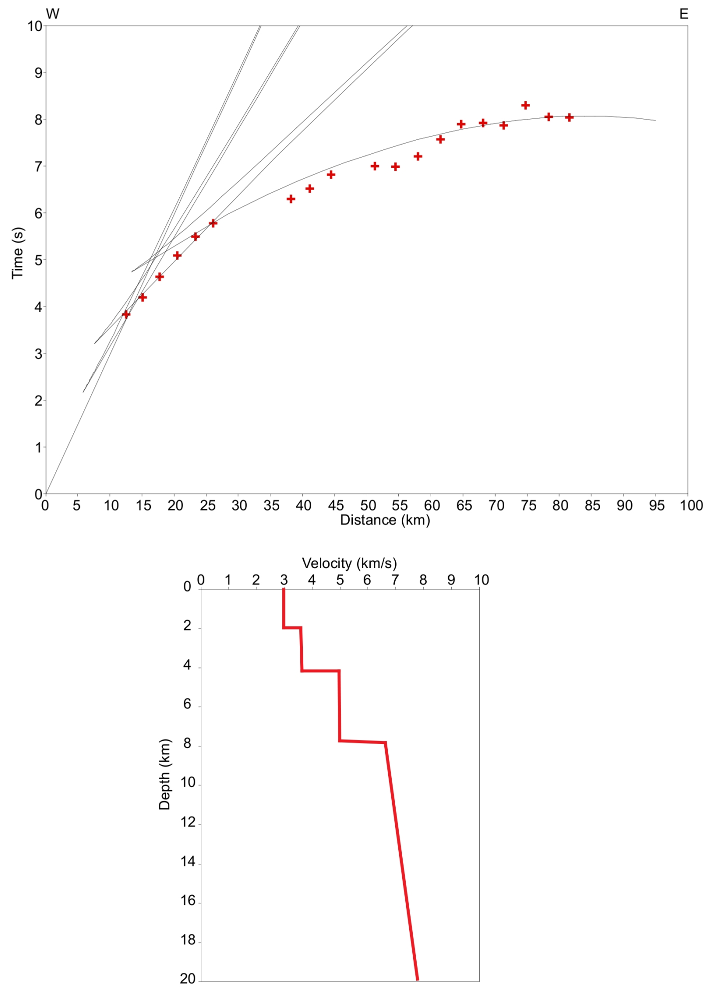

Figure 3.2: 1D Forward Model from Shot 4002 Cape Royds. The best fit to the time-depth data resulted in a model that has an initial velocity of 3 km/s from the surface to 2 km depth. The second layer was from 2 4 km depth and had a velocity of 3.5 km/s. The third layer had a depth of roughly 4 8 km, with a velocity of 5 km/s. The last layer began at 8 km/s and the velocity of this layer slowly increased with depth.

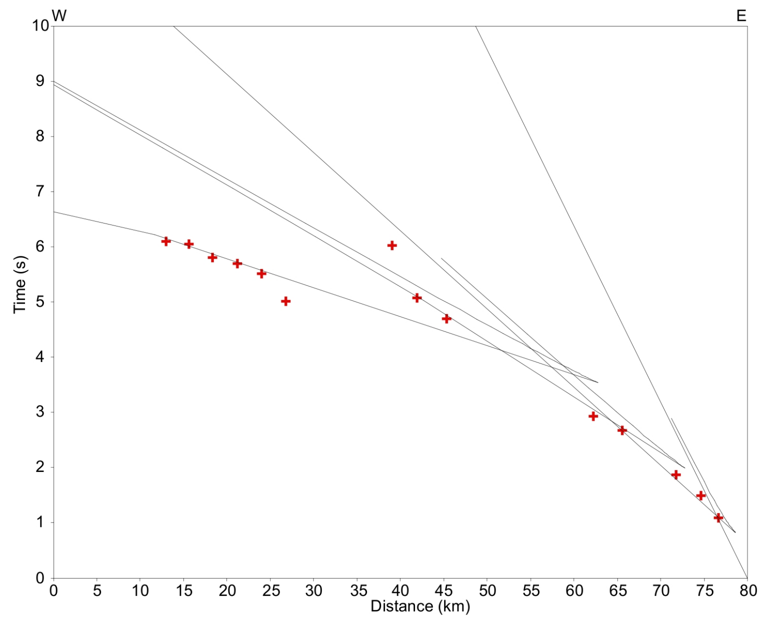

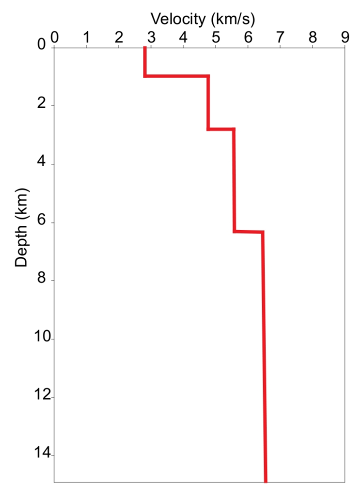

Figure 3.3: 1D Forward Model from Shot 4003 Crozier 2. Even though this was very close to the Cape Crozier shot, there are large differences in the near surface profile. The energy from the Cape Crozier shot did not carry to all of the seismic recorders and so this location was re-shot, using more explosives. There is a velocity of just below 3 km/s down to a depth of 1 km. There is a velocity of 5 km/s between the depths of 1-3 km, and a velocity of 5.5 km/s from the depths of 3 km 6.5 km, and then a velocity of 6.5 km/s from the depth of 6.5 km down.

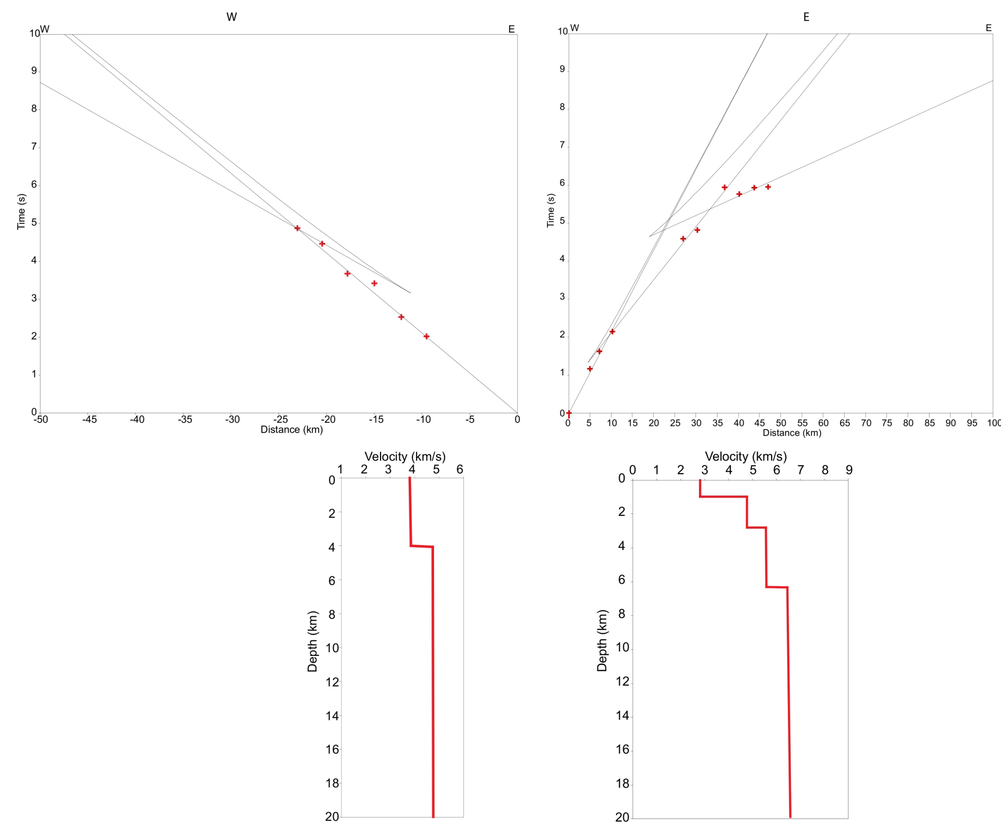

Figure 3.4: 1D Forward Model East and West from Shot 4004 FANG. These models were split up into west and east of the shot location. The east model shows velocities of just below 3 km/s down to 1 km below the surface. From 1 3 km depth, the second layer has a velocity of almost 5 km/s. A third layer of extends from 3 6.5 km below the surface with a velocity of 5.5 km/s. Below this depth we have a layer at a constant velocity of 6.5 km/s. For the west model, there was a velocity of just below 4 km/s down to a depth of 4 km, and then a constant velocity of 5 km/s.

1D forward models were created using the MacR1D software that was developed by *Luetgert* (1988a). All of the first *P* wave arrivals were picked at every station used in the TE2D survey for all sixteen shots, using ProMAX. Pick files were then created, which were a table of *P* wave arrival times for each station. The pick files were then input in the MacR1D raytracing software. Within this software, velocity-depth models are created and then refined by trying to match the synthetic time-depth data for the model with the actual travel-time data. The number of layers, depth to each layer and velocity gradient can be adjusted within the model. Models were created for the Cape Crozier shot (Fig. 3.1), the Cape Royds shot (Fig. 3.2), the Crozier 2 shot (Fig. 3.3) and the FANG shot (3.4). Since the FANG shot was on the summit, the model shows east and west of the shot location.

As there are no changes in velocities below 8km for the Cape Royds shot, and 6.5 km for the Crozier 2 and FANG Shots, it can be assumed that below these depths, the effects of the shots are not felt. These 1D models are therefore only effective for upper-crustal velocity modeling. It should be again noted that these are non-unique solutions, but these results were compared with the Dibble et al [1994] model, and each shot model was also found to be consistent with each other.

3.2 2D Forward Models

The software used for the 2D forward modeling was the MacRay program *Luetgert* (1992). Three shots were used to develop this model the Cape Royds, Cape Crozier and FANG shots. Again, the input data are the pick files containing the travel-time information. Also, a number of layers are added and adjusted

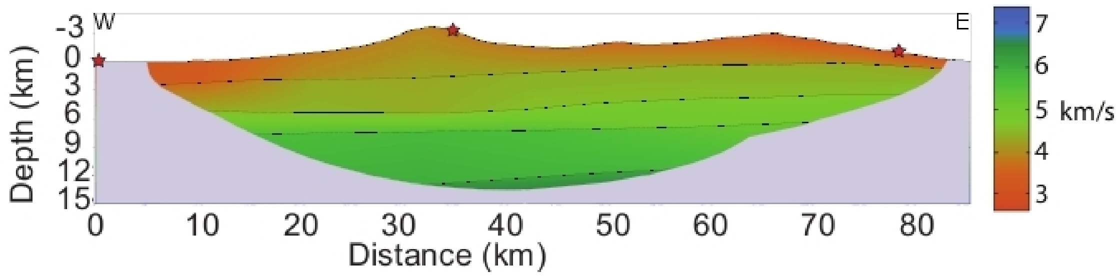

Figure 3.5: 2D Forward Model across Ross Island. Three shots were used to create this model, which are represented by red stars. West shot is at Cape Royds, shot at summit of Erebus volcano is at Fang, and east shot is Cape Crozier shot.

based on the comparison of the synthetic travel-time curves of the model with the real travel-time curves. These layers can also have a velocity gradient. The number of layers, their depths and velocities were chosen based on the 1D forward models. This software allows for rays to be shot from a specified shot point along a selected boundary layer, resulting in a synthetic travel-time plot. The layers are then adjusted, upon comparison of the two datasets, by either changing the velocity of the layer, the velocity gradient of the layer, by adjusting the depth of the layer, or by a combination of those three options. After the travel-time data from the first shot matches the observed travel-time data for the first layer, then the second and finally third shots were added. These shots can only be looked at one at a time, and because each change made in the model would affect the way the travel-times of the rays from the other two shots, this was an iterative process. This was then repeated for the lower layers. The resulting model is shown in Fig. 3.5, while the traveltime fits for two shots are shown in 3.6.

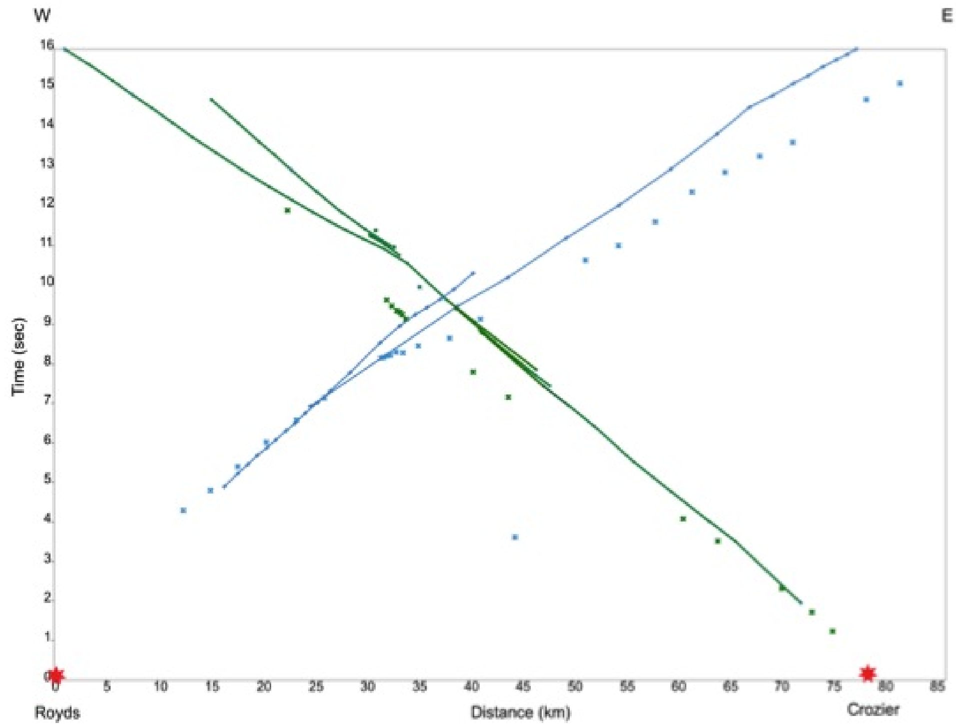

Figure 3.6: Travel-time fits for 2D forward model showing synthetic and observed data from the Cape Royds shot (blue) and the Cape Crozier shot(green). Only two of the three shots used are shown for simplicity. Straight lines represent the travel-time information from rays shot through the model, while the points represent the observed travel time data.

3.3 Tomography

The resulting data from the controlled-source experiment are travel-times. In order to get the travel-times, all of the first P wave arrivals were manually picked at all of the stations for each of the sixteen shots. The picks were also assigned a weight based on the confidence of the pick on a scale of 0 to 4, with 0 being the least confident and 4 being the most confident in the pick. Each of the weights was assigned a range of time uncertainty for that pick, and these are shown in Table 3.1.

Only the stations that were on the 2D transect were of interest to us for 2D tomography, so only the picks corresponding to these stations were used in the analysis (Fig 3.7). This resulted in 660 raypaths. A Matlab code took the input file that had over 600 raypaths, and removed stations that were more than 2 km away from the transect as well as raypaths that varied by more than 20 ° from the transect. As a result, 363 raypaths were ultimately used in the inversion. A map view of those raypaths are shown in Figure 3.9, where the 363 raypaths used are shown in red, and the raypaths not used are shown by black lines. The inversion code used was written by *Um and Thurber* (1987) and modified by Richard Aster for this specific problem. The model was set up to be 87 km long east-west, and 13 km vertically, with 6 km of padding in all four directions. The velocity was paramaterized by 0.5 km grids. The initial starting model used was based off of the 1D models done for the Cape Royds, Cape Crozier and Fang shots, presented in this work, as well as the *Dibble et al.* (1994) model. A starting velocity of approximately 4 km/s was used as the elevation for the summit of Mount Erebus and the velocity increased down to 6.27 km/s at 19 km depth. The raypaths were initially input as circular raypaths (Fig. 3.9).

Regularization was used to help us solve this problem. Inverse modeling is unstable as small changes in the noise can have large effects on the model. Regularization is applied to inverse problems as a way of adding constraints which bias a particular solution. The most widely used type of regularization for ill-posed problems (non-unique solution) is Tikhonov regularization, which punishes sharp discontinuities in the data, and thereby helps to smooth the model. The equation that we are attempting to solve is

$$min\|G(m) - d\|_2^2 + \alpha^2\|Lm\|_2^2 \tag{3.1}$$

where L is the first and second order Tikhonov regularization smoothing matrices, combined into one roughening matrix, G is the forward operator, m is the model, d is the vector of travel-time data, and α is the user-defined regularization parameter. In order to find the best model, we use the Gauss-Newton method by solving the equation below

$$(J(m)^T J(m) + \alpha^2\, L^T L)\Delta\, m = -J(m)^T (G(m) - d) - \alpha^2\, L^T L m \tag{3.2}$$

We first input a model and a value of α, and solve for Δm. This value of Δm is then added to the initial value of m, such that

$$m = m + \Delta\, m \tag{3.3}$$

For this specific problem, we used 3 iterations of each value of α, such that equation 3.3 was repeated 3 times for each α value. Then, this process was repeated for another value of α until the code was complete. Thus, at the end we had three models for each value of α. In order to determine which value of α corresponds to the best model, we use a tradeoff curve known as the L-curve. Since $\|Lm\|_2$ is always decreasing with respect to α, and $\|Gm - d\|_2$ is always increasing with respect to α, a plot of those two functions will yield a curve with a characteristic 'L' shape, where the corner value corresponds to the best value of α. The best value of alpha found, based on the L-curve (Fig. 3.11), was found to be 586.5514, with an rms of 0.23605. For all alpha values, the maximum liklihood, increases with the number of iterations, while the residual norm

$$\|G(m) - d\|_2 \tag{3.4}$$

decreases with the number of iterations.

Weight	Time in seconds
4	0.000 0.012
3	0.012 0.013
2	0.013 0.015
1	0.015 0.020
0	0.020 1.000

Table 3.1: Uncertainty in time corresponding to weights assigned during picking.

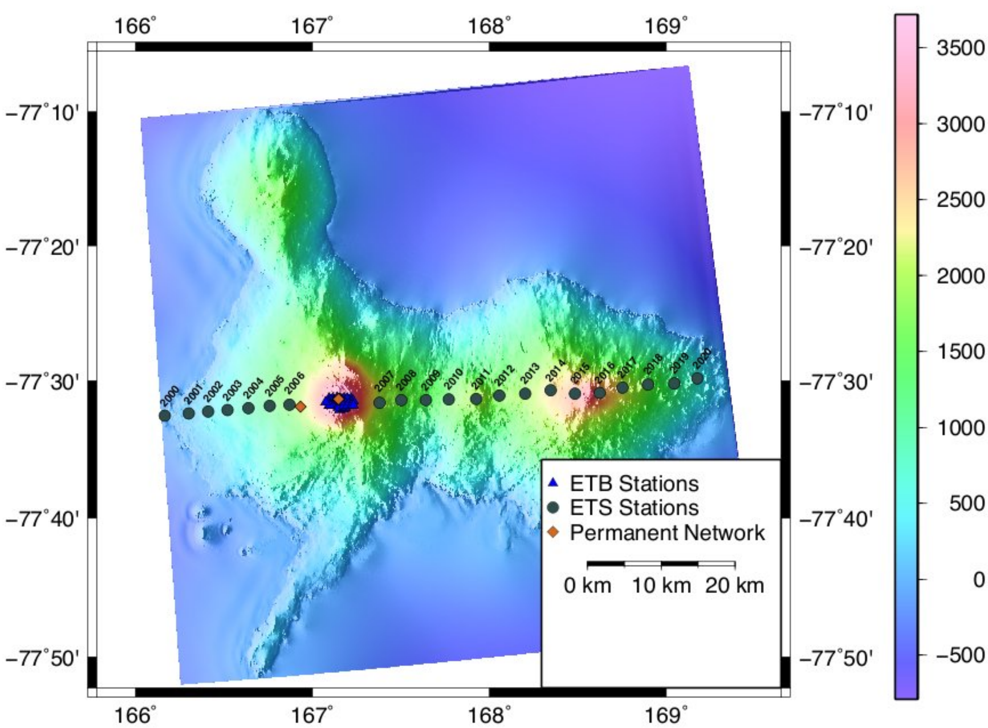

Figure 3.7: Stations that roughly lie along the East-West profile. These stations include the ETB, ETS and Permanent Network stations that lie along the east-west transect. All of these stations were considered for the tomography

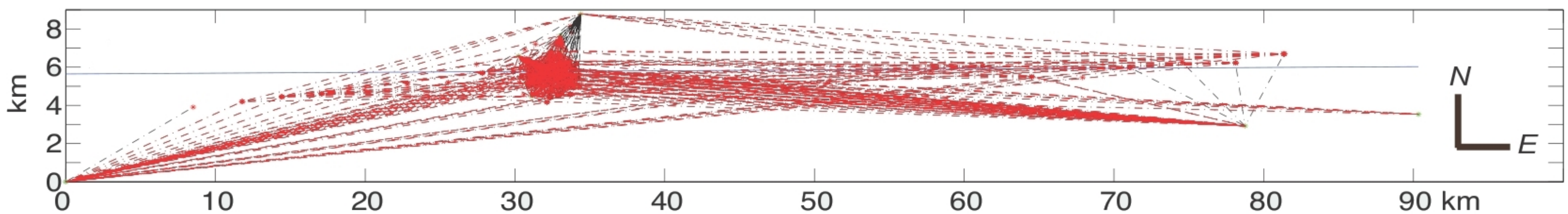

Figure 3.8: Distribution of raypaths of station-shot pairs from 3.7 in map view. Only raypaths within 2 km perpedicular to transect or less than 20 ° from the transect were used. All raypaths used are shown in red, and all raypaths not used are shown as black lines. Ultimately, 363 raypaths were used.

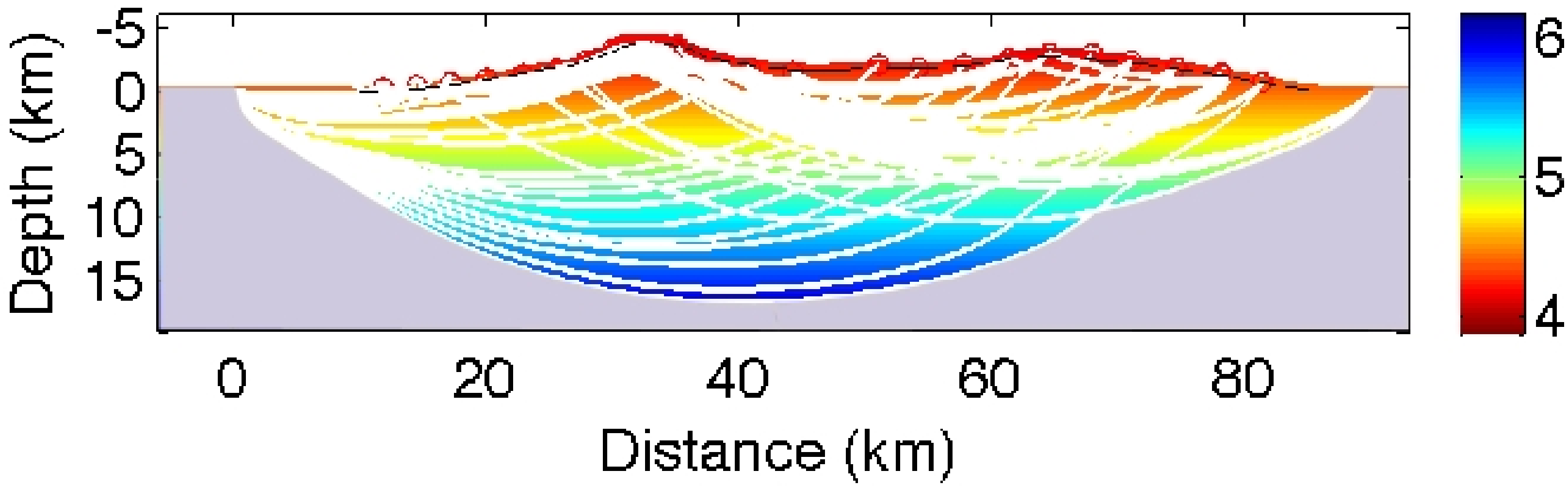

Figure 3.9: Gradient velocity model showing circular input raypaths as white lines. Velocity gradient is shown in km/s. Topography of Ross Island is shown as a black line, and areas without raypath coverage are shown in gray.

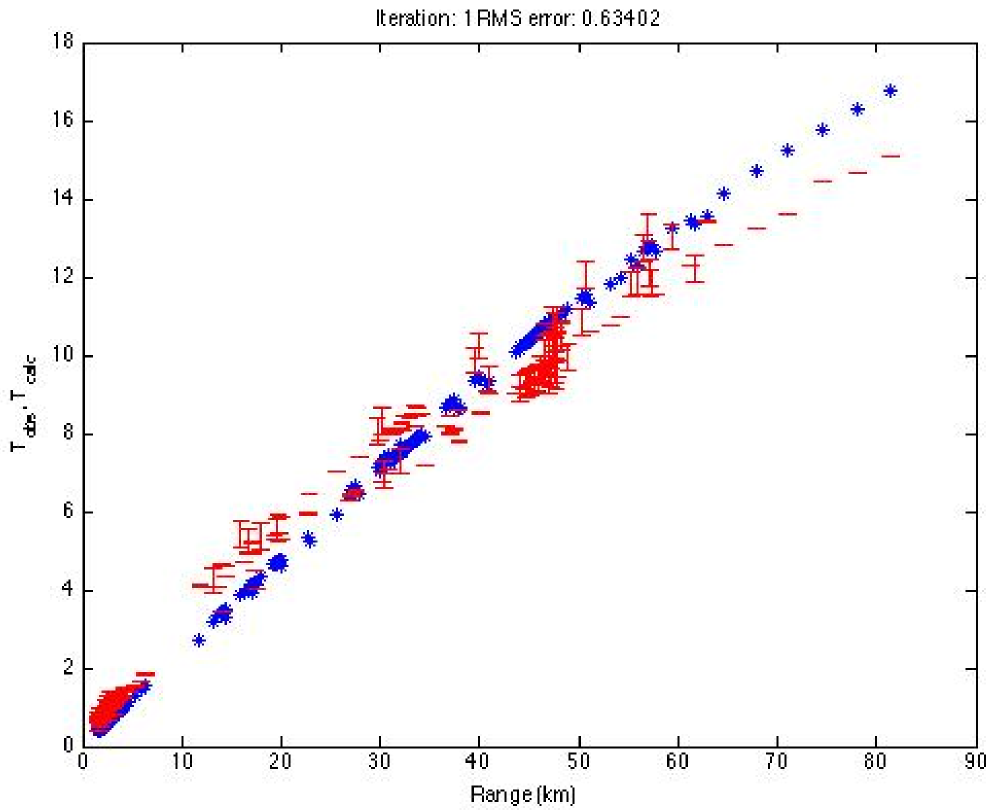

Figure 3.10: RMS Error for input gradient model. Input gradient model is based on the work of *Dibble et al.* (1994). The starting RMS for raypaths through this model is 0.634, which represents the residual between observed travel times (red) and calculated travel times (blue)

The choice of the 'best' model (Fig. 3.12) was made from a visual inspection of the L-curve (Fig. 3.11). At first, it seems that there is a clear corner at $\alpha = 107.7181$. However, for values of α that are less than 101.7181, $\|Gm - d\|_2$ decreases as $\|m\|_2$ also decreases. These values are displayed by open circles in Figure 3.12. From equation 3.1 above, $\|Gm - d\|_2$ is an always increasing function of α, thus, these values of α are not real as these models do not converge. Although an α value of 586.5514 is the preferred model, it should be noted that the rms errors of all models are quite high, and none of these models are very

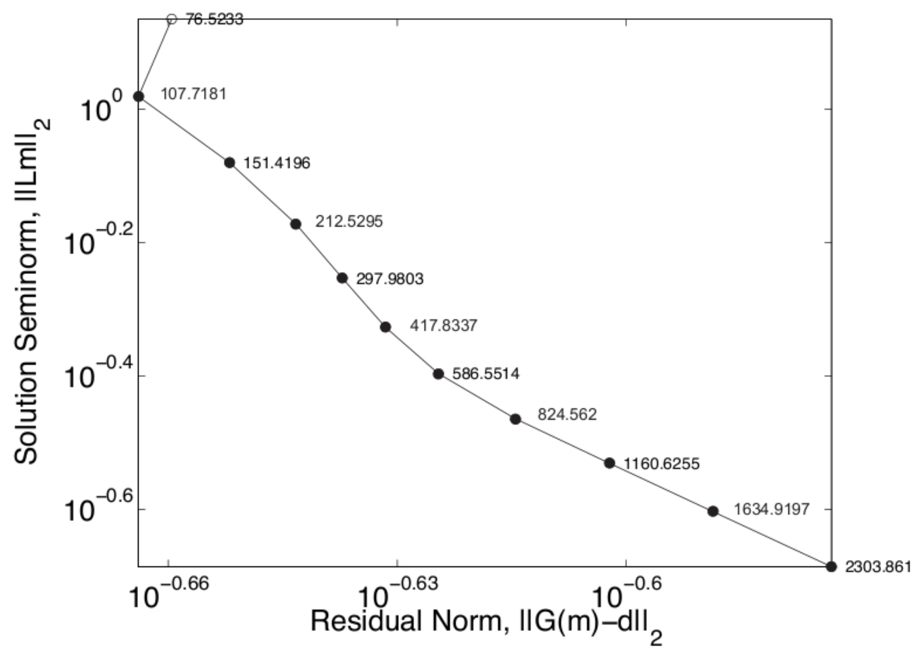

Figure 3.11: L-Curve showing subtle corner at α = 586.5514. Open circles represent values of the regularization parameter whose models do not converge.

well regularized. This is due to the inadequate distribution of raypaths within the model.

Checkerboards of 35 x 35 km anomalies of alternating velocity anomalies were constructed and superimposed on the original velocity gradient (Fig. 3.15). These perturbations of velocity are small enough that the checkerboard shape is resolvable after the inversion process, but not so large that they cause significant raypath deviation. The rays were traced through this new model and the raypath times were recorded as the input times for the inversion. The inversion was then run, with the expectation of recovering the checkerboard model, the result of which shown in Figure 3.16. As expected, the best resolved areas correspond to areas with the densest ray coverage, at the summit of Erebus, and along the near-surface, with poorer resolution at depth.

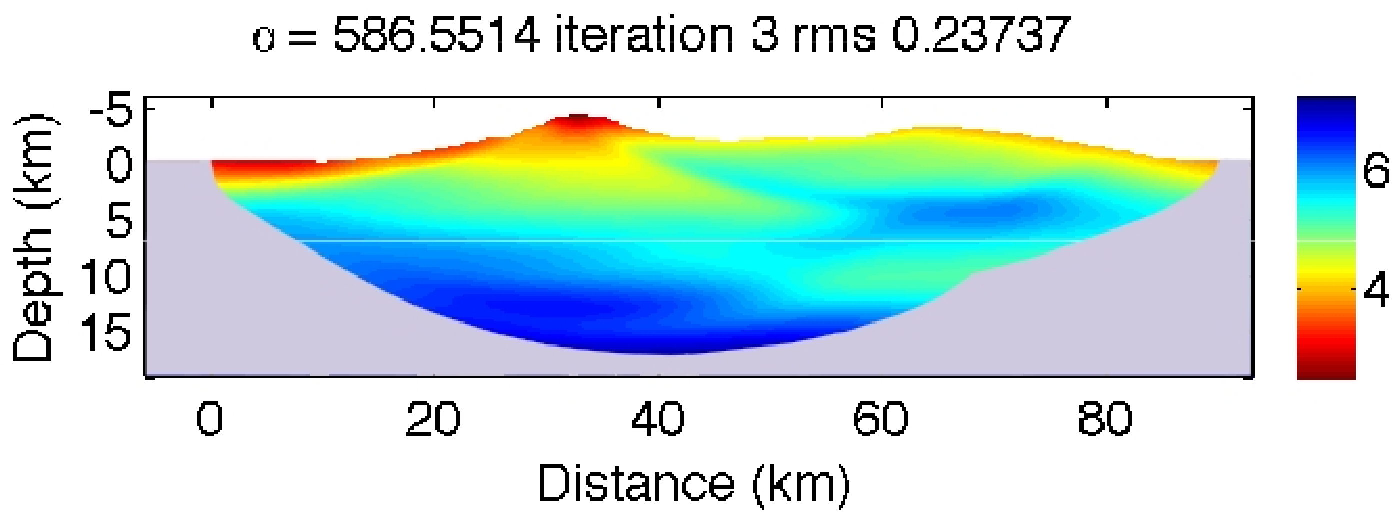

Figure 3.12: Best Model from tomographic inversion. Velocities are shown in km/s.

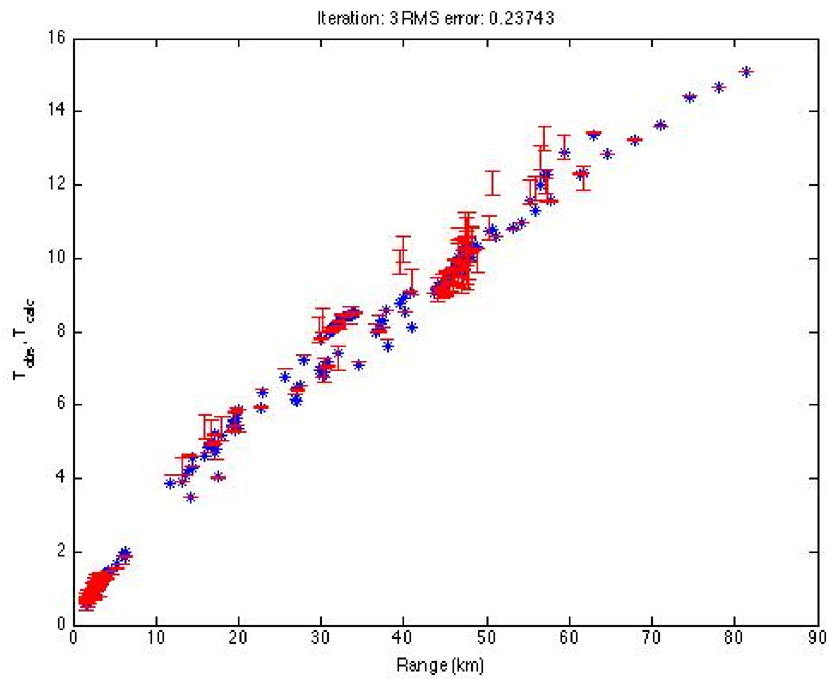

Figure 3.13: RMS Error between observed and calculated travel times for α = 586.5514. Again, the observed travel times are in red, and calculated travel times are shown in blue.

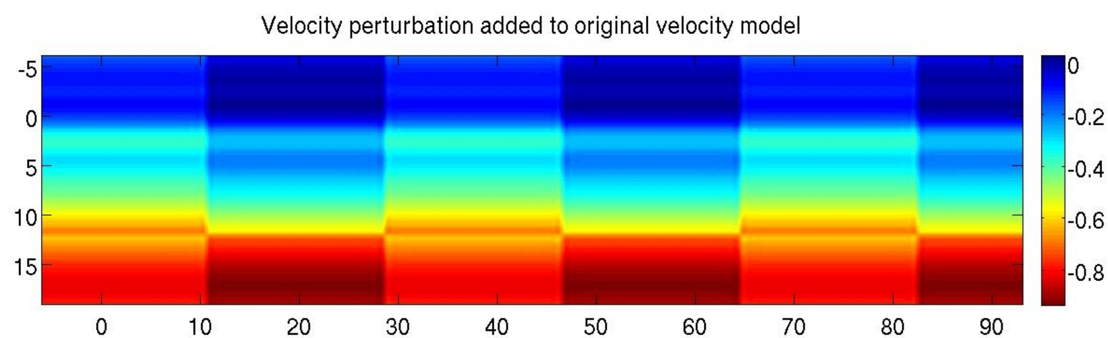

Figure 3.14: Velocity perturbation that was superimposed over gradient velocity model in order to do checkerboard test. Input velocity pertubation is also a velocity gradient.

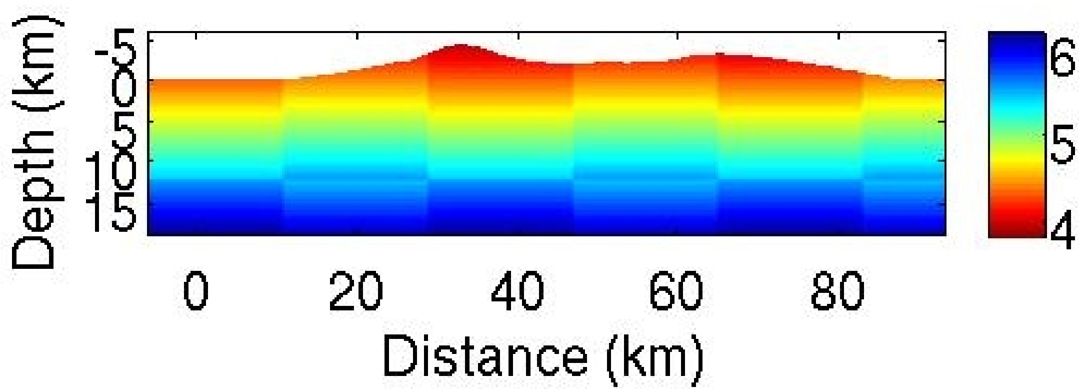

Figure 3.15: Input Checkerboard model with 35 km checkers, that was composed of the velocity perturbations from Figure 3.14 superimposed over the velocity gradient model of Figure 3.9.

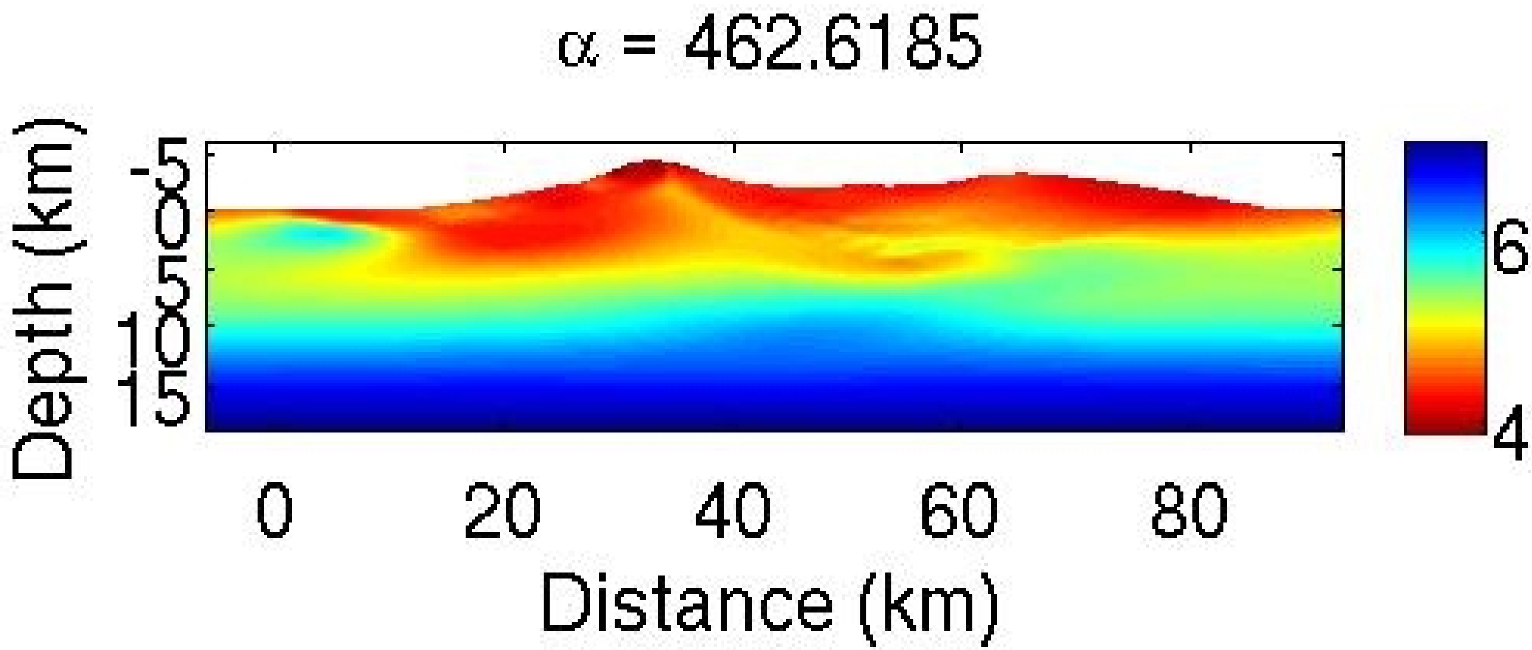

Figure 3.16: Result of checkerboard inversion using 35 km checkers for α = 462. Evidence of checkerboard is only seen in the near surface, especially in areas that had the densest raypath coverage.

CHAPTER 4

DISCUSSION

Different modeling techniques were applied to data from a large seismic survey conducted during the 2008-2009 field season on Ross Island, with the intention of better characterizing the crustal structure. Prior to this study, only one other velocity model of the island had been created that only covered the western portion of the island, and resolved features at depths no more than 6 km below sea level *Dibble et al.* (1994). As this model was constructed using data from several studies, it is quite robust. Even though the model is fairly simple, it does provide some interesting detail, such as evidence of a low-velocity zone below Mount Erebus and lateral velocity changes across the volcano. It is the only model we have to compare the results from this study to.

1D models were created for 4 shots across the island; at Cape Royds, Fang (summit) and both shots at Cape Crozier. They generally are accurate to 6 km below the shot location, and show similar velocity values at comparable depths to the *Dibble et al.* (1994) model. The 2D model was created using 3 shots across the island. Because only one shot was used on the summit, it is not very well resolved in the near-surface, but at mid-crustal depths of around 5 km, it shows general agreement with previous work. The tomography models show a marked improvement over previous velocity-gradient style models, especially in areas of high raypath coverage.

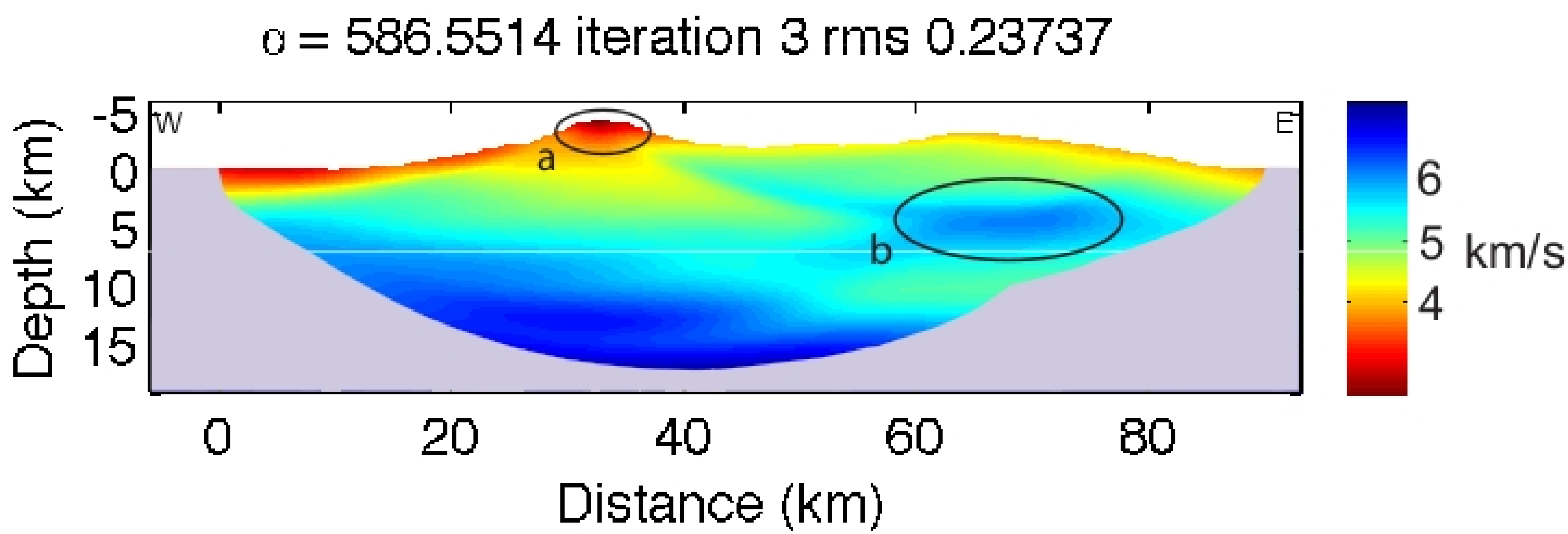

Figure 4.1: Best tomography model. (a) shows very low velocities of less than 3 km/s at the summit of Erebus volcano, (b) relatively high velocities below Mount Terror. Both features are in areas of high raypath coverage, and thus are the among the best resolved areas of the model.

One advantage to this method over forward modeling is that reducing the residuals are are handled by the code and not by the user. This makes it less biased by human error. The RMS for the gradient model is 0.634, while the RMS for the best tomography model was 0.237. The gradient models tended to not be able to handle horizontal velocity changes very well, and even though the tomography code applied a horizontal smoother, it was still able to resolve certain features, such as the higher than background velocity below Mount Terror (Fig. 4.1). There are many raypaths that have the same orientation and thus cause horizontal smoothing in the model. However, there are several raypaths that cross that swath of raypaths. Velocities where raypaths of different orientations cross tend to be better resolved, and this happens in several places of this high velocity anomaly. Therefore, while I do believe that this high velocity zone exists at depth, it is difficult to determine the dimensions of the anomaly, and its actual shape, since currently its shape is a function of the raypaths. Another robust feature is the anomalously low-velocities observed at the summit of Erebus volcano. The best raypath coverage is in this area, due to the twelve summit shots and the raypaths also come in at a variety of angles from both east and west. These velocities are less than 3 km/s, approaching the velocity of phonolitic lava. The smoothing effect is again seen in the This smoothing effect is seen in the higher velocity lobe that runs from the summit to that high velocity below Mount Terror. Here there are much less raypaths at an angle to this swath of raypaths and so the smoothing effect of these paths overwhelms the model in this area. The apparent lower velocity region below this swath of raypaths going east from the summit has very similar velocities to the input velocity model, since there are very few raypaths that are in this area. This does not represent a velocity discontinuity of any kind. We can look at the horizontal layer east and below the volcano at around 5 km depth in order to see how a dearth of raypath results in no changes to the input gradient model. The model here reflects is very minimally changed from the gradient model, since there are about 2 raypaths that go through this area.

A comparison of the tomographic image with the *Dibble et al.* (1994) model is shown in Figure 4.2. It is very interesting that from 1 km above sea level to 7 km below sea level, the models are almost identical. This figure clearly demonstrates the agreement of this work with previous work. However, the large difference between the two models is at the summit region of the volcano to 1 km above sea level or in the upper 3 km of the volcano. Here, the tomographic model produced from this study has significantly lower velocities. As the summit region is the area with the highest raypath coverage, it is the best resolved area of the entire study. The velocities from this study, especially in the near-surface therefore seem to be more accurate. Another interesting thing is the perceived low velocity zone that was in the *Dibble et al.* (1994) model. If we are to assume that in the near-surface, the velocities from this study are correct, then it seems that the velocities down to 7 km depth are increasing with depth, and the low velocity zone observed by *Dibble et al.* (1994) is due to his higher summit velocities.

All studies conducted in this region have found the Terror Rift at depths greater than 18 km (e.g. *Lawrence et al.* (2006)). A general rule of seismic refraction is that the maximum resolvable depth that can be imaged is typically one fifth of the length of the line of seismic recorders. As the length of our line is 76 km, we expect to see raypaths not much deeper than $\sim$15 km depth. Thus, we neither expect to see, nor do we see, any evidence of the Terror Rift for the deepest parts of the profile. Most maps of the Ross Sea region show the Terror Rift running

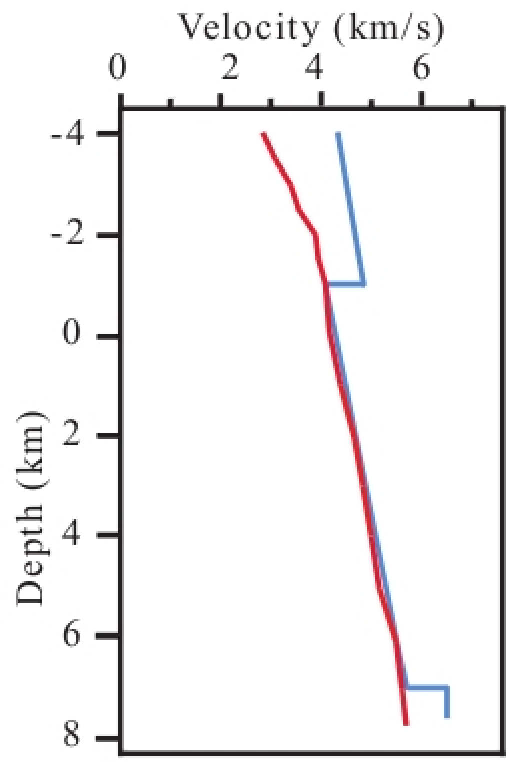

Figure 4.2: Comparison of velocity profiles from the 2D tomographic images (red line) with the *Dibble et al.* (1994) model (blue line) at Erebus. The models are identical from above 1 km above sea level to 7 km below sea level. The summit velocities of this study are much lower than the previous model.

directly below Mount Erebus, when no studies have indicated its presence within ~200 km of Ross Island. The only large-scale velocity model produced for Ross Island by *Dibble et al.* (1994) did not extend east past Mount Erebus, so it has not been possible, before this current study, to be able to make conclusions on any rift effects on the island. This velocity model produced by this study does not see any evidence of rifting or offsets for any crustal depths between Mounts Erebus and Terror as has been hypothesized. There are several rays that cross pass through this region, including several crossing rays (which help to constrain velocities by reducing the smoothing effect due to unidirectional rays), so even though the resolution is poor, any large-scale offset would be observed.

Seismic tomography studies have carried out at several volcanoes worldwide, but arguably the most and best studies have been conducted at Mount Vesuvius, whose lava bears some geochemical signatures to that of Erebus volcano. These studies also tend to focus on the summit region of Vesuvius. A comparison of 1D velocity profiles from the Fang shot on the summit of Erebus is compared with 1D models from three studies of Vesuvius in Figure 4.3. The studies by *Vilardo et al.* (1996), *De Natale et al.* (1998) and *Capuano et al.* (1999) were created using local or earthquake data. The *Lomax et al.* (2001) study interpolated data from previous 2D velocity models of the volcano. Stations that recorded the Fang shot, both east and west of the shot are shown on Figure 4.3. The velocities, especially in the near surface (surface to ~2 km below sea level) are significantly higher than the Vesuvius velocities. However, below this depth, they are comparable to the velocities found in the *Lomax et al.* (2001) study. These high velocities in the near-surface could be due to the shot location of Fang, which is on the eastern side of the volcano, and several kilometers away from the actual summit of the volcano.

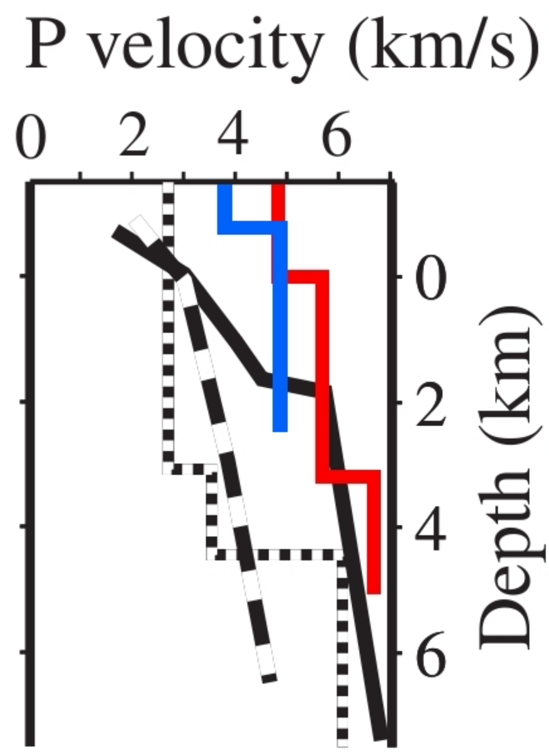

Figure 4.3: Comparison of velocity profiles from this study with studies from Vesuvius. The short-dashed line is from *Vilardo et al.* (1996), the long-dashed line is from *De Natale et al.* (1998) and *Capuano et al.* (1999), the solid line is from *Lomax et al.* (2001). The red line is the 1D profile east of the Fang shot, and the blue line is the 1D profile west of the Fang shot.

CONCLUSION

Overall, the 1D models are consistent with the *Dibble et al.* (1994) model which had a velocity of 4.3 km/s at the summit of Erebus that increased with depth at a rate of 0.1z. The 1D models developed for this work found a velocity of Erebus of $\sim$ 4 km/s. 2D model were quite poorly resolved as only three shots were used, and multiple models could be developed that resulted in similar fits of the calculated to the observed travel time data 4.4. Overall, these velocities are higher than normal for a volcano, especially one that has a shallow lava lake (*Aster et al.*, 2008). The high velocities could be due to an abundance of cumulate material as several large xenoliths have been recovered in recent years. The low velocities on the summit however, do approach the velocity of phonolitic lava at 2.7 km/s. Since the raypaths tended to be overwhelmed by the many summit shots, areas with many raypaths going in the same direction, such as in the near-surface both east and west of Mount Erebus, tend to be very smoothed. This shows up as a smearing effect of the velocity. Below Mount Terror, where there is an area of higher than background velocity, it is difficult to resolve the actual dimensions of that anomaly. However, due to the many raypaths that go through this region, we can still say that there is something there causing the raypaths to speed up. It could be a sill or even a solidified magma chamber, but it is difficult to determine based off of the results. Most importantly, despite the raypath limitations, the inversion model still provides a large improvement over the previous gradient model of the island. This is reflected in the increase of the RMS errors from 0.63 to 0.23. I believe that this study has provided evidence that this method works in an environment such as Antarctica, and the derived tomography velocity model will be very useful as a starting model for any future work in the region. That this method worked is also incentive for a study of this type to be repeated, where the length of line of stations and shot configuration can be altered to achieve more ideal raypath design. There have been several seismic experiments aimed at easily deploying instruments in the ice (e.g. (*Betterly et al.*, 2007)), which can be implemented in our study location to possibly extend the line of recorders. It is possible using this technique to ultimately image the Moho and increase our knowledge of the tectonics of the West Antarctic Rift System.

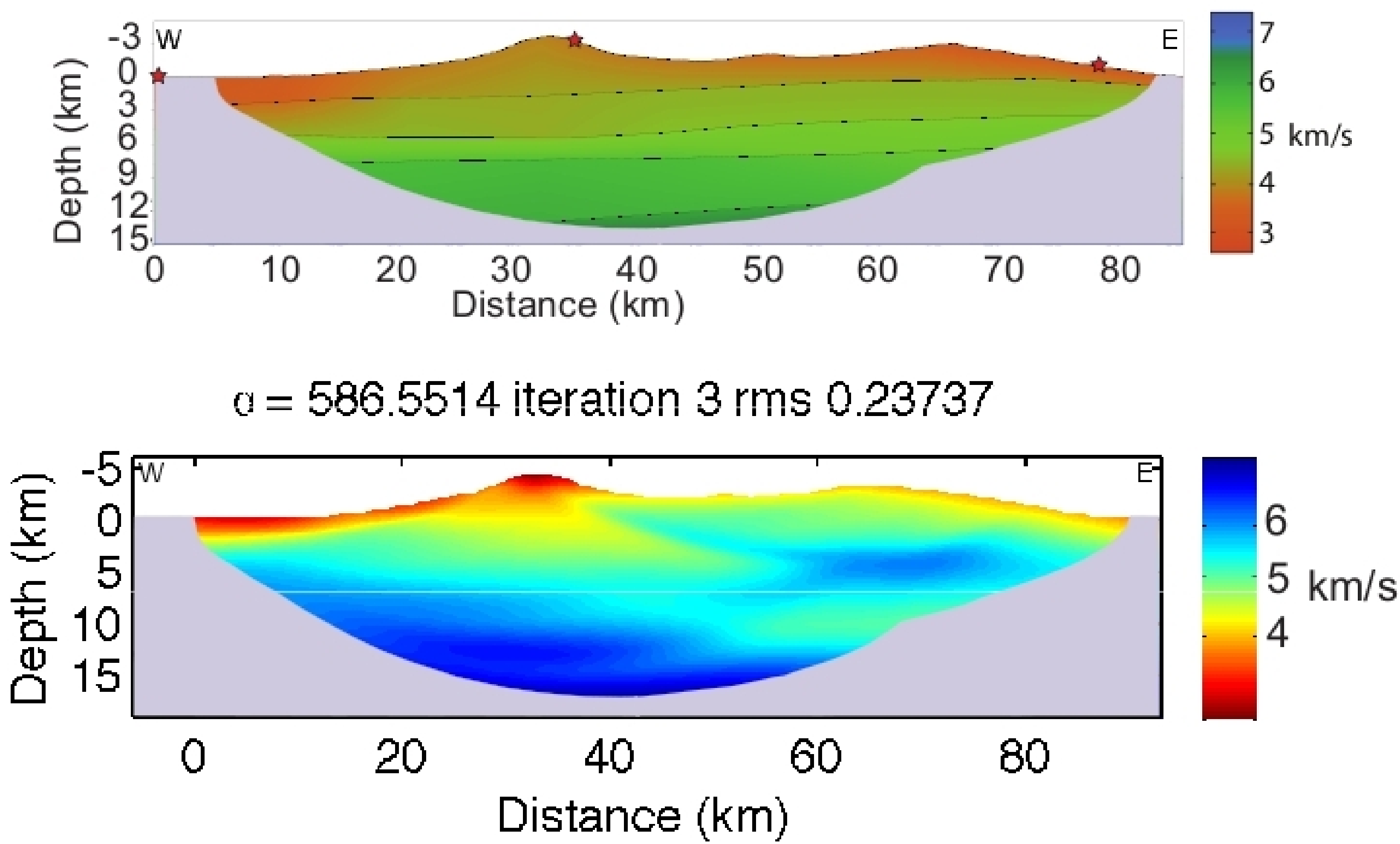

Figure 4.4: Comparison between the 2D and tomography models. In areas of poor raypath coverage, the inversion model is comparable to the 2D model. However, in areas of higher raypath coverage, such as in the near surface, especially in the summit region of Mount Erebus, the resolution greatly increases.

REFERENCES

Aster, R., S. Mah, P. Kyle, W. McIntosh, N. Dunbar, J. Johnson, M. Ruiz, and S. McNamara (2003), Very long period oscillations of Mount Erebus Volcano, *J. geophys. Res*, *108*(2522), 10–50.

Aster, R., D. Zandomeneghi, S. Mah, S. McNamara, D. Henderson, H. Knox, and K. Jones (2008), Moment tensor inversion of very long period seismic signals from strombolian eruptions of erebus volcano, *Journal of Volcanology and Geothermal Research*, *177*(3), 635 – 647, doi:10.1016/j.jvolgeores.2008.08.013.

Beaudoin, B., S. Uri, and T. Stern (1992), Characteristics and processing of seismic data collected on thick, floating ice: Results from the Ross Ice Shelf, Antarctica, *Geophysics*, *57*, 1359.

Behrendt, J. (1999), Crustal and lithospheric structure of the West Antarctic Rift System from geophysical investigations–a review, *Global and Planetary Change*, *23*(1-4), 25–44.

Betterly, S., M. Speece, R. Levy, D. Harwood, and S. Henrys (2007), A novel over-sea-ice seismic reflection survey in mcmurdo sound, antarctica, *Terra Antartica*, *14*(1/2), 97.

Capuano, P., U. Coppa, G. De Natale, F. Di Sena, C. Godano, and C. Troise (1999), A detailed analysis of some local earthquakes at somma-vesuvius, *Annals of Geophysics*, *42*(3).

Cooper, A., F. Davey, and J. Behrendt (1987), Seismic stratigraphy and structure of the Victoria Land basin, western Ross Sea, Antarctica, *The Antarctic continental margin: geology and geophysics of the western Ross Sea*, *5*, 27–76.

De Natale, G., P. Capuano, C. Troise, and A. Zollo (1998), Seismicity at somma-vesuvius and its implications for the 3d tomography of the volcano, *Journal of volcanology and geothermal research*, *82*(1-4), 175–197.

Dibble, R., B. OBrien, and C. Rowe (1994), The velocity structure of Mount Erebus, Antarctica, and its lava lake, *Volcanological and Environmental Studies of Mount Erebus, Antarctica, Antarct. Res. Ser*, *66*, 1–16.

Eschenbacher, A. (1998), Open-system degassing of a fractionating, alkaline magma, Mount Erebus, Ross Island, Antarctica, Master's thesis, New Mexico Institute of Mining and Technology.

Esser, R., P. Kyle, and W. McIntosh (2004), 40 Ar/39 Ar dating of the eruptive history of Mount Erebus, Antarctica: volcano evolution, *Bulletin of volcanology*, *66*(8), 671–686.

Ferraccioli, F., and E. Bozzo (1999), Inherited crustal features and tectonic blocks of the Transantarctic Mountains: An aeromagnetic perspective (Victoria Land, Antarctica), *Journal of geophysical research*, *104*(B11), 25,297–25.

Finotello, M., A. Nyblade, J. Julia, D. Wiens, and S. Anandakrishnan (2011), Crustal Vp–Vs ratios and thickness for Ross Island and the Transantarctic Mountain front, Antarctica, *Geophysical Journal International*.

Giggenbach, W., P. Kyle, and G. Lyon (1973), Present volcanic activity on Mount Erebus, Ross Island, Antarctica, *Geology*, *1*(3), 135.

Harpel, C., P. Kyle, R. Esser, W. McIntosh, and D. Caldwell (2004), 40 Ar/39 Ar dating of the eruptive history of Mount Erebus, Antarctica: summit flows, tephra, and caldera collapse, *Bulletin of volcanology*, *66*(8), 687–702.

Huerta, A., and D. Harry (2007), The transition from diffuse to focused extension: Modeled evolution of the West Antarctic Rift system, *Earth and Planetary Science Letters*, *255*(1-2), 133–147.

Kyle, P., R. Dibble, and J. Giggenbach, W.F. Keys (1982), *Volcanic activity associated with the anorthoclase phonolite lava lake, Mount Erebus, Antarctica*, Ohio State University, Institute of Polar Studies.

Kyle, P., L. Sybeldon, W. McIntosh, K. Meeker, and R. Symonds (1994), Sulfur dioxide emission rates from Mount Erebus, Antarctica, *Volcanological and Environmental Studies of Mount Erebus, Antarctica*, *66*, 69–82.

Lawrence, J., D. Wiens, A. Nyblade, S. Anandakrishnan, P. Shore, and D. Voigt (2006), Crust and upper mantle structure of the Transantarctic Mountains and surrounding regions from receiver functions, surface waves, and gravity: implications for uplift models, *Geochemistry Geophysics Geosystems*, *7*(10), Q10,011.

Lomax, A., A. Zollo, P. Capuano, and J. Virieux (2001), Precise, absolute earthquake location under somma–vesuvius volcano using a new three-dimensional velocity model, *Geophysical Journal International*, *146*(2), 313–331.

Luetgert, J. (1988a), Users manual for R1D84 interactive modeling of one-dimensional velocity-depth functions, *US Geological Survey Open File Report*, *88*(247), 30.

Luetgert, J. (1992), MacRay-Interactive two-dimensional seismic raytracing for the Macintosh, *US Geological Survey Open File Report*, *92*(356), 1–2.

McGinnis, L., D. Wilson, W. Burdelik, and T. Larson (1983), Crust and upper mantle study of mcmurdo sound, *Antarctic Earth Science*, pp. 204–208.

McGinnis, L., R. Bowen, J. Erickson, B. Allred, and J. Kreamer (1985), East-West Antarctic boundary in McMurdo Sound, *Tectonophysics*, *114*(1-4), 341–356.

Nardini, I., P. Armienti, S. Rocchi, L. Dallai, and D. Harrison (2009), Sr–Nd–Pb–He–O Isotope and Geochemical Constraints on the Genesis of Cenozoic Magmas from the West Antarctic Rift, *Journal of Petrology*, *50*(7), 1359.

Northey, D., C. Brown, D. Christoffel, H. Wong, and P. Barrett (1975), A continuous seismic profiling survey in mcmurdo sound, antarctica, *Dry Valley Drilling Project bulletin no*, *5*, 167–179.

Oppenheimer, C., A. Lomakina, P. Kyle, N. Kingsbury, and M. Boichu (2009), Pulsatory magma supply to a phonolite lava lake, *Earth and Planetary Science Letters*, *284*(3-4), 392–398.

Rocchi, S., P. Armienti, and G. Di Vincenzo (2005), No plume, no rift magmatism in the West Antarctic Rift, *Plates, Plumes, and Paradigms*, pp. 435–447.

Rocholl, A., M. Stein, M. Molzahn, S. Hart, and G. Worner (1995), Geochemical evolution of rift magmas by progressive tapping of a stratified mantle source beneath the Ross Sea Rift, Northern Victoria Land, Antarctica, *Earth and Planetary Science Letters*, *131*(3-4), 207–224.

Rowe, C. (1988), Seismic velocity structure and seismicity on Mount Erebus Volcano, Ross Island, Antarctica, Master's thesis, University of Alaska, Fairbanks.

Stern, T., F. Davey, and G. Delisle (1991), Lithospheric flexure induced by the load of the ross archipelago, southern victoria land, antarctica, *Geological Evolution of Antarctica*, pp. 323–328.

Um, J., and C. Thurber (1987), A fast algorithm for two-point seismic ray tracing, *Bulletin of the Seismological Society of America*, *77*(3), 972.

Vilardo, G., G. De Natale, G. Milano, and U. Coppa (1996), The seismicity of mt. vesuvius, *Tectonophysics*, *261*(1-3), 127–138.

Watson, T., A. Nyblade, D. Wiens, S. Anandakrishnan, M. Benoit, P. Shore, D. Voigt, and J. VanDecar (2006), P and S velocity structure of the upper mantle beneath the Transantarctic Mountains, East Antarctic craton, and Ross Sea from travel time tomography, *Geochemistry Geophysics Geosystems*, *7*(7), Q07,005.

Wilson, G., D. Damaske, H. Möller, K. Tinto, and T. Jordan (2007), The geological evolution of southern McMurdo Soundnew evidence from a high-resolution aeromagnetic survey, *Geophysical Journal International*, *170*(1), 93–100.

Worner, G. (1999), Lithospheric dynamics and mantle sources of alkaline magmatism of the Cenozoic West Antarctic Rift System, *Global and Planetary Change*, *23*(1-4), 61–77.

APPENDIX A

SHOT DATA

Shot Point ID	Shot Point Name	Time (UTC) yyyy:jd:hr:mn:ss	latitude (WGS84)	longitude (WGS84)	elevation (m)	type of source	size (kg)	depth below surface (m)	# of holes
4000	Windless Bight	2008:346:01:40:00	77.74667	167.42534	38.774	ANFO	500	15	4
4001	Cape Crozier	2008:346:00:17:00	77.52047	169.55677	23.408	ANFO	600	14.5	5
4002	Cape Royd	2008:345:05:17:00	77.57793	165.81121	-0.123	dynamite	200	water	1
4003	Crozier 2	2008:357:02:27:00	77.53207	169.07915	792.162	ANFO	500	15	5
4004	FANG	2008:355:21:51:00	77.49550	167.23412	2928.494	ANFO	300	15	3
4005	Cones2	2008:356:09:00:00	77.53486	167.10207	3494.562	ANFO	100	6.0, 6.13, 7.4	3
4006	Cones	2008:356:08:23:00	77.52857	167.08469	3439.634	ANFO	200	14.9	2
4007	CORR13	2008:356:07:50:00	77.51817	167.08751	3294.538	ANFO	75	20	1
4008	Tramsw 2	2008:356:09:45:00	77.51977	167.11968	3421.712	ANFO	75	6.15, 6.8	2
4009	Sunshine Valley CornerSW	2008:359:00:30:00	77.51650	167.06509	3225.665	ANFO	100	5.5, 5.8, 7.9	3
4010	HoleH	2008:358:20:55:00	77.51334	167.15366	3424.817	ANFO	75	7.8, 8.15	2
4011	Stinky (13)	2008:358:23:49:00	77.51361	167.17945	3424.82	ANFO	75	8.1, 8.5	2
4012	Black (19)	2008:357:05:02:00	77.52920	167.22458	3461.882	ANFO	100	7.5	2
4013	Tower (17)	2008:357:05:28:00	77.52416	167.22520	2928.494	ANFO	100	7.8, 8.7	2
4014	Fog (15)	2008:357:05:55:00	77.51781	167.20687	3466.01	ANFO	100	8.0, 8.6	2
4015	Stuck (11)	2008:358:23:27:00	77.50585	167.17907	3351.054	ANFO	100	6.2 7.1	2

APPENDIX B

BROADBAND STATION DATA

Receiver ID	Latitude (WGS84)	Longitude (WGS84)	Elevation (m)	Serial # of data logger	Data logger manufacturer	Data logger model #	Sensor manufacturer	Sensor model number
1001	-77.5245	166.964417	2359	9297	RefTek	RT-130	Guralp	40-T
1002	-77.548567	166.97205	2114	9892	RefTek	RT-130	Guralp	40-T
1003	-77.508133	166.931617	2001	9866	RefTek	RT-130	Guralp	40-T
1004	-77.4965	166.965167	2143	9873	RefTek	RT-130	Guralp	40-T
1005	-77.492167	167.051167	2452	9848	RefTek	RT-130	Guralp	40-T
1006	-77.492083	167.105167	2583	9915	RefTek	RT-130	Guralp	40-T
1007	-77.5628	166.9777	1780	995F	RefTek	RT-130	Guralp	40-T
1008	-77.504183	167.336983	2495	990B	RefTek	RT-130	Guralp	40-T
1009*	-77.542717	166.1646	16	995D	RefTek	RT-130	Guralp	40-T
1010	-77.55235	167.282717	2361	92C8	RefTek	RT-130	Guralp	40-T
1011	-77.517917	167.151567	3494	976C	RefTek	RT-130	Guralp	40-T
1012	-77.515117	167.109217	3373	985B	RefTek	RT-130	Guralp	40-T
1013	-77.547933	167.360350	1979	9868	RefTek	RT-130	Guralp	40-T
1014	-77.515417	167.194300	3437	944B	RefTek	RT-130	Guralp	40-T
1015	-77.537333	167.144517	3405	9859	RefTek	RT-130	Guralp	40-T
1016	-77.511700	167.079967	3274	92D9	RefTek	RT-130	Guralp	40-T
1017	-77.533283	167.208633	3437	995A	RefTek	RT-130	Guralp	40-T
1018	-77.524883	167.197683	3566	995B	RefTek	RT-130	Guralp	40-T
1019	-77.505250	167.177533	3290	988F	RefTek	RT-130	Guralp	40-T
1020	-77.525333	167.104700	3493	953B	RefTek	RT-130	Guralp	40-T
1021	-77.500167	167.225217	2951	984D	RefTek	RT-130	Guralp	40-T
1022	-77.518967	167.224267	3455	9920	RefTek	RT-130	Guralp	40-T
1023	-77.523383	167.050150	3236	9343	RefTek	RT-130	Guralp	40-T
1024	-77.575517	167.124017	1540	9876	RefTek	RT-130	Guralp	40-T

APPENDIX C

SHORT-PERIOD STATION DATA

Receiver ID	Latitude (WGS84)	Longitude (WGS84)	Elevation (m)	Serial # of data logger	Data logger manufacturer	Data logger model #	Sensor manufacturer	Sensor model number
2001	-77.53994	166.30038	173	9777	RefTek	RT-130	Mark Products	L-28
2002	-77.53737	166.40999	398	9142	RefTek	RT-130	Mark Products	L-28
2003	-77.5357	166.52064	633	9095	RefTek	RT-130	Mark Products	L-28
2004	-77.53352	166.63891	921	9914	RefTek	RT-130	Mark Products	L-28
2005	-77.53053	166.75738	1242	9805	RefTek	RT-130	Mark Products	L-28
2006	-77.52926	166.87078	1680	9553	RefTek	RT-130	Mark Products	L-28
2007	-77.52702	167.37993	2091	9310	RefTek	RT-130	Mark Products	L-28
2008	-77.52374	167.50133	1786	949A	RefTek	RT-130	Mark Products	L-28
2009	-77.52338	167.64172	1491	9811	RefTek	RT-130	Mark Products	L-28
2010	-77.5225	167.77194	1583	9260	RefTek	RT-130	Mark Products	L-28
2011	-77.52202	167.92625	2048	92D5	RefTek	RT-130	Mark Products	L-28
2012	-77.51818	168.05618	1808	938B	RefTek	RT-130	Mark Products	L-28
2013	-77.51552	168.204	2007	92B4	RefTek	RT-130	Mark Products	L-28
2014	-77.51165	168.34747	2501	9844	RefTek	RT-130	Mark Products	L-28
2015	-77.51547	168.48471	2925	92BE	RefTek	RT-130	Mark Products	L-28
2016	-77.51452	168.62449	2860	924C	RefTek	RT-130	Mark Products	L-28
2017	-77.50844	168.75416	2317	92D1	RefTek	RT-130	Mark Products	L-28
2018	-77.50433	168.89784	1841	9342	RefTek	RT-130	Mark Products	L-28
2019	-77.50288	169.0452	1346	9099	RefTek	RT-130	Mark Products	L-28
2020	-77.4971	169.17777	643	913F	RefTek	RT-130	Mark Products	L-28
3021	-77.5099	167.16557	3390	978F	RefTek	RT-130	Mark Products	L-28
3022	-77.50983	167.14503	3394	978A	RefTek	RT-130	Mark Products	L-28
3023	-77.5121	167.13493	3387	9874	RefTek	RT-130	Mark Products	L-28
3024	-77.51435	167.12445	3366	929D	RefTek	RT-130	Mark Products	L-28
3025	-77.51212	167.11406	3342	92D6	RefTek	RT-130	Mark Products	L-28
3026	-77.51659	167.093	3345	9240	RefTek	RT-130	Mark Products	L-28
3027	-77.50987	167.20732	3361	92A4	RefTek	RT-130	Mark Products	L-28
3028	-77.51208	167.19729	3382	9828	RefTek	RT-130	Mark Products	L-28
3030	-77.52112	167.09288	3383	9896	RefTek	RT-130	Mark Products	L-28
3031	-77.51889	167.10345	3377	945A	RefTek	RT-130	Mark Products	L-28
3032	-77.51606	167.10916	3375	9140	RefTek	RT-130	Mark Products	L-28
3033	-77.51213	167.1762	3399	92EA	RefTek	RT-130	Mark Products	L-28

3034	-77.51207	167.15577	3408	92F0	RefTek	RT-130	Mark Products	L-28
3035	-77.51439	167.14486	3417	92E4	RefTek	RT-130	Mark Products	L-28
3036	-77.51661	167.13501	3421	92A0	RefTek	RT-130	Mark Products	L-28
3037	-77.51859	167.12402	3446	9780	RefTek	RT-130	Mark Products	L-28
3038	-77.52116	167.11426	3449	92E2	RefTek	RT-130	Mark Products	L-28
3039	-77.52344	167.12413	3573	92A5	RefTek	RT-130	Mark Products	L-28
3040	-77.52567	167.11426	3539	92C9	RefTek	RT-130	Mark Products	L-28
3041	-77.52791	167.1031	3512	9261	RefTek	RT-130	Mark Products	L-28
3042	-77.53006	167.09288	3512	9559	RefTek	RT-130	Mark Products	L-28
3043	-77.52342	167.10374	3456	91F7	RefTek	RT-130	Mark Products	L-28
3044	-77.52564	167.09313	3454	9917	RefTek	RT-130	Mark Products	L-28
3045	-77.51438	167.20756	3412	9294	RefTek	RT-130	Mark Products	L-28
3046	-77.51662	167.19693	3456	9290	RefTek	RT-130	Mark Products	L-28
3047	-77.51894	167.18651	3516	9283	RefTek	RT-130	Mark Products	L-28
3048	-77.51657	167.17658	3468	983D	RefTek	RT-130	Mark Products	L-28
3049	-77.51435	167.16609	3429	9803	RefTek	RT-130	Mark Products	L-28
3050	-77.51434	167.18666	3425	9912	RefTek	RT-130	Mark Products	L-28
3051	-77.51882	167.16587	3519	9869	RefTek	RT-130	Mark Products	L-28
3052	-77.52333	167.16593	3699	944C	RefTek	RT-130	Mark Products	L-28
3053	-77.52119	167.17656	3591	9241	RefTek	RT-130	Mark Products	L-28
3054	-77.51892	167.20757	3480	983E	RefTek	RT-130	Mark Products	L-28
3055	-77.52118	167.21802	3481	91E5	RefTek	RT-130	Mark Products	L-28
3056	-77.52329	167.18687	3607	990D	RefTek	RT-130	Mark Products	L-28
3057	-77.51702	167.21719	3446	92F7	RefTek	RT-130	Mark Products	L-28
3058	-77.52345	167.20699	3544	9891	RefTek	RT-130	Mark Products	L-28
3059	-77.52105	167.19776	3547	9446	RefTek	RT-130	Mark Products	L-28
3060	-77.51439	167.10342	3354	924A	RefTek	RT-130	Mark Products	L-28
3061	-77.51672	167.15409	3477	9864	RefTek	RT-130	Mark Products	L-28
3062	-77.52016	167.13886	3548	9512	RefTek	RT-130	Mark Products	L-28
3063	-77.5189	167.14537	3515	947D	RefTek	RT-130	Mark Products	L-28
3064	-77.52115	167.15534	3604	9491	RefTek	RT-130	Mark Products	L-28
3065	-77.52562	167.13679	3633	947A	RefTek	RT-130	Mark Products	L-28
3066	-77.52785	167.14371	3712	924E	RefTek	RT-130	Mark Products	L-28
3067	-77.50768	167.15874	3384	9453	RefTek	RT-130	Mark Products	L-28
3068	-77.53487	167.0934	3452	930A	RefTek	RT-130	Mark Products	L-28
3069	-77.53218	167.10373	3527	9461	RefTek	RT-130	Mark Products	L-28
3070	-77.52748	167.12784	3642	995C	RefTek	RT-130	Mark Products	L-28
3071	-77.53011	167.11364	3556	9466	RefTek	RT-130	Mark Products	L-28
3072	-77.53485	167.113	3469	9238	RefTek	RT-130	Mark Products	L-28
3073	-77.50758	167.17648	3360	9292	RefTek	RT-130	Mark Products	L-28
3074	-77.50765	167.19571	3349	990F	RefTek	RT-130	Mark Products	L-28
3075	-77.50758	167.11426	3313	92A1	RefTek	RT-130	Mark Products	L-28
3076	-77.50991	167.10369	3320	92DD	RefTek	RT-130	Mark Products	L-28
3077	-77.53509	167.15373	3518	929B	RefTek	RT-130	Mark Products	L-28
3078	-77.53423	167.17502	3511	9293	RefTek	RT-130	Mark Products	L-28
3079	-77.5324	167.12409	3557	9334	RefTek	RT-130	Mark Products	L-28
3080	-77.5346	167.13564	3521	9791	RefTek	RT-130	Mark Products	L-28
3081	-77.53256	167.14668	3626	980E	RefTek	RT-130	Mark Products	L-28

3082	-77.52963	167.09758	3529	986C	RefTek	RT-130	Mark Products	L-28
3083	-77.51224	167.09409	3331	9C30	RefTek	RT-130	Mark Products	L-28
3084	-77.51233	167.06478	3235	943F	RefTek	RT-130	Mark Products	L-28
3085	-77.52435	167.23053	3458	9924	RefTek	RT-130	Mark Products	L-28
3086	-77.52793	167.18616	3601	9462	RefTek	RT-130	Mark Products	L-28
3087	-77.53258	167.1859	3515	9237	RefTek	RT-130	Mark Products	L-28
3088	-77.53063	167.17526	3627	9926	RefTek	RT-130	Mark Products	L-28
3089	-77.50752	167.13603	3369	9245	RefTek	RT-130	Mark Products	L-28
3090	-77.53096	167.14265	3678	9009	RefTek	RT-130	Mark Products	L-28
3091	-77.52572	167.07326	3426	956F	RefTek	RT-130	Mark Products	L-28
3092	-77.52332	167.14515	3658	925D	RefTek	RT-130	Mark Products	L-28
3093	-77.52562	167.21814	3494	92F4	RefTek	RT-130	Mark Products	L-28
3094	-77.52788	167.20786	3515	909A	RefTek	RT-130	Mark Products	L-28
3095	-77.53015	167.19658	3527	9560	RefTek	RT-130	Mark Products	L-28
3096	-77.53007	167.2178	3488	92C4	RefTek	RT-130	Mark Products	L-28
3097	-77.52956	167.23168	3439	92AC	RefTek	RT-130	Mark Products	L-28
3098	-77.52537	167.15936	3654	991C	RefTek	RT-130	Mark Products	L-28
3099	-77.50123	167.20651	3037	92AB	RefTek	RT-130	Mark Products	L-28

APPENDIX D

SHOT GATHERS

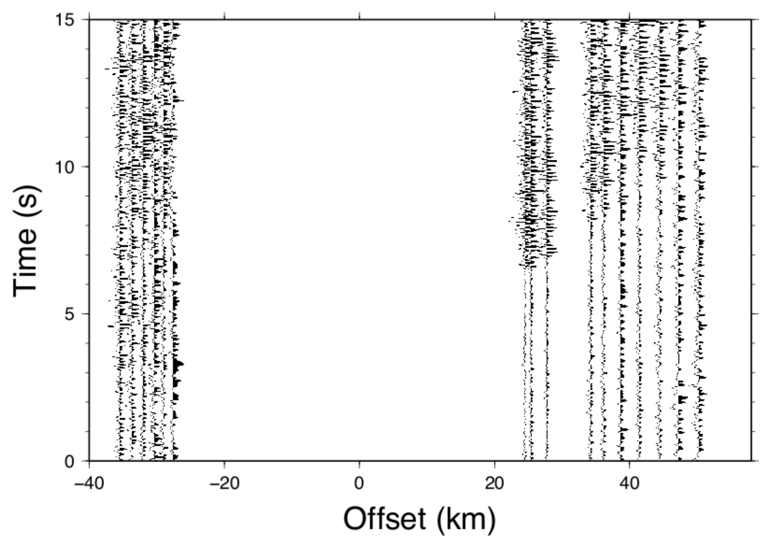

Figure D.1: Shot gather from the Windless Bight (4000) shot

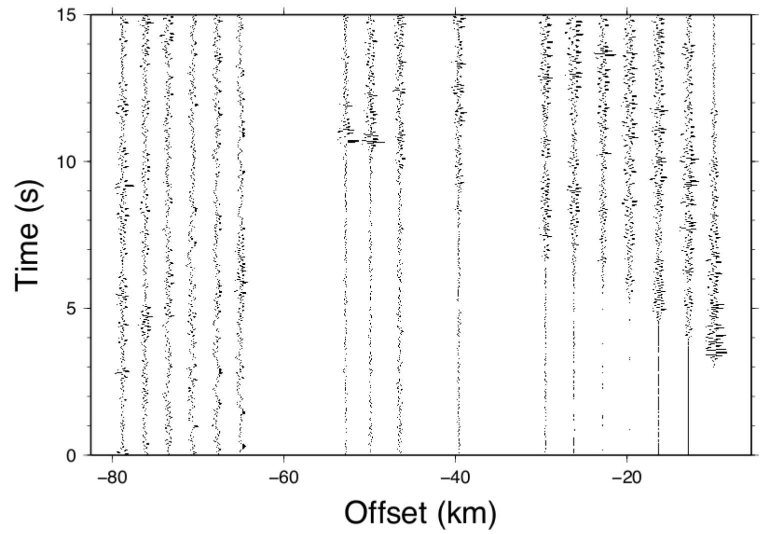

Figure D.2: Shot gather from the Cape Crozier (4001) shot

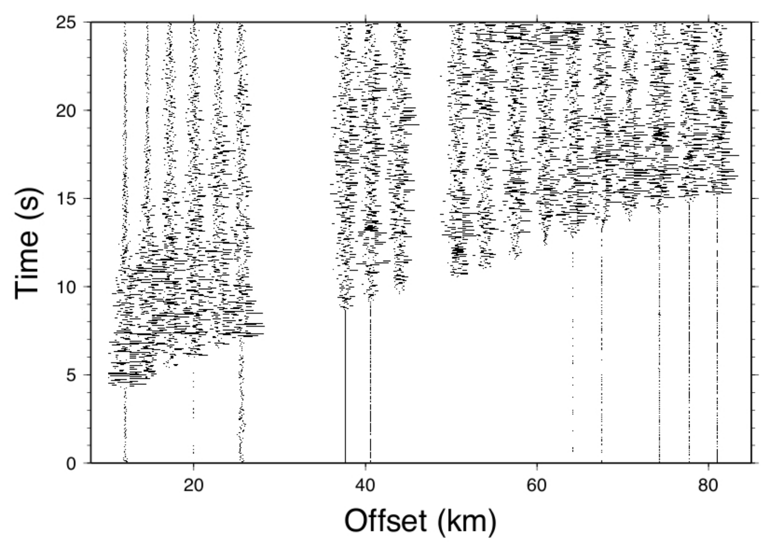

Figure D.3: Shot gather from the Cape Royds (4002) shot

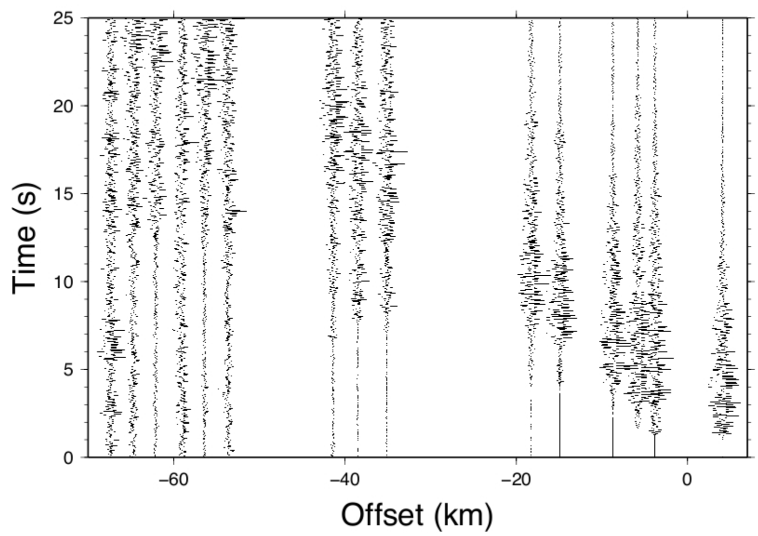

Figure D.4: Shot gather from the Crozier 2 (4003) shot

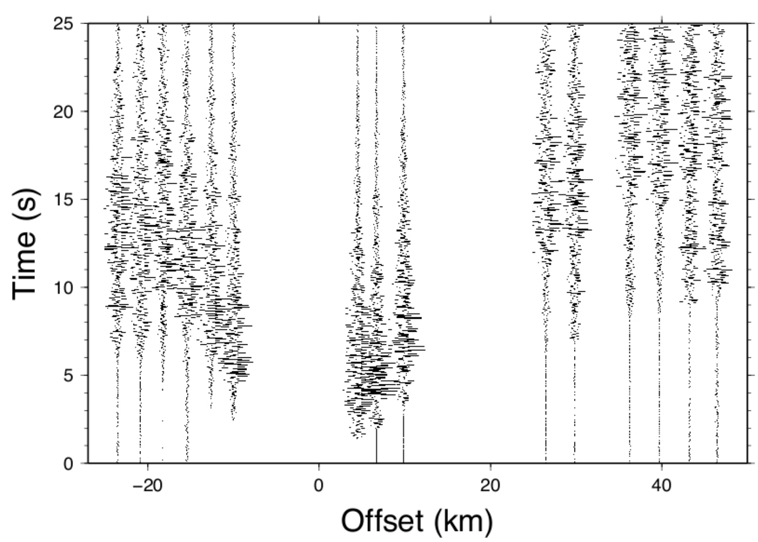

Figure D.5: Shot gather from the FANG (4004) shot

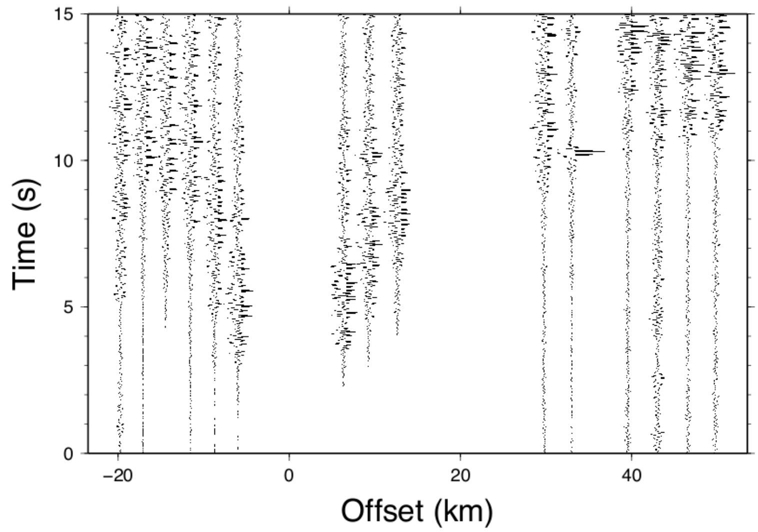

Figure D.6: Shot gather from the Cones2 (4005) shot

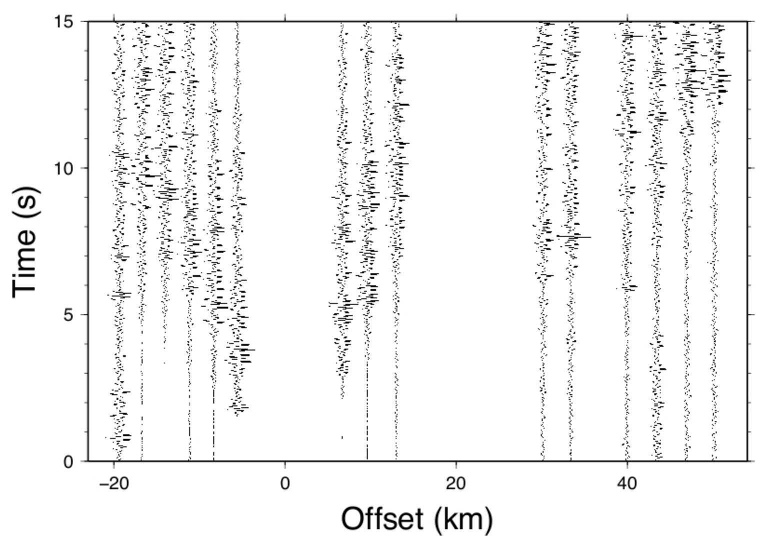

Figure D.7: Shot gather from the Cones (4006) shot

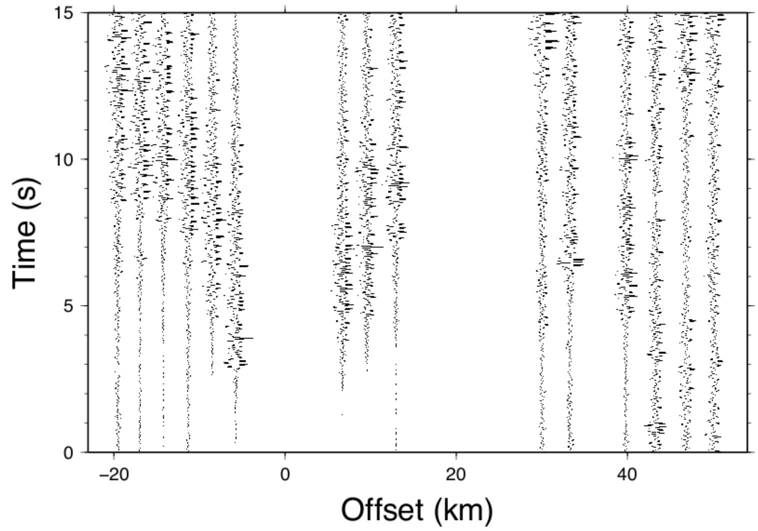

Figure D.8: Shot gather from the CORR13 (4007) shot

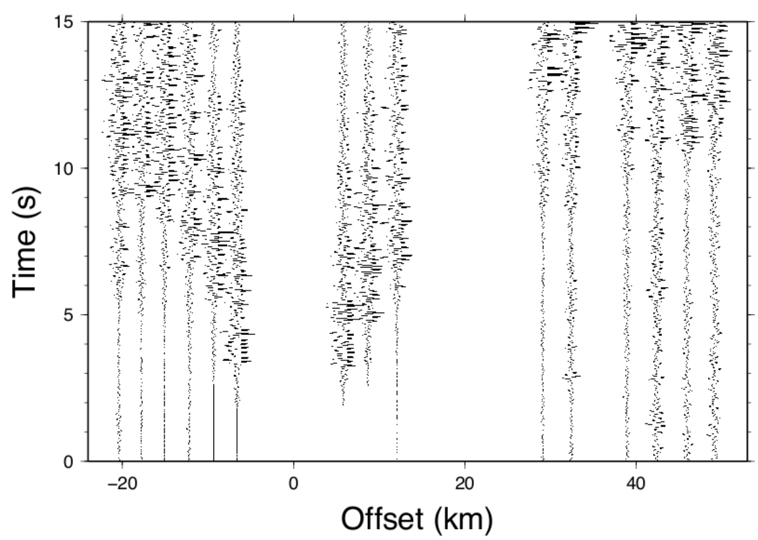

Figure D.9: Shot gather from the Transw 2 (4008) shot

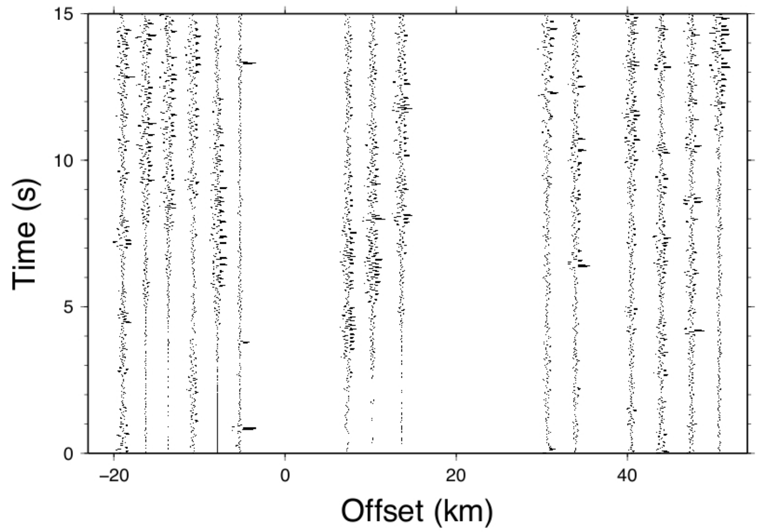

Figure D.10: Shot gather from the Sunshine Valley Corner SW (4009) shot

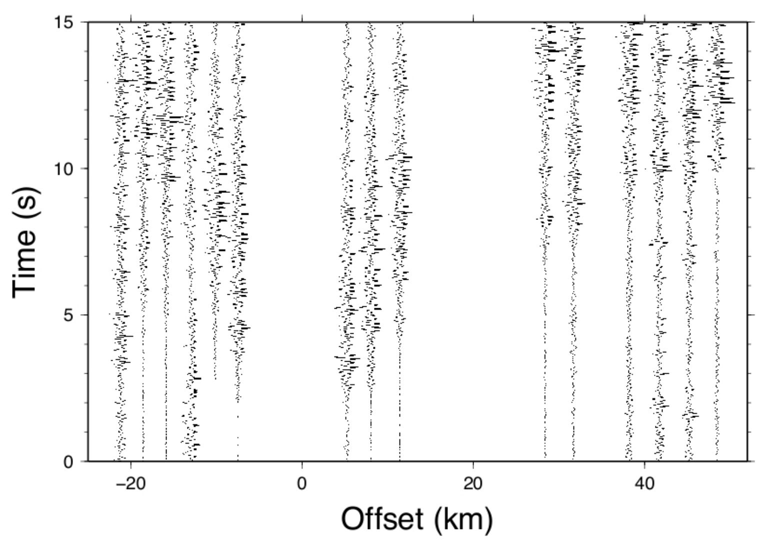

Figure D.11: Shot gather from the HoleH (4010) shot

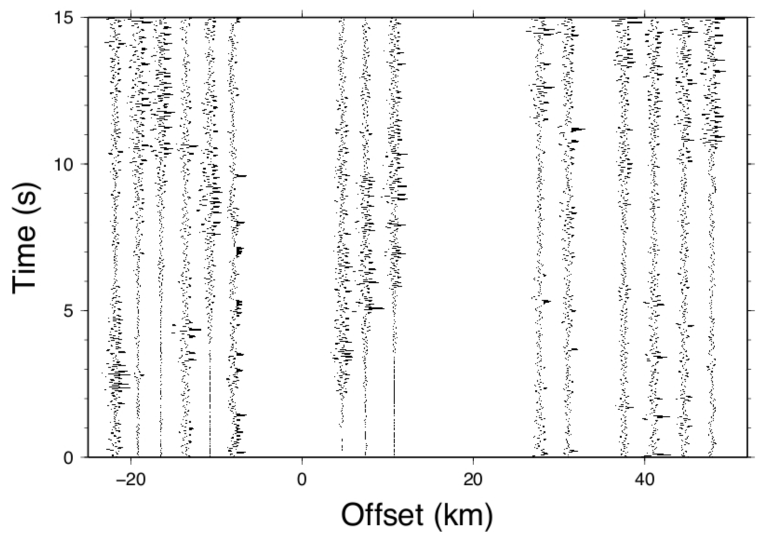

Figure D.12: Shot gather from the Stinky (13) (4011) shot

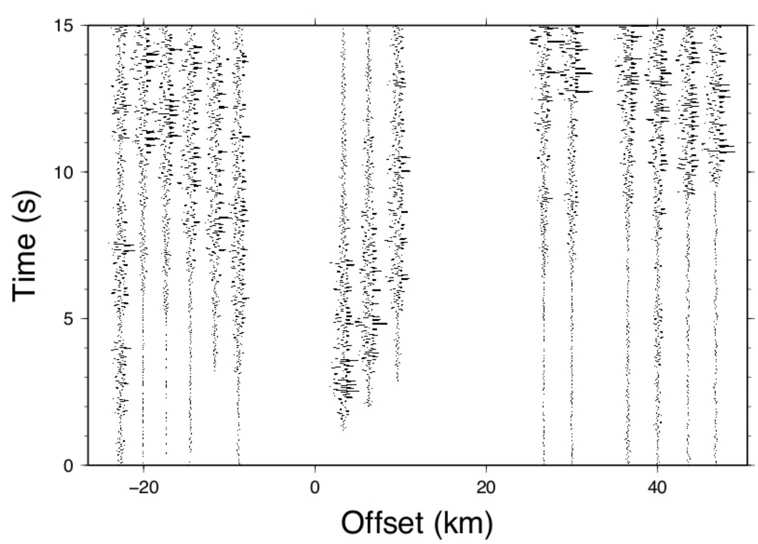

Figure D.13: Shot gather from the Black (19) (4012) shot

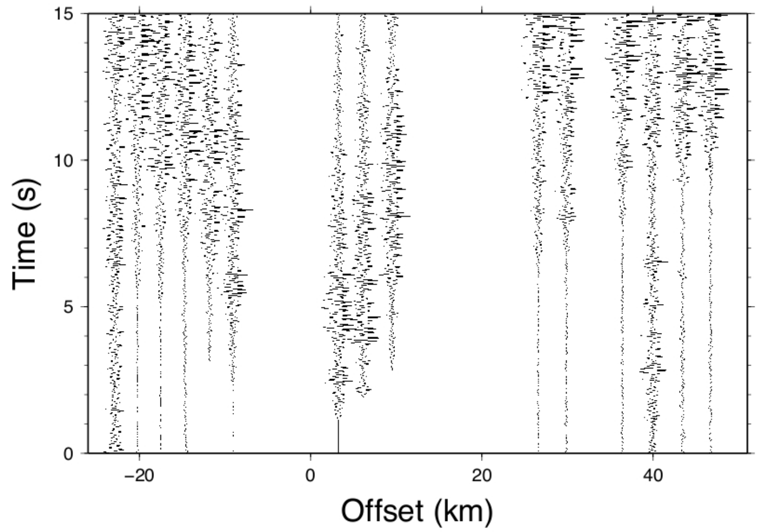

Figure D.14: Shot gather from the Tower (17) (4013) shot

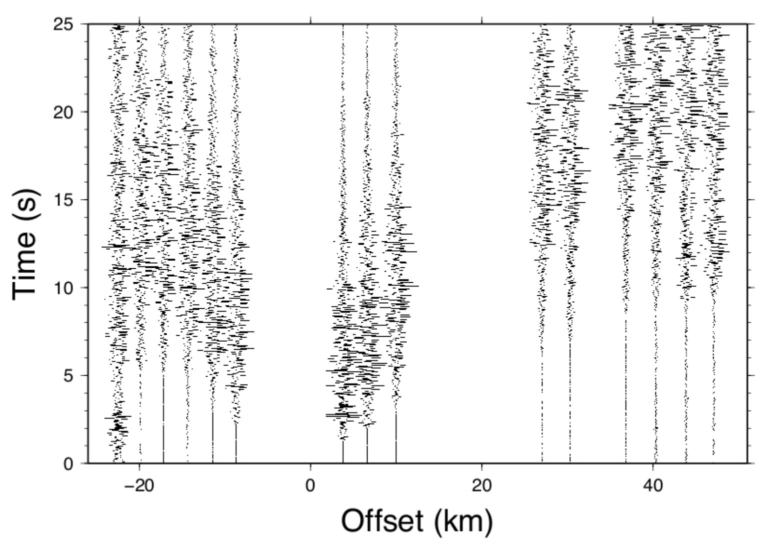

Figure D.15: Shot gather from the Fog (15) (4014) shot

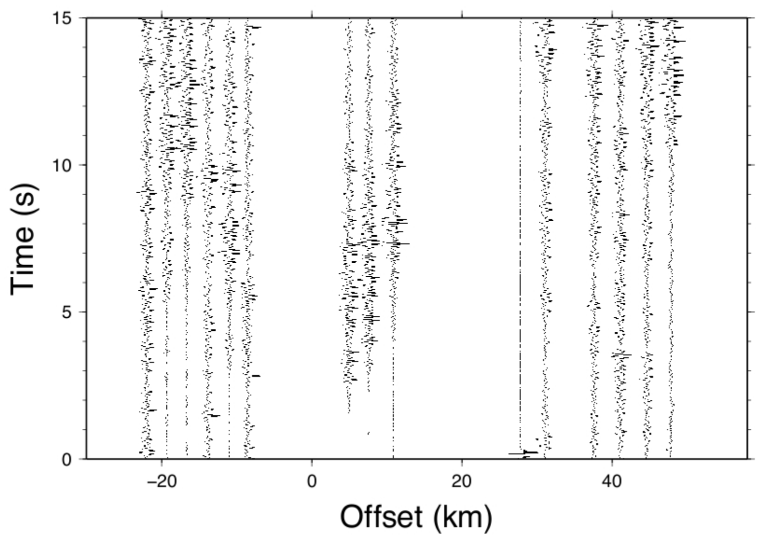

Figure D.16: Shot gather from the Stuck (11) (4015) shot

APPENDIX E

TOMOGRAPHIC INVERSION CODE

```
%Erebus 2-d inverse code
clear; clc;


%Erebus long line data
load projdata1
ttobs=ttobs_proj;
stdw=stds_proj;
range=abs(xrs-xss);

%noise level (s)
NOISE = 0.05;

XFAC=2.2;
CONV=1e-5;

%number of ray tracing iterations
NIT=25;

%number of nonlinear inverse (GN, regularized) interations
MAXITER=3;

%grid size (km)
gridx=87;
gridz=13;

%size of velocity model edge padding (km)
vpad=6;

%model grid spacing (km)
gs=0.5;

%number of nodes
nx=round((gridx+2*vpad)/gs);
nz=round((gridz+2*vpad)/gs);

%dimensions of inverse problem (model, data);
```

```
N=nx*nz;
M=length(xss);

%number of segments per ray
nseg=2*nx;

%coordinates of velocity nodes
xv=linspace(-vpad,gridx+vpad,nx);
zv=linspace(-vpad,gridz+vpad,nz);

%initial gradient model km/s
v0=4;
v=v0*ones(nz,nx);
[xx,zz]=meshgrid(xv,zv');
k=0.1;
vgrad=(zz+3.7)*k;
v=v+vgrad;
vsmooth=v;

%starting slowness model for inversion
s=1./vsmooth;
m=reshape(s,nx*nz,1);

% %checkerboard test model superposition
% csize=5;
% mmm=round(nz/csize)*csize;
% nnn=round(nx/csize)*csize;
% ck=checkerboard(csize,mmm/csize,nnn/csize);
% ind=find(ck > 0);
% %[i,j]=ind2sub(size(ck),ind);
% ck(ind)=1.;
% ck=ck-0.5;

% %velocity model to be revealed in inversion
% v=v+ck(1:nz,1:nx)*0.25;

[xnm,znm]=meshgrid(xv,zv);
xni=(-5:.1:gridx+5)';
zni=(-5:.1:gridz+5)';
[xnim,znim]=meshgrid(xni,zni);

vi=interp2(xnm,znm,v,xnim,znim,'spline');

%plot starting model and raypaths
figure(1)
bookfonts
imagesc(xv,zv,vi);
colormap(flipud(jet));
colorbar
xlabel('km');
```

```
ylabel('km');

rpnum=0;
rpinits=zeros(length(xss),nseg+1,2);
    for nr=1:length(xrs)
        rpnum=rpnum+1;


    %set up an initial circular path set for the starting gradient ...
       model
    reverse=false;
    D=xrs(nr)-xss(nr);
    %right - left ray
    Δz=zrs(nr)-zss(nr);
    if (D<0)
        D=-D;
        Δz=-Δz;
        reverse=true;
    end
    v0=4.0;
    [r,h,theta0]=getcircray(v0,D,k);
    tmin=(pi/2-theta0);
    theta=linspace(-tmin,tmin,nseg+1)';
    if reverse==true; theta=-theta; end;
    xp=r*sin(theta)+xss(nr)+(xrs(nr)-xss(nr))/2;
    dx=r*sin(theta)-r*sin(theta(1));
    zp=r*cos(theta)+h+zss(nr)+Δz*dx/D;
    rpinits(rpnum,:,:)=[xp,zp];

    end

[tt,raypaths,it]=get_raypaths(M,xv,zv,v,rpinits,XFAC,CONV,NIT);
raypaths_store=raypaths;
tts_store=tt;


M=length(tts_store);

figure(1)
hold on
for i=1:rpnum
    raypath(:,:)=raypaths_store(i,:,:);
    %plot raypaths
plot(raypath(:,1),raypath(:,2),'w-','linewidth',2);
end

%plot velocity model nodes
 plot(xx,zz,'k.');
%plot sources
plot(xrs,zrs,'ro');
```

```
load Profile_Elevs.mat
Tx=sqrt(X.^2+Y.^2);
for i=1:length(xni)
evi(i,1)=-1.16*interp1(Tx,Z,xni(i))/1000;
end

ind=find(isnan(evi));
evi(ind)=0;

plot(xni,evi,'k');
hold off

%interpolate the velocity field for plotting
vi=interp2(xnm,znm,v,xnim,znim,'spline');

%create mask for later plotting
vmask=ones(size(vi));
for i=1:length(xni)
    ind=find(zni>evi(i),length(zni));
    vmask(1:ind(1),i)=0;
end


% plot(range+10,-stelev/1000,'r*');
axis ij
%axis([-150 1750 -150 1750]);
  drawnow;

%construct the second--order regularization matrix
L2=sparse(N,N);
k=1;
for j=1:nx
    for i=1:nz;
        mtmp=zeros(nz,nx);
        if i>1; mtmp(i-1,j)=1; end;
        if j>1; mtmp(i,j-1)=1; end;
        if i<nz; mtmp(i+1,j)=1; end;
        if j<nx; mtmp(i,j+1)=1; end;
        L2(k,:)=reshape(mtmp,N,1);
        k=k+1;
    end
end
%fix for edges and corners
for i=1:N
    L2(i,i)=-sum(L2(i,:));
end

%construct a horizontal first--order regularization matrix
L1h=sparse(N,N);
```

```
k=1;
for j=1:nx
    for i=1:nz;
        mtmp=zeros(nz,nx);
        %if i>1; mtmp(i-1,j)=1; end;
        if j==1 mtmp(i,nx)=1; end;
        if j>1; mtmp(i,j-1)=1; end;
        L1h(k,:)=reshape(mtmp,N,1);
        k=k+1;
    end
end
for i=1:N
    L1h(i,i)=-sum(L1h(i,:));
end


%hybrid roughening matrix
L=L2+3*L1h;

%L=sparse(eye(N))+L1;

%piter corresponds to a particular choice of alpha
piter=0;
%fliplr to calculate most regularized models first
piterexprange=fliplr(2:0.5:5.5);
NPITER=length(piterexprange);
[mm,nn]=size(vi);
vstore=zeros(NPITER,mm,nn);
alphasq=zeros(NPITER,1);
misfit=zeros(NPITER,MAXITER);
mnorm=zeros(NPITER,MAXITER);
mrms=zeros(NPITER,MAXITER);

%regularization/solving loop
for piterexp=piterexprange

piter=piter+1;

for iter=1:MAXITER

    disp('calculating Jacobian and ray tracing')
  [J,ttcal]=get_j(N,M,xv,zv,v,raypaths_store);
    disp('done calculating Jacobian and ray tracing')
    figure(100+10*(piter-1)+iter)
%plot data fit for initial model
plot(range,ttcal,'*');
hold on
errorbar(range,ttobs,stdw,'r.');
hold off
ylabel('T_{obs}, T_{calc}')
```

```
xlabel('Range (km)');
title(['Iteration: ',num2str(iter),' RMS error: ...
    ',num2str(norm(ttobs-ttcal)/sqrt(M))]);

%save raypaths to start the next iteration
  rpinit=raypaths_store;

%set the regularization tradeoff parameter here
  if (iter == 1)
    rparam=norm(full(J))*10^piterexp;
  end

  alphasq(piter)=rparam;

%calculate the travel-time residual vector for this iteration
  rms=zeros(MAXITER,1);
  r=ttcal-ttobs;
  rms(iter,1)=norm(r)/sqrt(M);
  disp('updating model')

%GN, explicit regularization

  %apply pick standard deviation weighting here to travel time data ...
      and J
  %rows
  dr=-[sparse(ttcal-ttobs)./stdw ; sqrt(alphasq(piter))*(L*sparse(m))];
  for i=1:M
      J(i,:)=J(i,:)/stdw(i);
  end
  K=[J ; sqrt(alphasq(piter))*L];
  dm=K\dr;

%model update
  m=m+dm;
  slow=reshape(m,nz,nx);
  mnslow=mean(mean(slow));
  v=1./slow;

  %figure shows the separate model for each iteration as the code ...
      runs, for different regularization parameters (alpha).
%the final model in each case is assembled into figure 10.2
  figure(200+10*(piter-1)+iter)
  clf
  bookfonts

%interpolate the velocity field for plotting
  vi=interp2(xnm,znm,v,xnim,znim,'spline');
  imagesc(xv,zv,vi);
  colormap(flipud(jet));
  colorbar
```

```
  bookfonts
  xlabel('km');
  ylabel('km');
  set(gca,'color',[1 1 1]);
  alpha(vmask);
  drawnow;
  pause(0.1);

  disp('re-raytracing')
[tt,raypaths,it]=get_raypaths(M,xv,zv,v,raypaths_store,XFAC,CONV,NIT);
  disp('done re-raytracing')
%disp(['iterations: ',num2str(it)]);
raypaths_store=raypaths;
tts_store=tt;
  tttry=tts_store;
  rtry=ttobs-tttry;
  %dtry=reshape(rtry,M,1);
  %rmstry=sqrt(dtry'*dtry);
  rmstry=norm(rtry)/sqrt(M);
  disp('alpha, iteration, rmsnew, sqrt(chi^2)')
  [sqrt(alphasq(piter)) iter rmstry NOISE*sqrt(N)]
  misfit(piter,iter)=rmstry;
  mnorm(piter,iter)=norm(L*m);

%title for evolving velocity model plot
 title(['\alpha = ',num2str(sqrt(alphasq(piter))),' iteration ...
     ',num2str(iter),' rms ',num2str(rmstry)]);

%rms difference wrt true model
  %mrms(piter,iter)= norm((mtrue-m));

%  end of tomography inversion loop
end

vstore(piter,:,:)=vi;

% end of regularization parameter loop
% use this smooth model for a subsequent less-well regularized ...
    inversion
end

%show results for the various regularization parameters

%this figure (not used in text) shows the residual stats for each ...
    iteration and alpha value
figure(3)
bookfonts
plot(1:iter,misfit)
xlabel('Iteration')
ylabel('Residual Norm, ||G(m)-d||_2')
```

```
%this figure (not used in text) shows the seminorm stats for each ...
    iteration and alpha value
figure(4)
bookfonts
semilogy(1:iter,mnorm)
xlabel('Iteration')
ylabel('Solution Seminorm, ||Lm||_2')

%L-curve
figure(5)
bookfonts;
loglog(misfit(1:piter,MAXITER),mnorm(1:piter,MAXITER),'ok-')
xlabel('Residual Norm, ||G(m)-d||_2')
ylabel('Solution Seminorm, ||Lm||_2')
axis tight
hold on
loglog([NOISE*sqrt(N),NOISE*sqrt(N)],[.00001,.001],'k--')
for i=1:2:piter
text(misfit(i,MAXITER),mnorm(i,MAXITER),['   ...
    ',num2str(sqrt(alphasq(i)))]);
end
text(NOISE*sqrt(N),.000015,'   \Delta')
hold off

%Models compared to true model
figure(6)
bookfonts;
semilogx(sqrt(alphasq),mrms(1:piter,MAXITER),'ok-')
xlabel('\alpha')
ylabel('||m_{true}-m||_2')
ylim([0 2.2e-4])

%Suite of models
figure(70)
for i=1:piter
subplot(4,4,i)
vtmp1=vstore(i,:,:);
vtmp(:,:)=vtmp1;
imagesc(vtmp)
colormap(flipud(jet));
axis square
set(gca,'xticklabel','')
set(gca,'yticklabel','')
title(['\alpha = ',num2str(sqrt(alphasq(i)))])
end
```

APPENDIX F

TOMOGRAPHY IMAGES

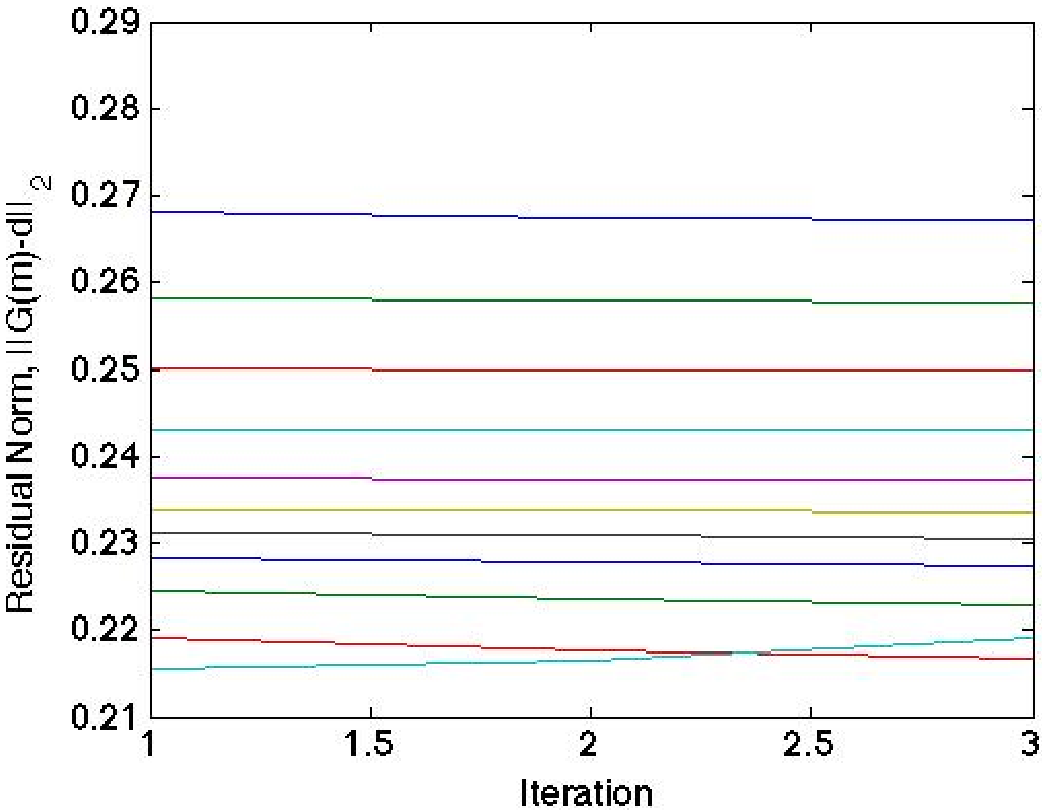

Figure F.1: Residual Norm versus number of Iterations

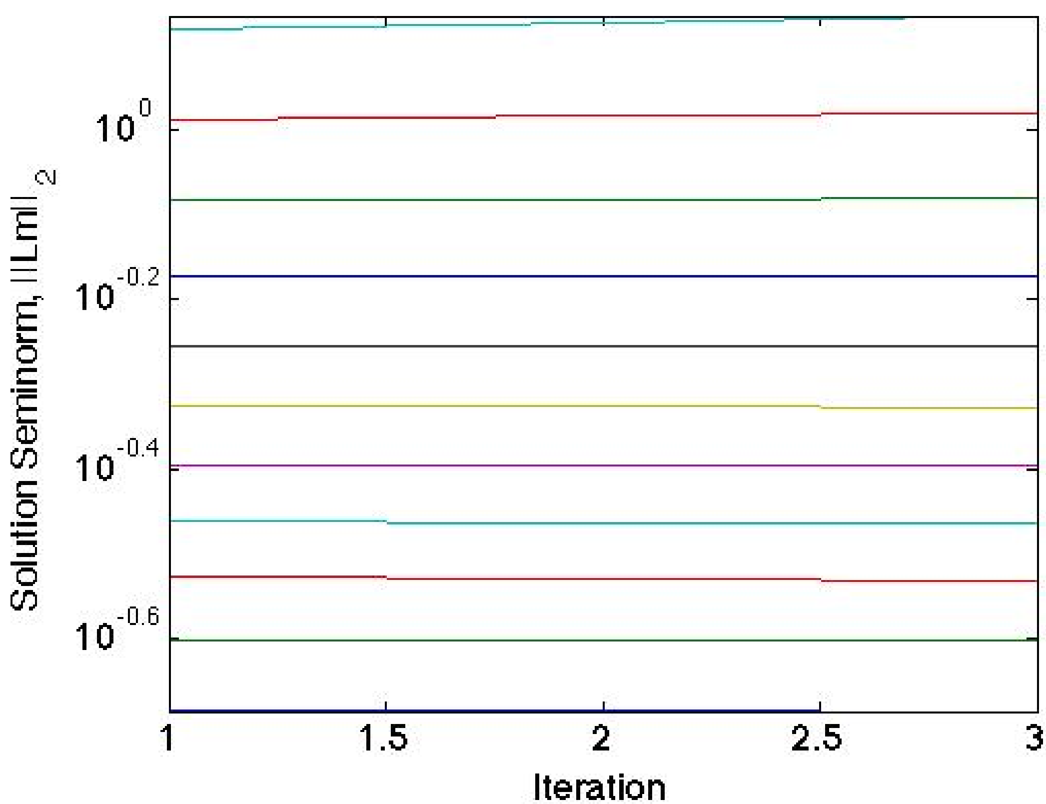

Figure F.2: Solution Seminorm versus number of Iterations

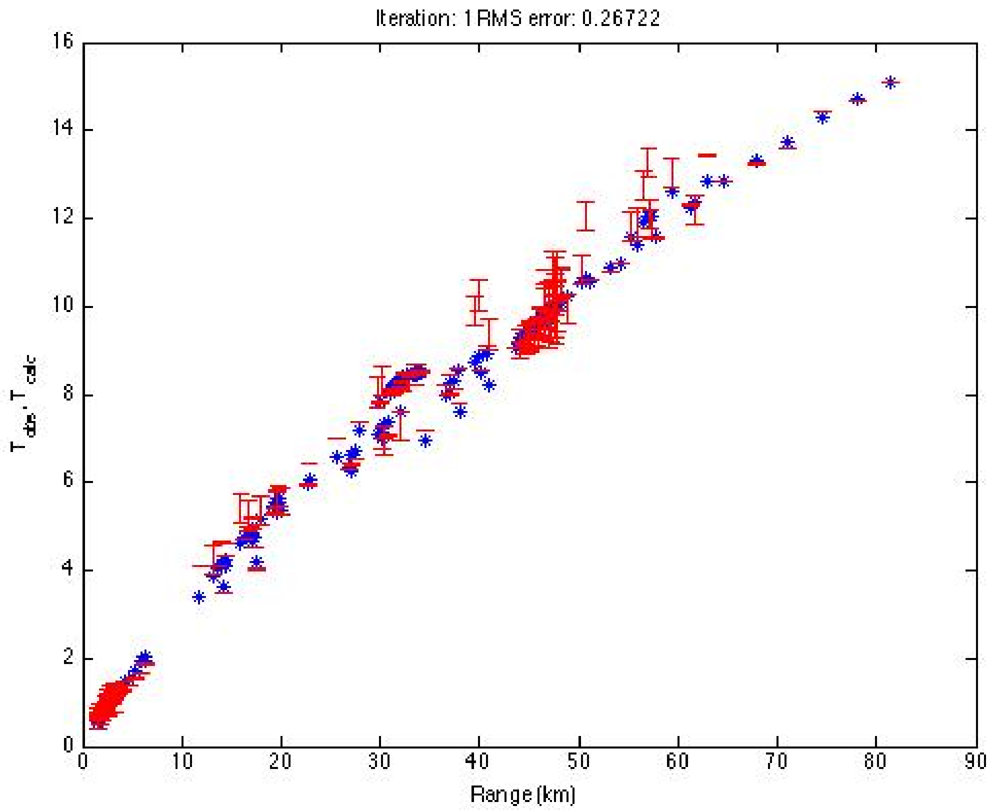

Figure F.3: RMS Error for α = 1634.9197, First Iteration

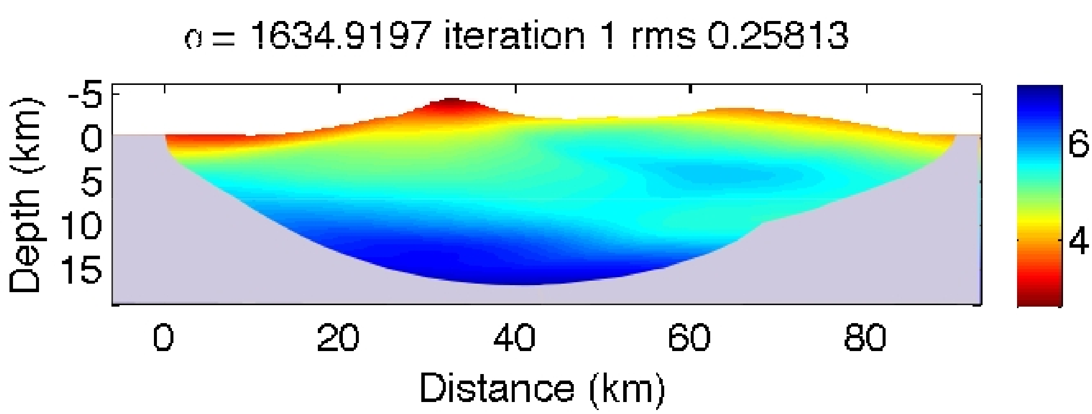

Figure F.4: Velocity model for α = 1634.9197, First Iteration

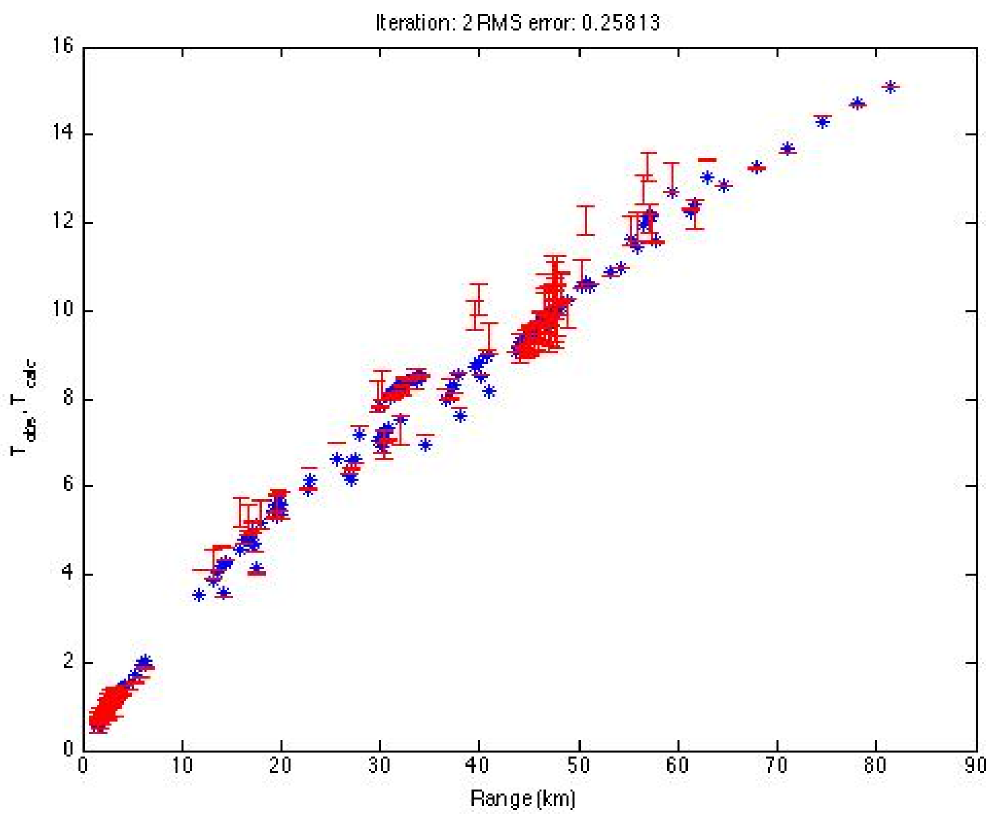

Figure F.5: RMS Error for α = 1634.9197, Second Iteration

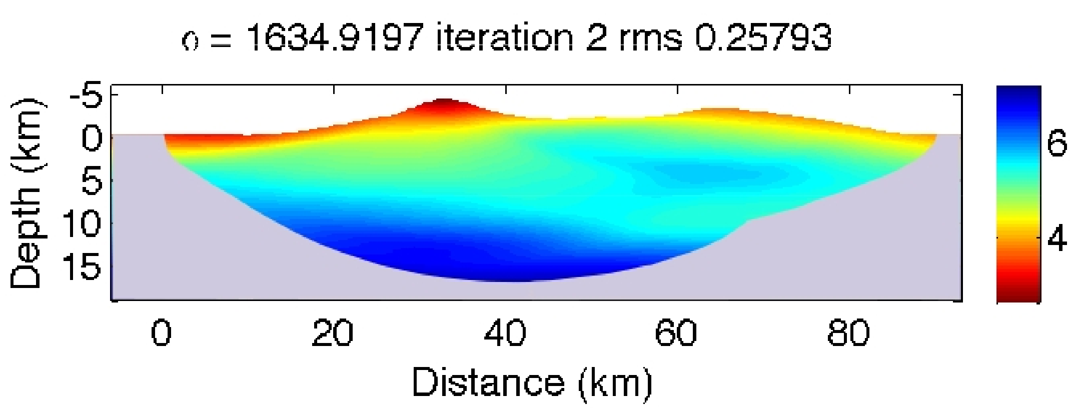

Figure F.6: Velocity model for α = 1634.9197, Second Iteration

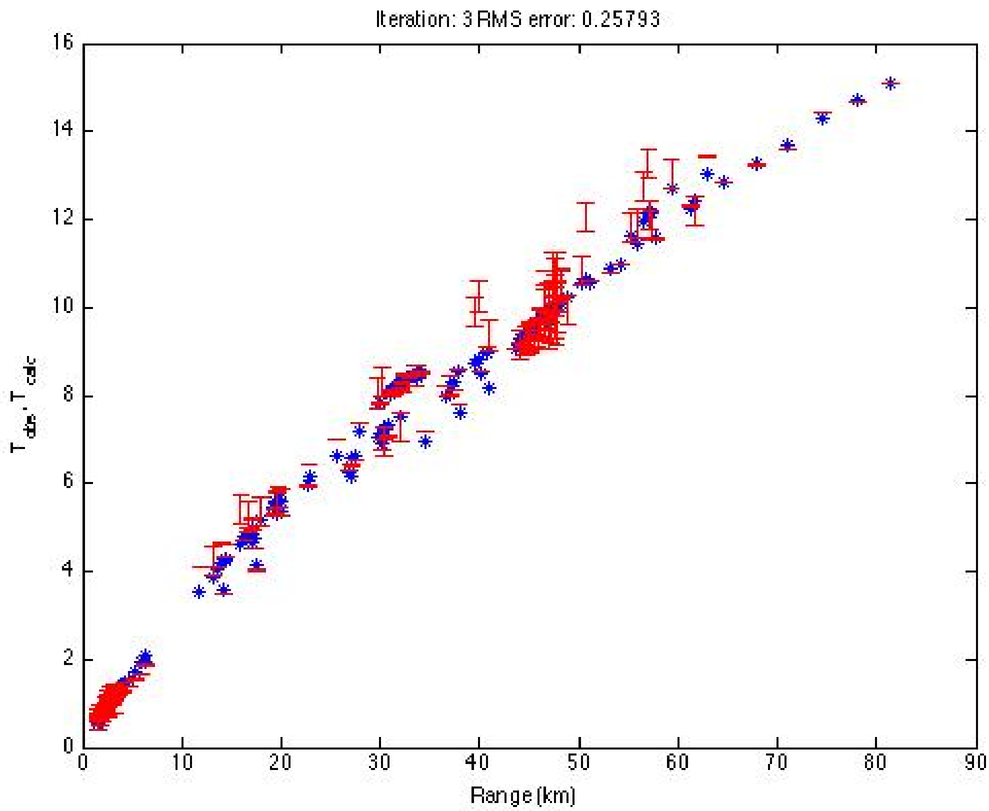

Figure F.7: RMS Error for α = 1634.9197, Third Iteration

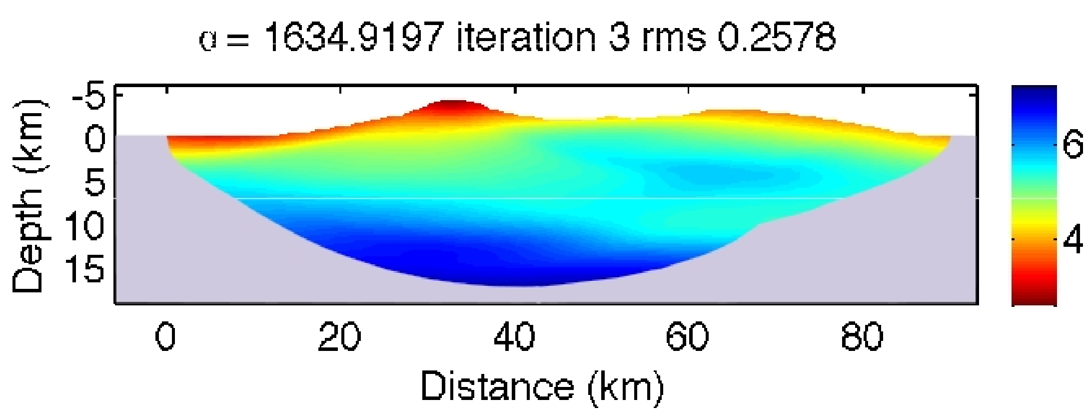

Figure F.8: Velocity model for α = 1634.9197, Third Iteration

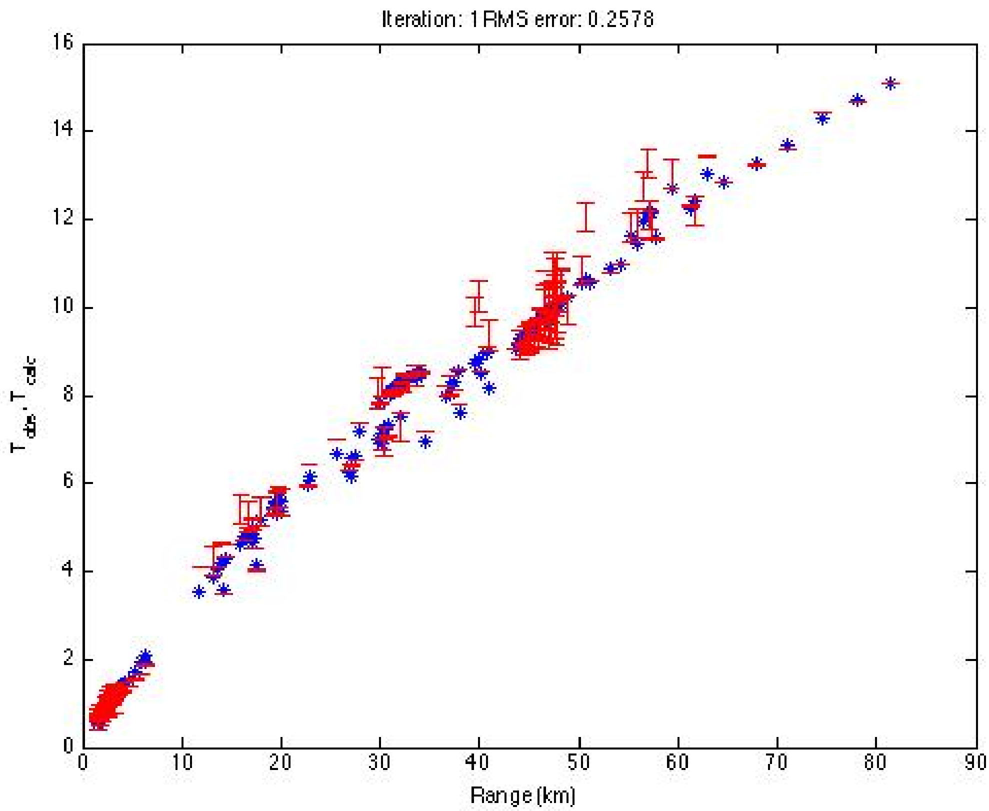

Figure F.9: RMS Error for α = 1160.6255, First Iteration

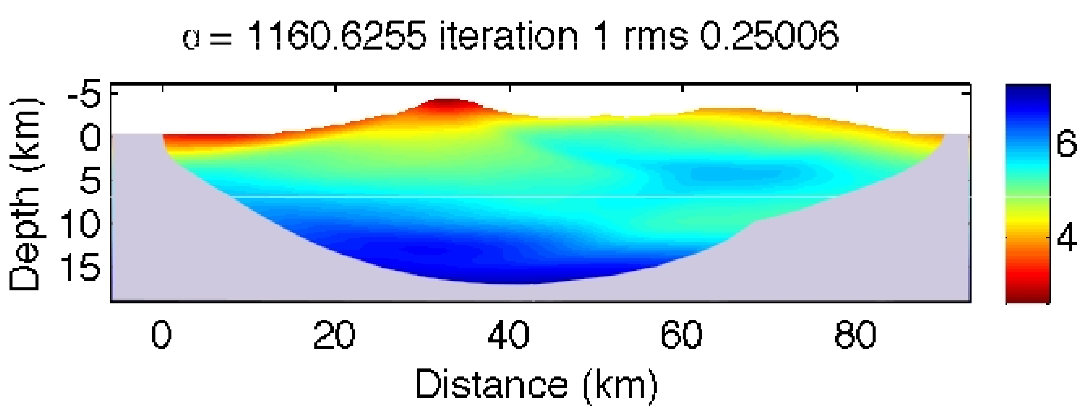

Figure F.10: Velocity model for α = 1160.6255, First Iteration

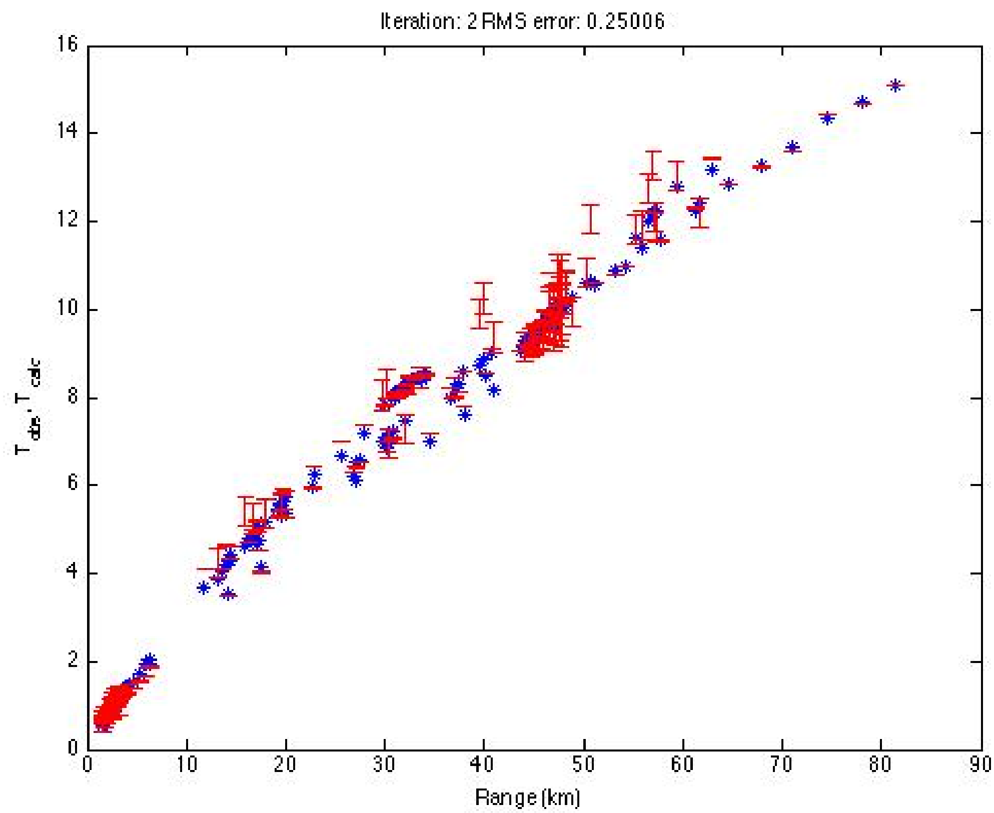

Figure F.11: RMS Error for α = 1160.6255, Second Iteration

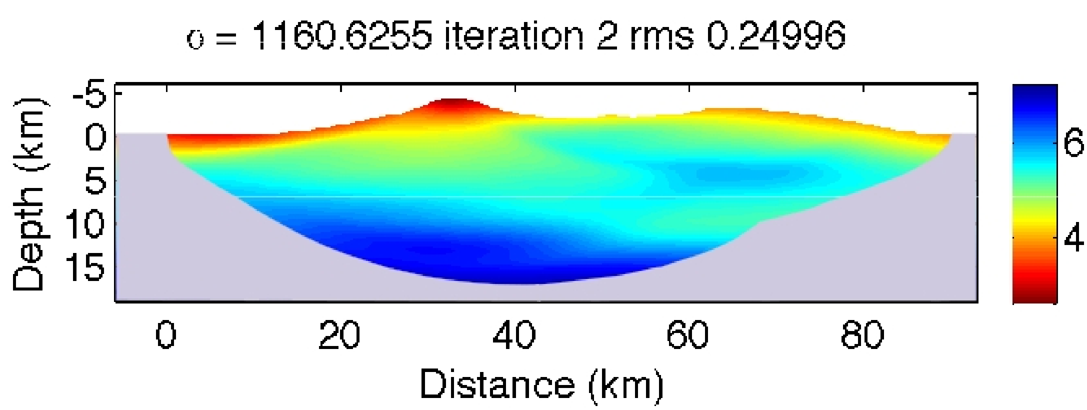

Figure F.12: Velocity model for α = 1160.6255, Second Iteration

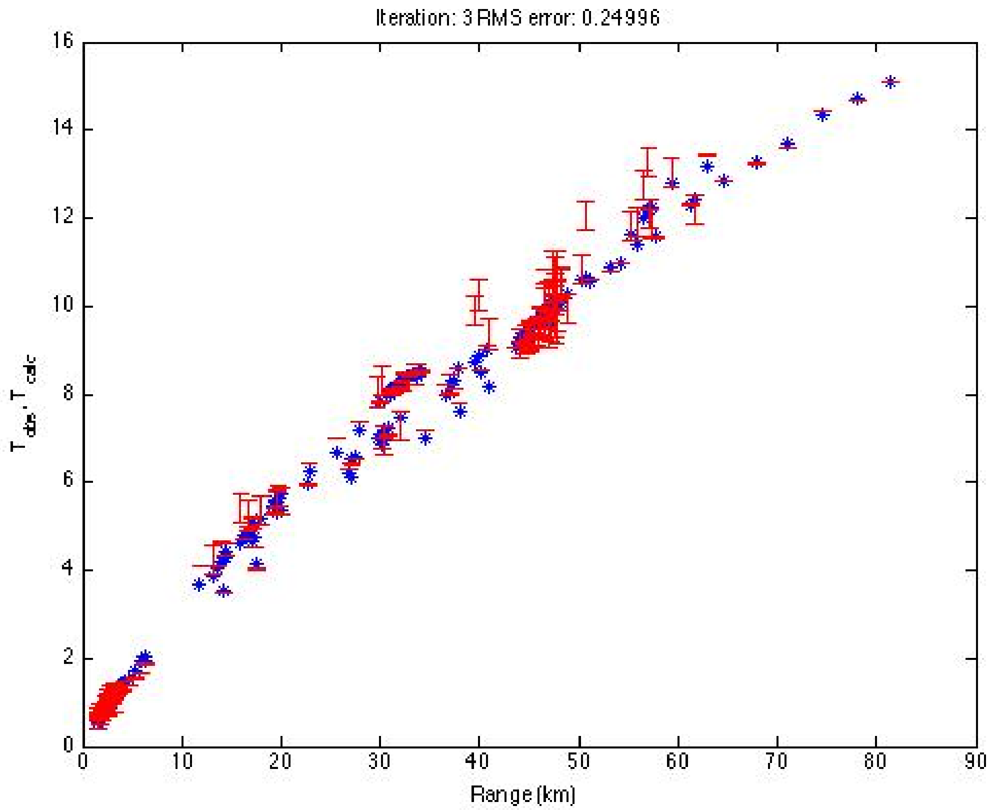

Figure F.13: RMS Error for α = 1160.6255, Third Iteration

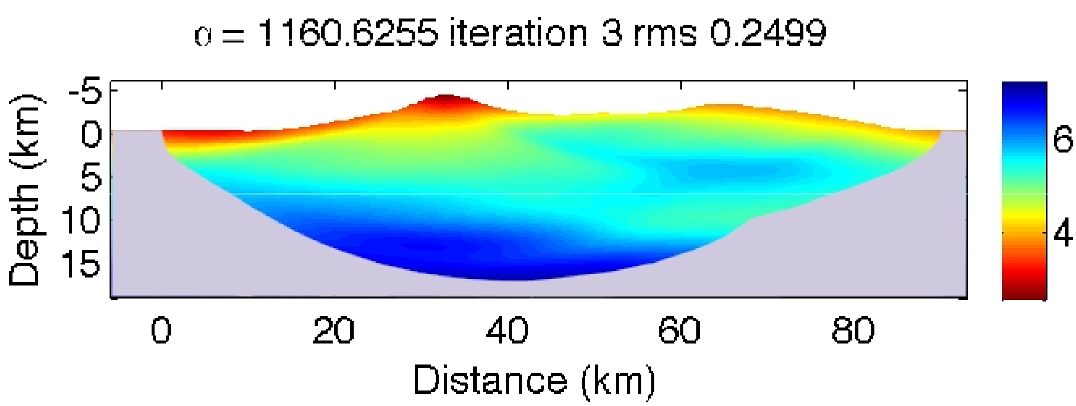

Figure F.14: Velocity model for α = 1160.6255, Third Iteration

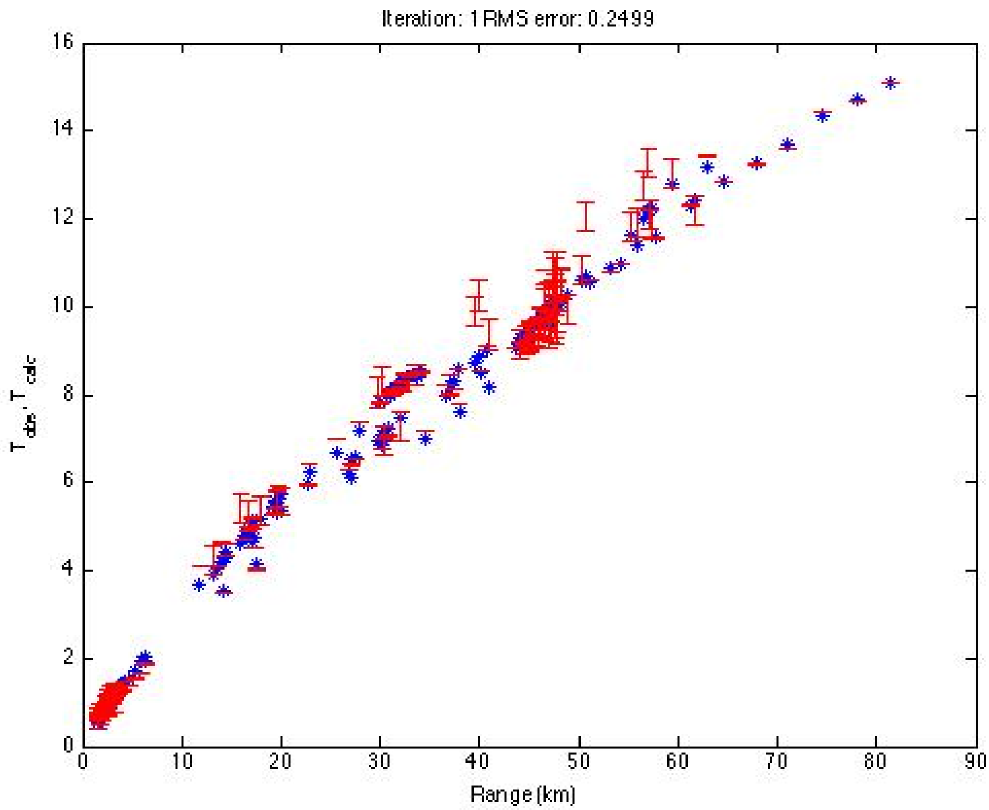

Figure F.15: RMS Error for α = 824.562, First Iteration

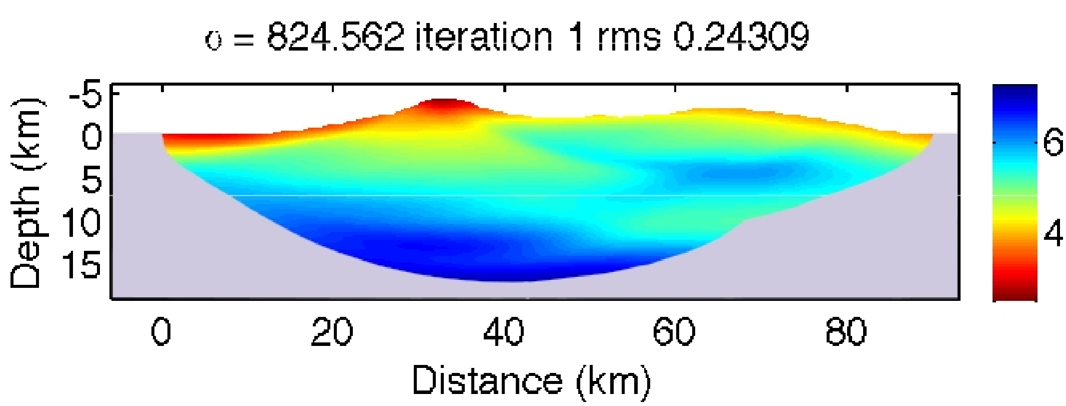

Figure F.16: Velocity model for α = 824.562, First Iteration

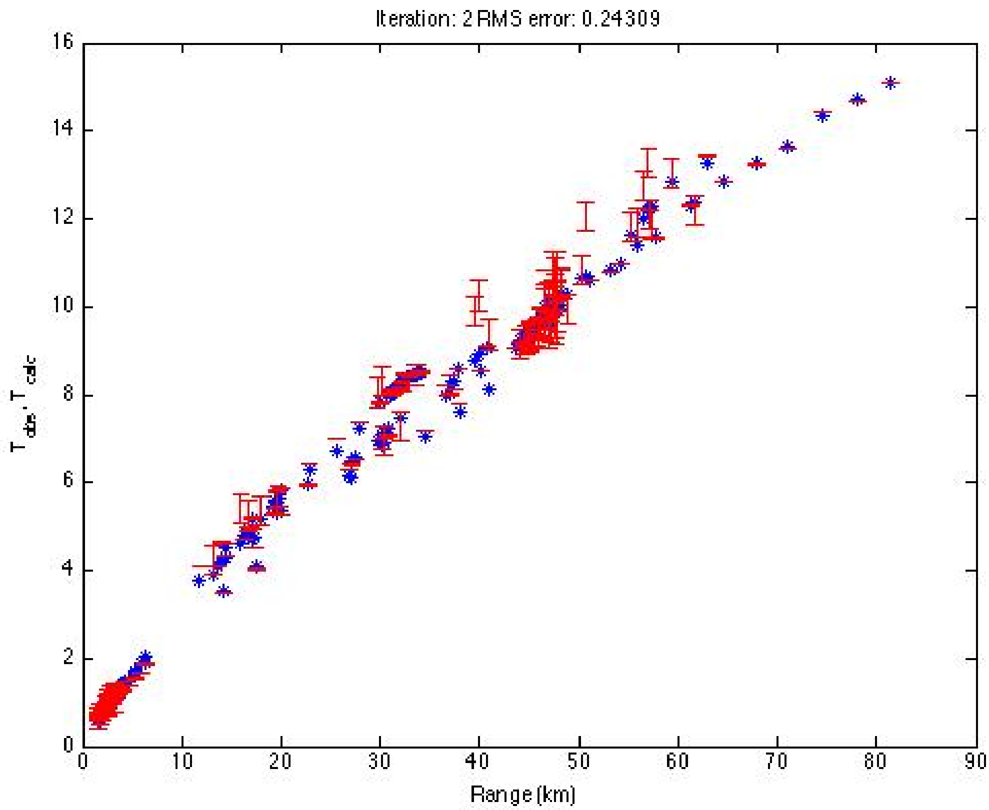

Figure F.17: RMS Error for α = 824.562, Second Iteration

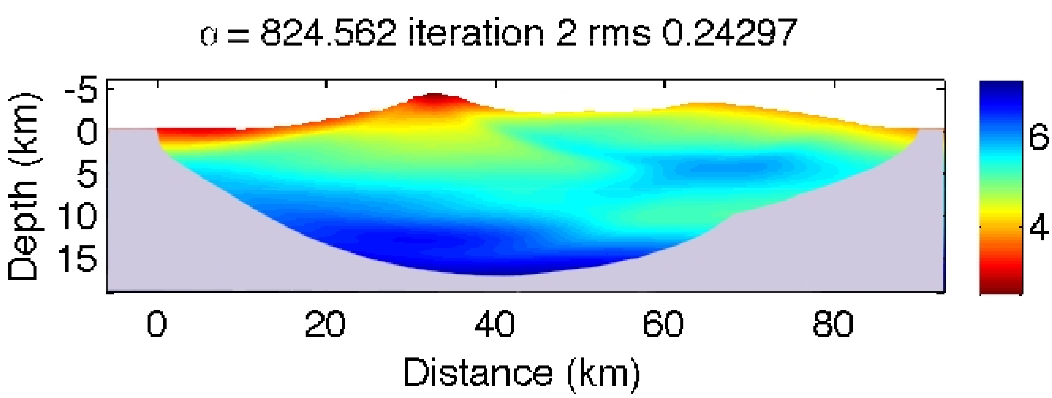

Figure F.18: Velocity model for α = 824.562, Second Iteration

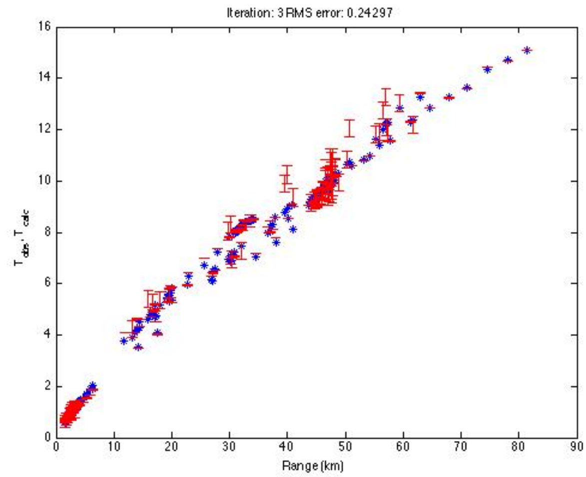

Figure F.19: RMS Error for α = 824.562, Third Iteration

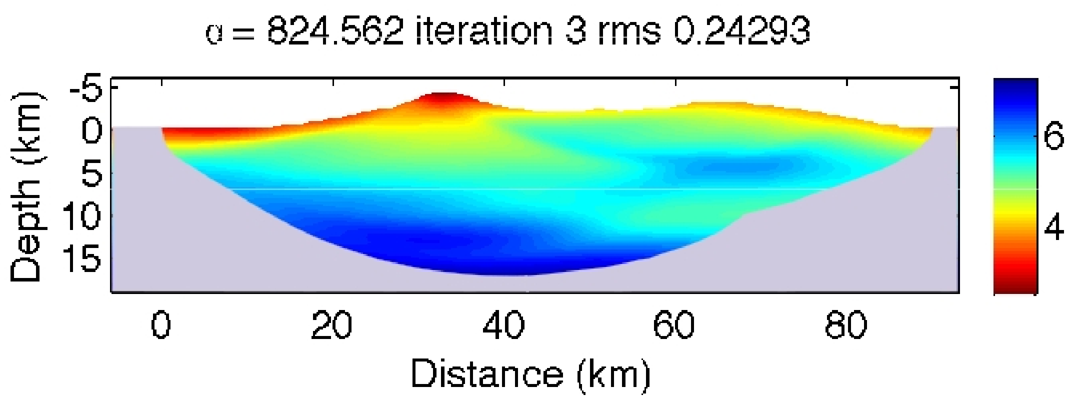

Figure F.20: Velocity model for α = 824.562, Third Iteration

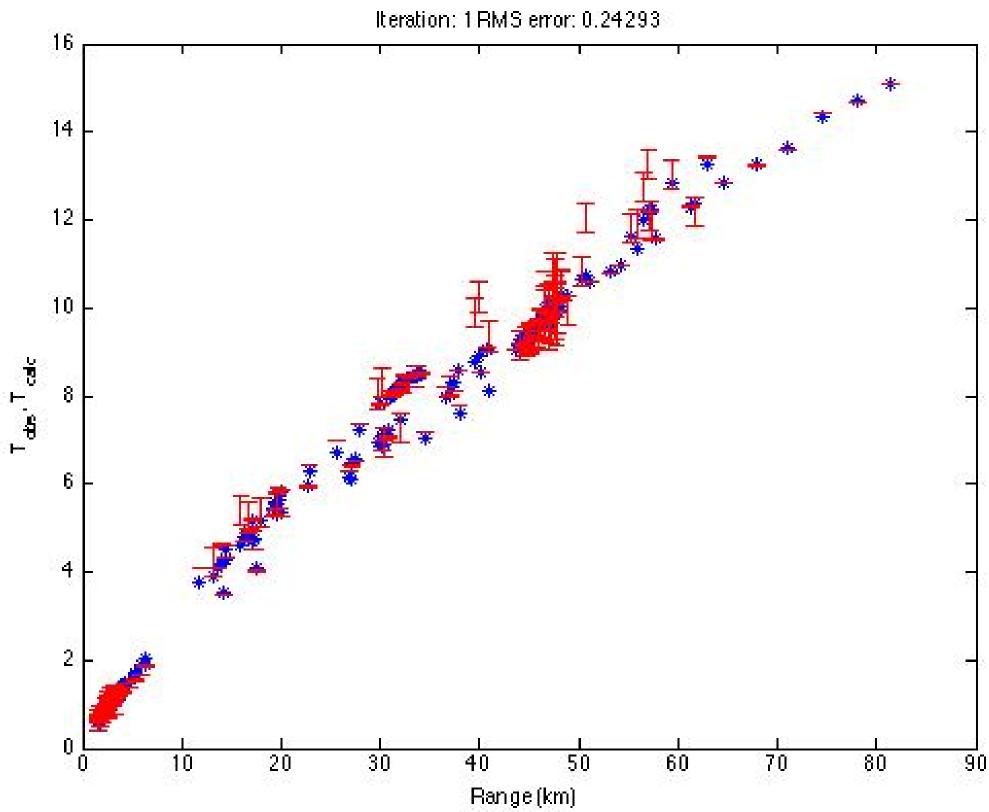

Figure F.21: RMS Error for α = 586.5514, First Iteration

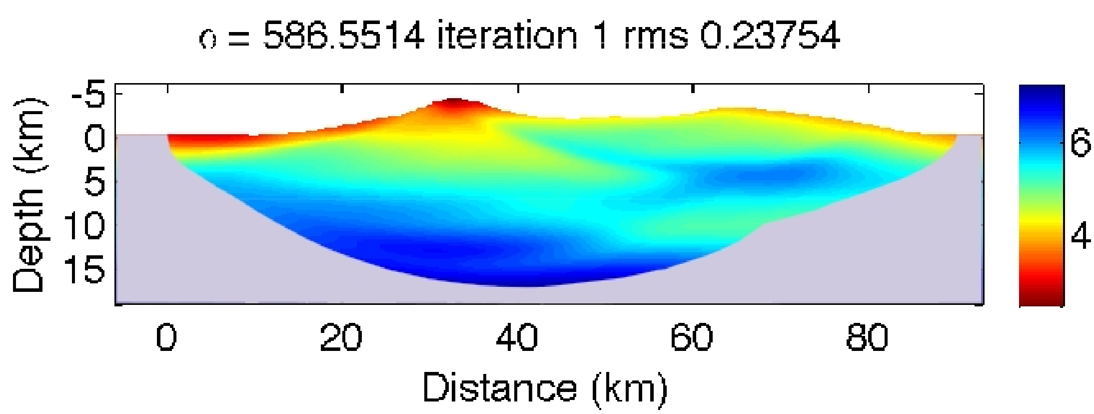

Figure F.22: Velocity model for α = 586.5514, First Iteration

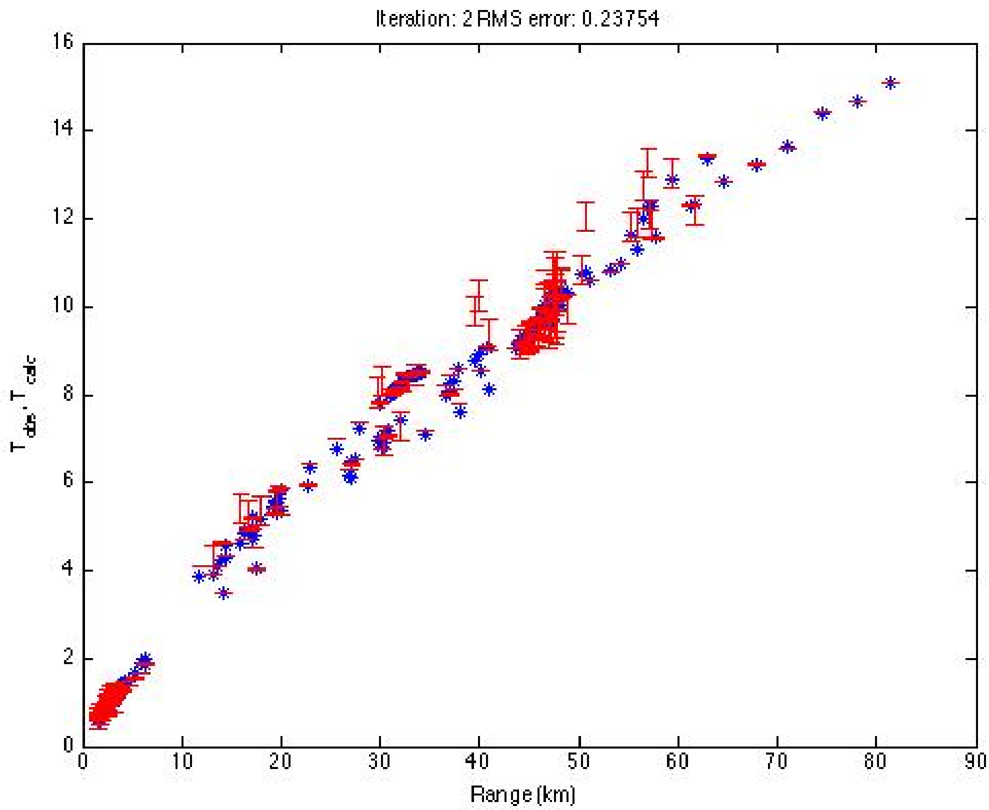

Figure F.23: RMS Error for α = 586.5514, Second Iteration

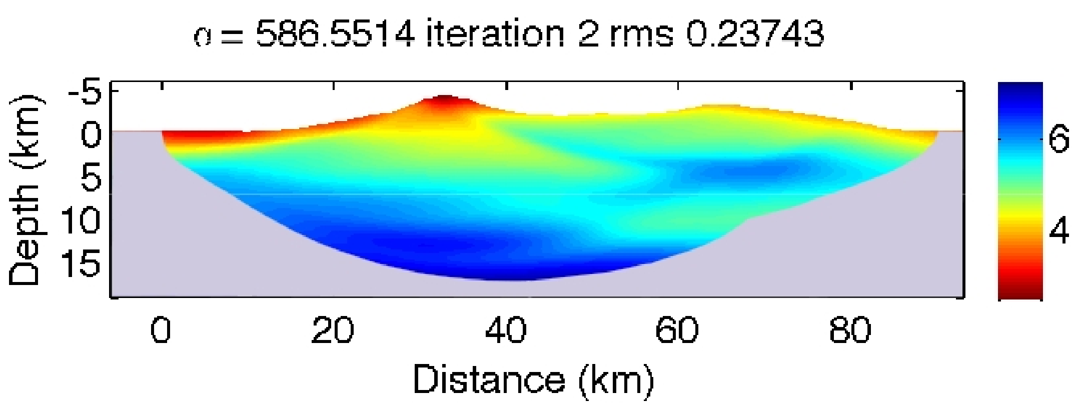

Figure F.24: Velocity model for α = 586.5514, Second Iteration

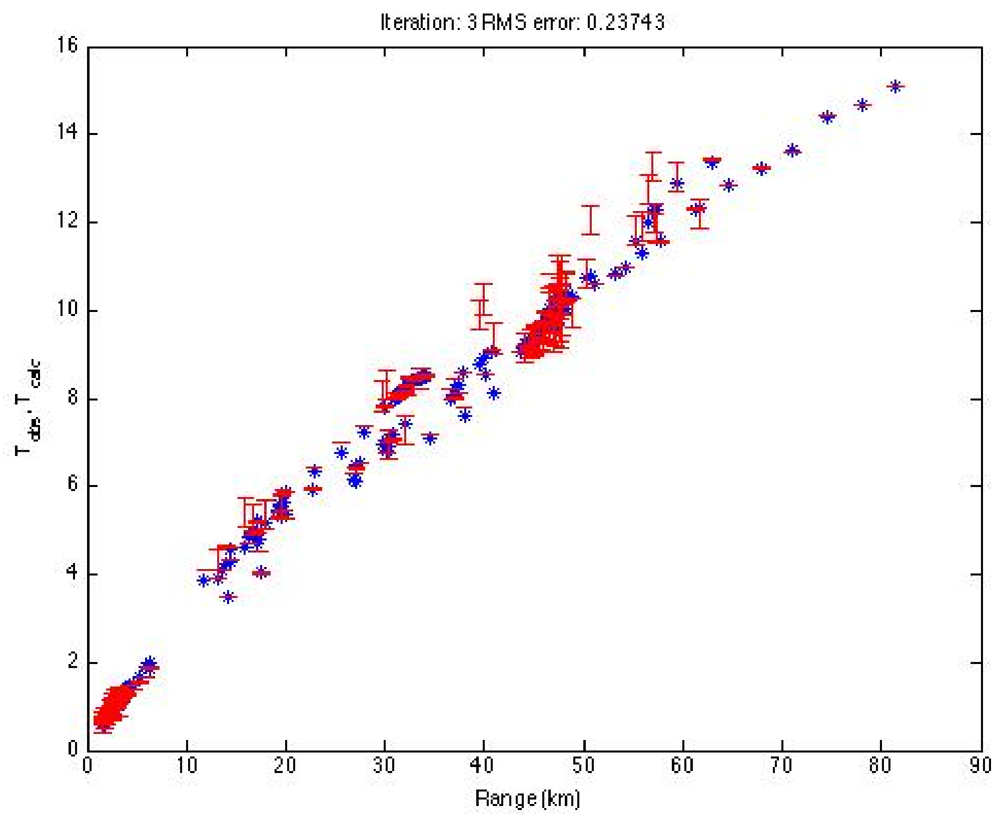

Figure F.25: RMS Error for α = 586.5514, Third Iteration

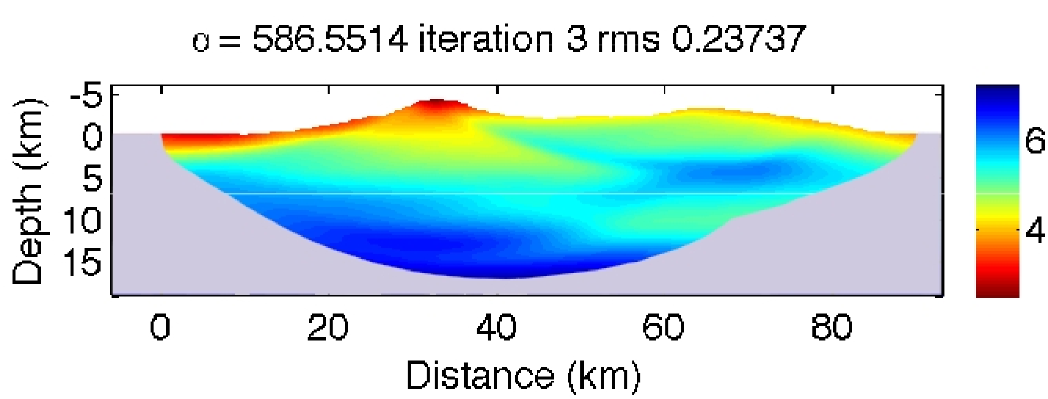

Figure F.26: Velocity model for α = 586.5514, Third Iteration

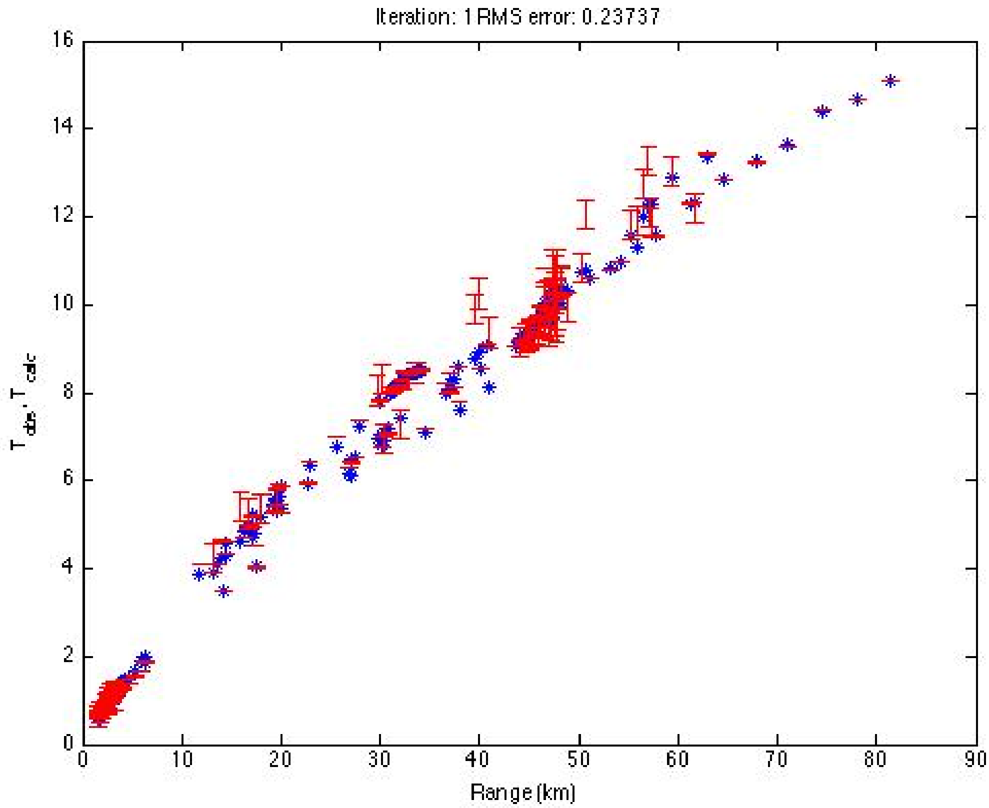

Figure F.27: RMS Error for α = 417.8337, First Iteration

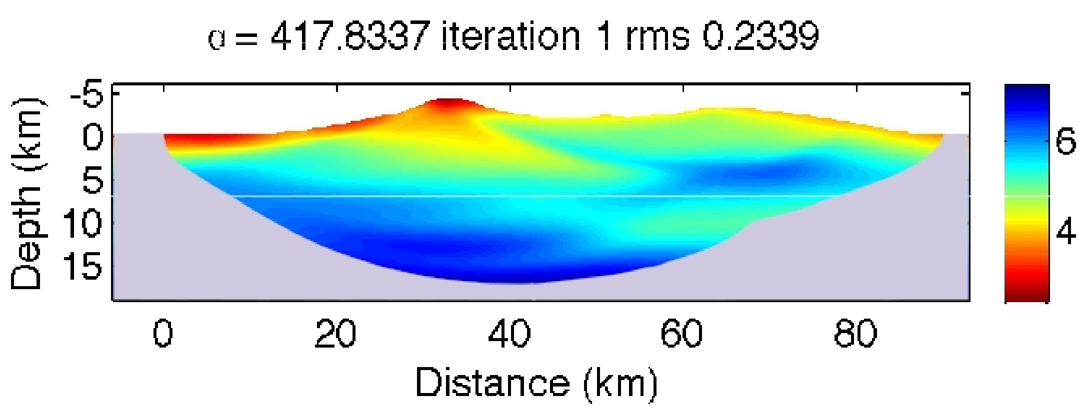

Figure F.28: Velocity model for α = 417.8337, First Iteration

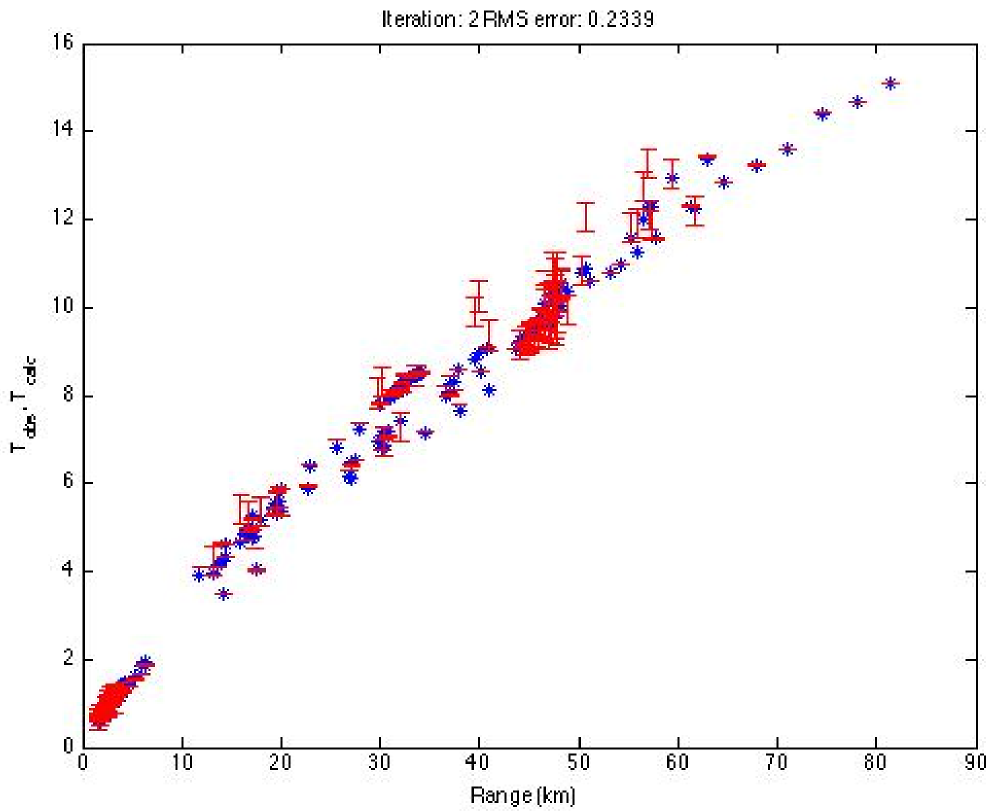

Figure F.29: RMS Error for α = 417.8337, Second Iteration

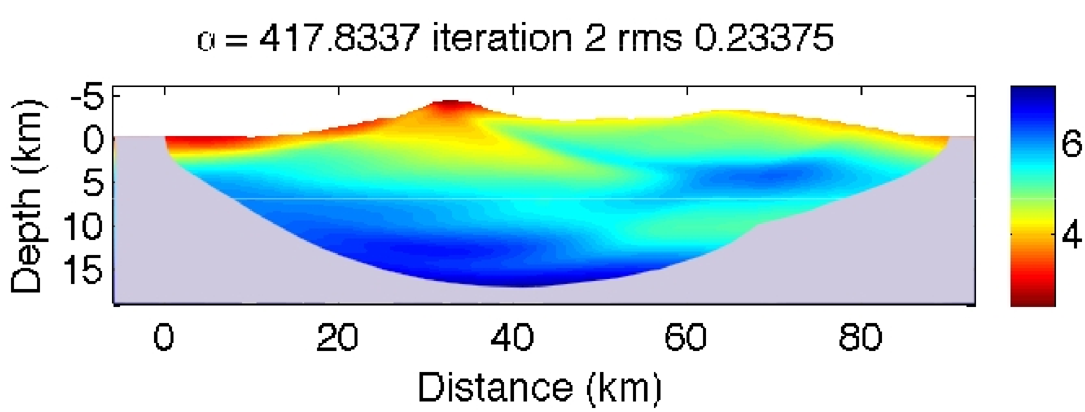

Figure F.30: Velocity model for α = 417.8337, Second Iteration

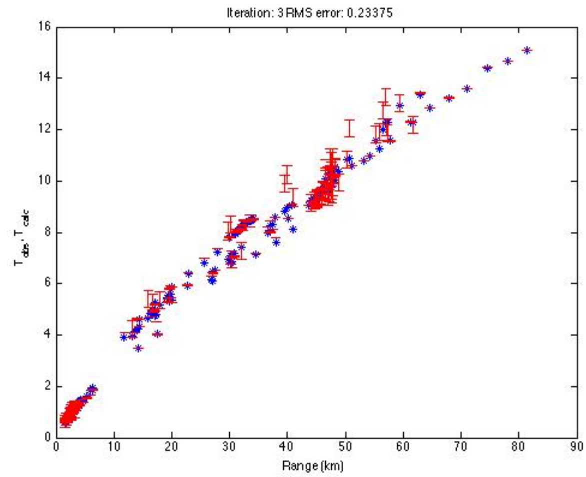

Figure F.31: RMS Error for α = 417.8337, Third Iteration

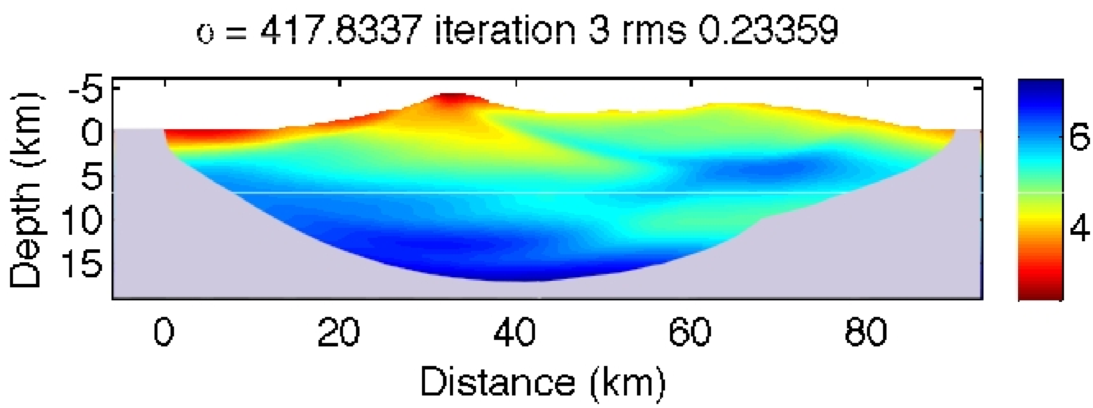

Figure F.32: Velocity model for α = 417.8337, Third Iteration

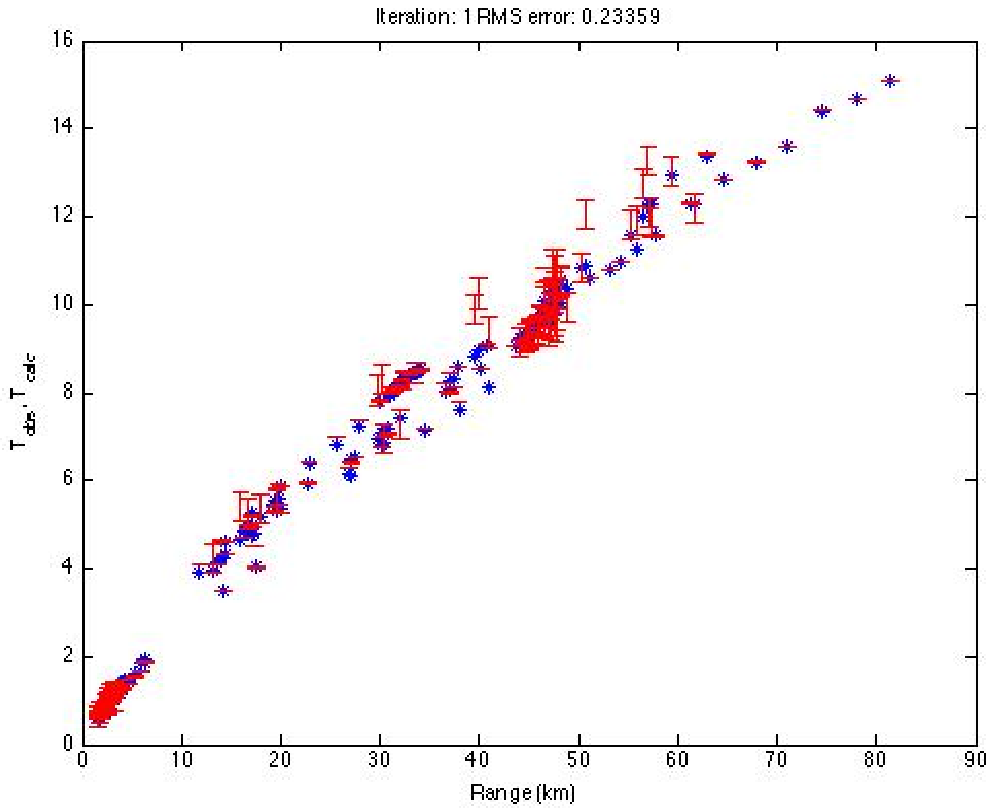

Figure F.33: RMS Error for α = 297.9803, First Iteration

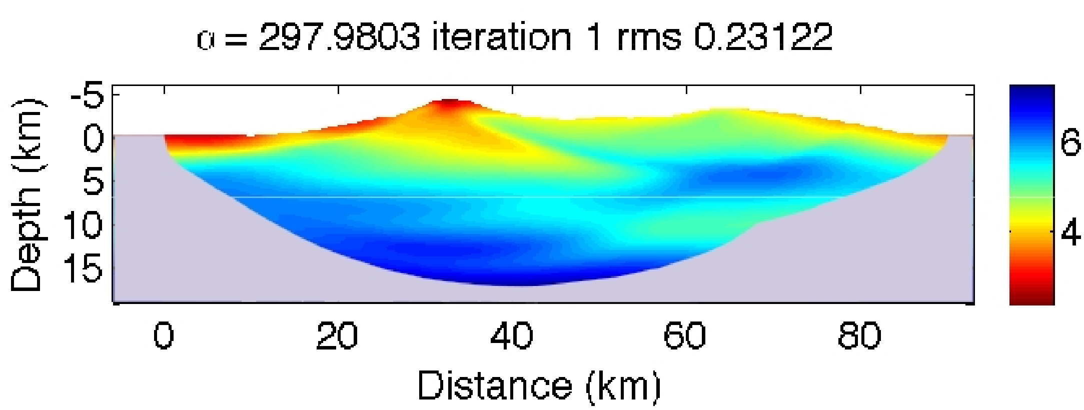

Figure F.34: Velocity model for α = 297.9803, First Iteration

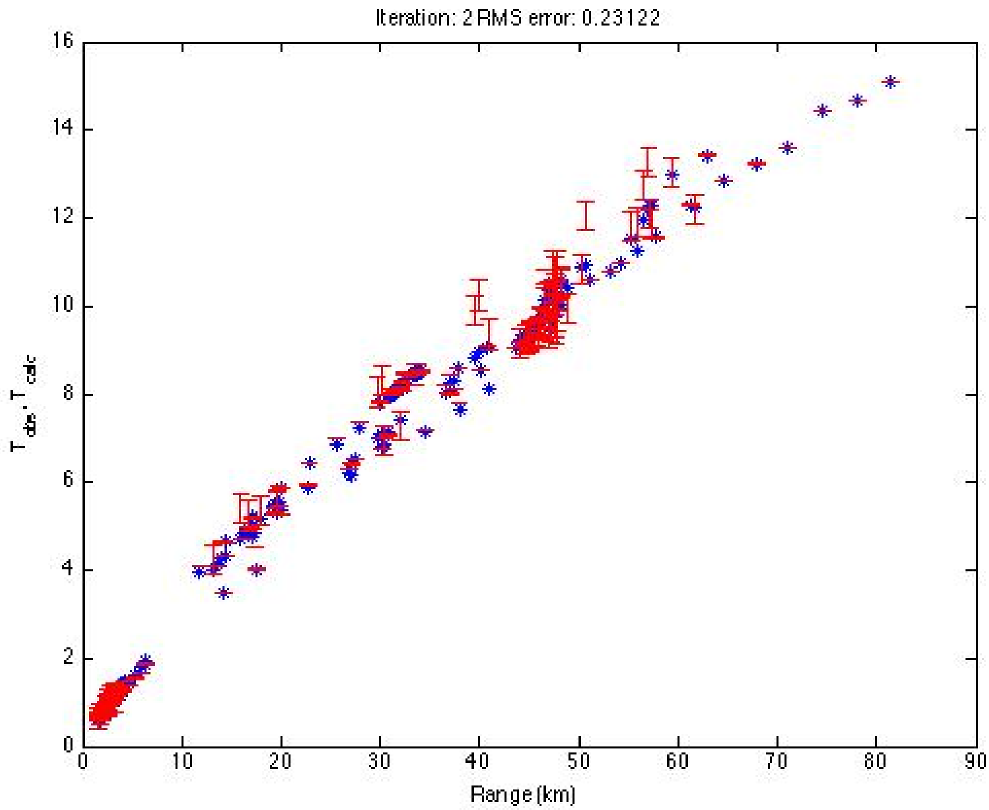

Figure F.35: RMS Error for α = 297.9803, Second Iteration

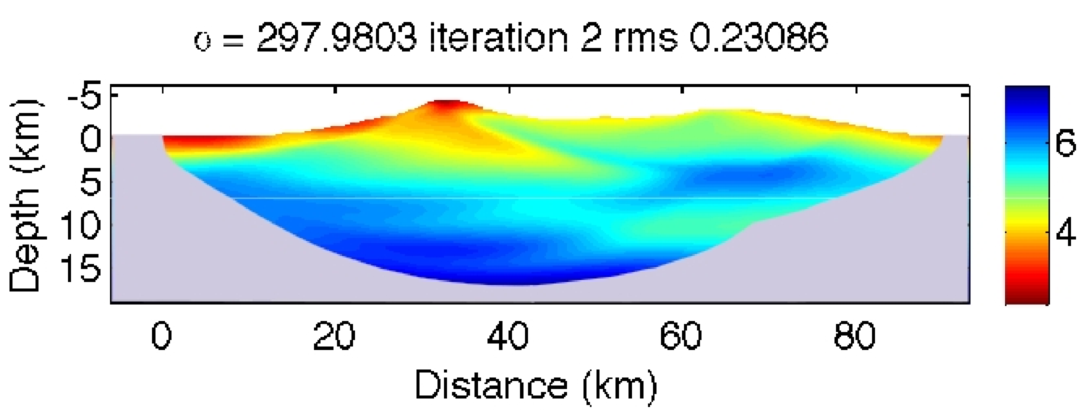

Figure F.36: Velocity model for α = 297.9803, Second Iteration

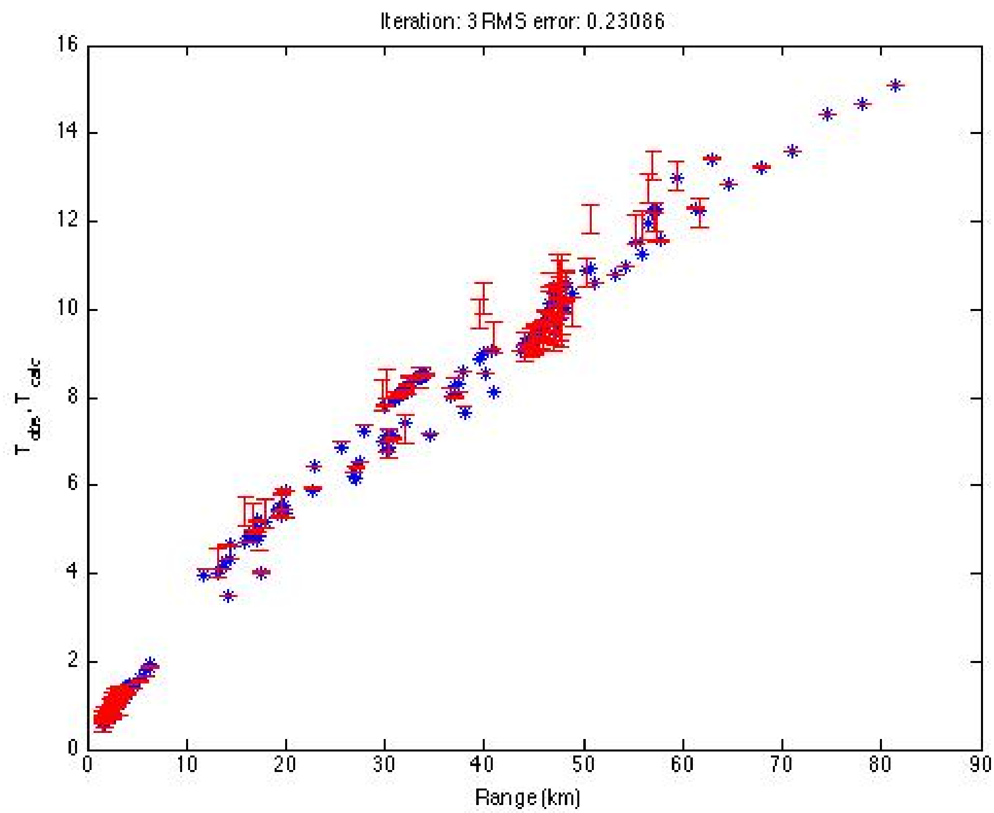

Figure F.37: RMS Error for α = 297.9803, Third Iteration

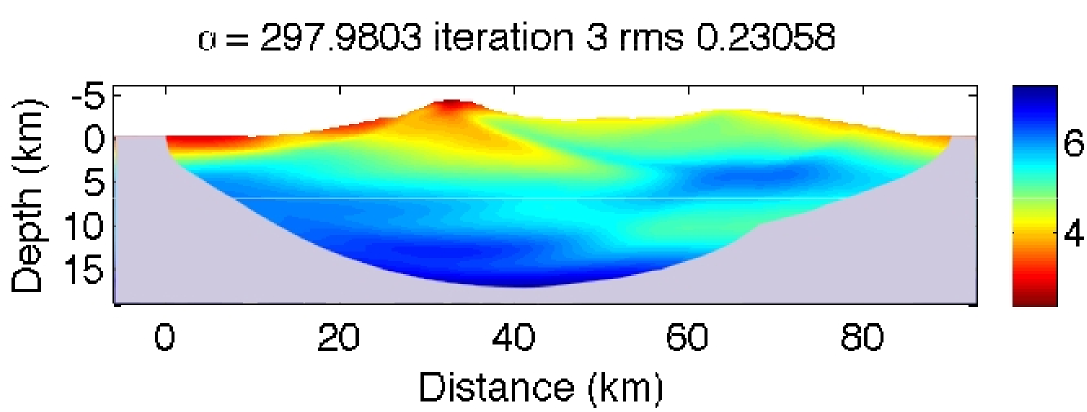

Figure F.38: Velocity model for α = 297.9803, Third Iteration

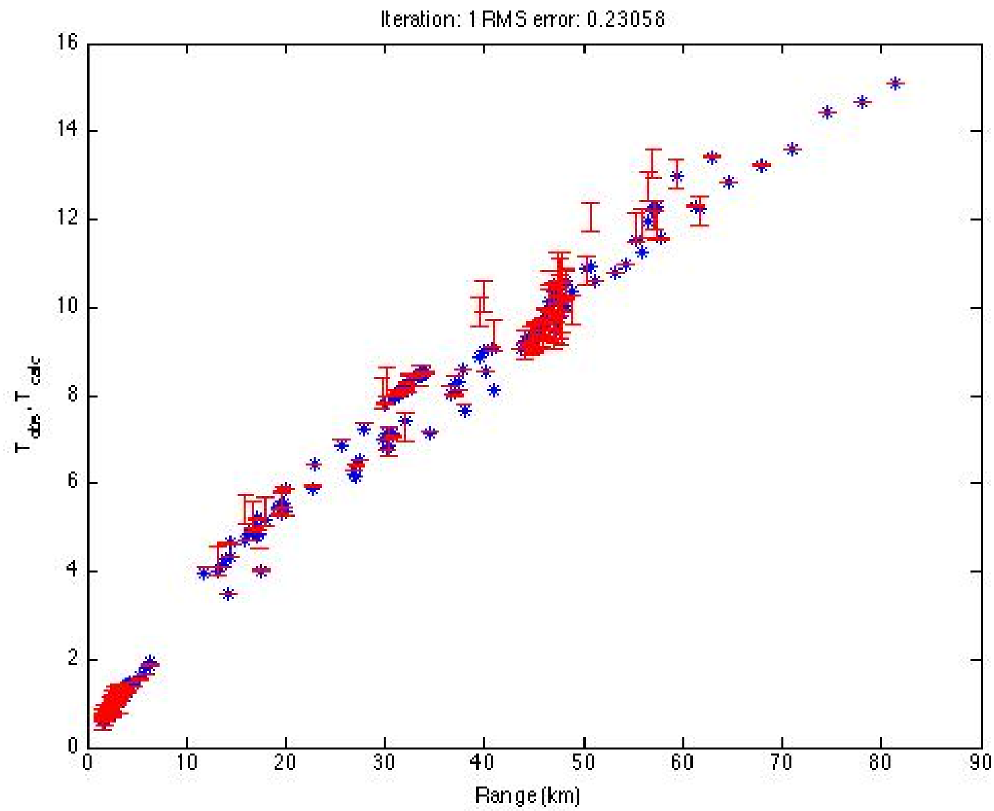

Figure F.39: RMS Error for α = 212.5295, First Iteration

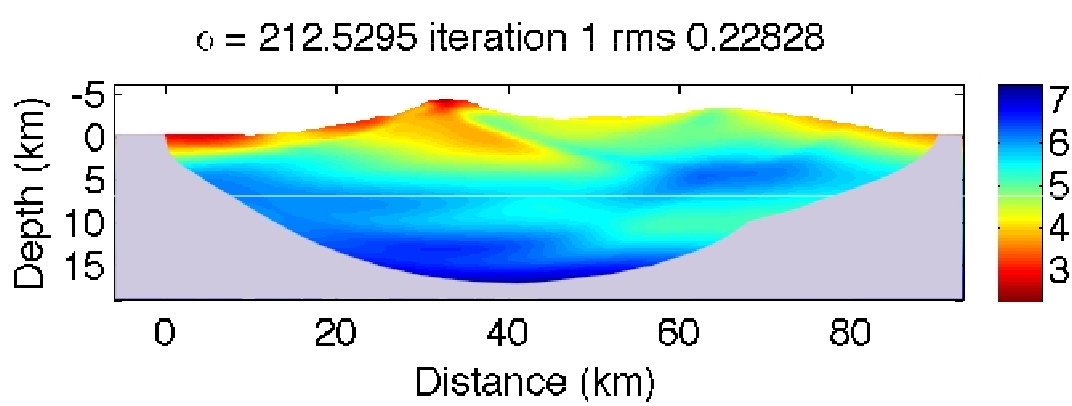

Figure F.40: Velocity model for α = 212.5295, First Iteration

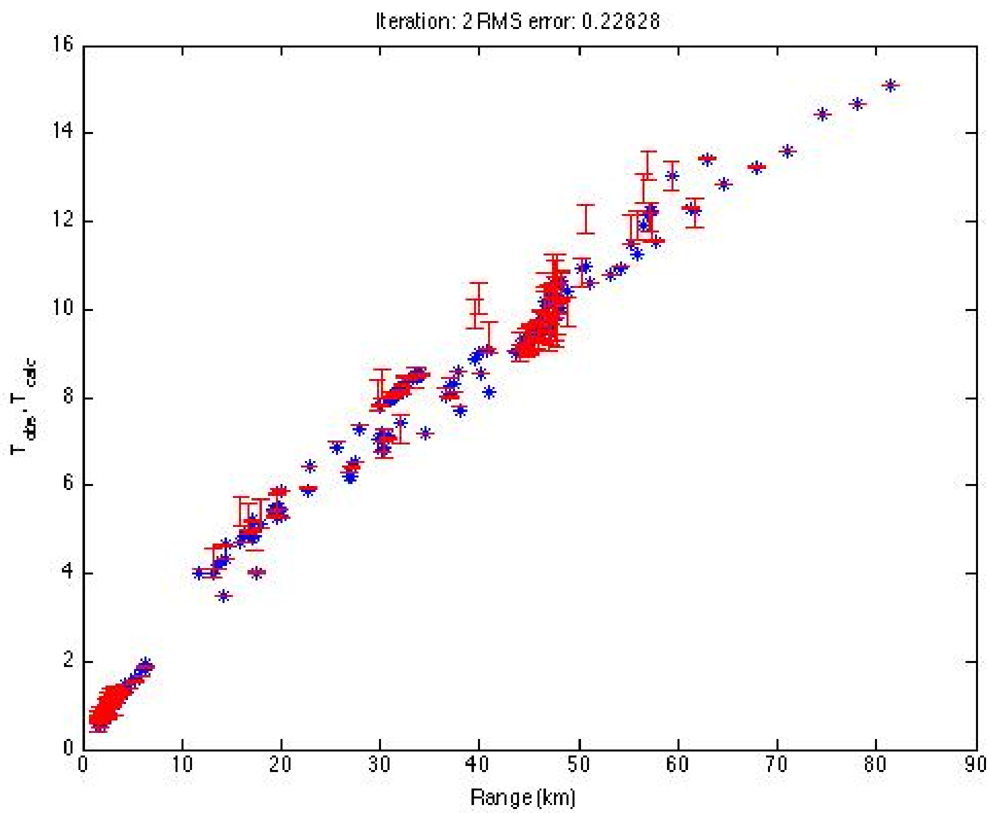

Figure F.41: RMS Error for α = 212.5295, Second Iteration

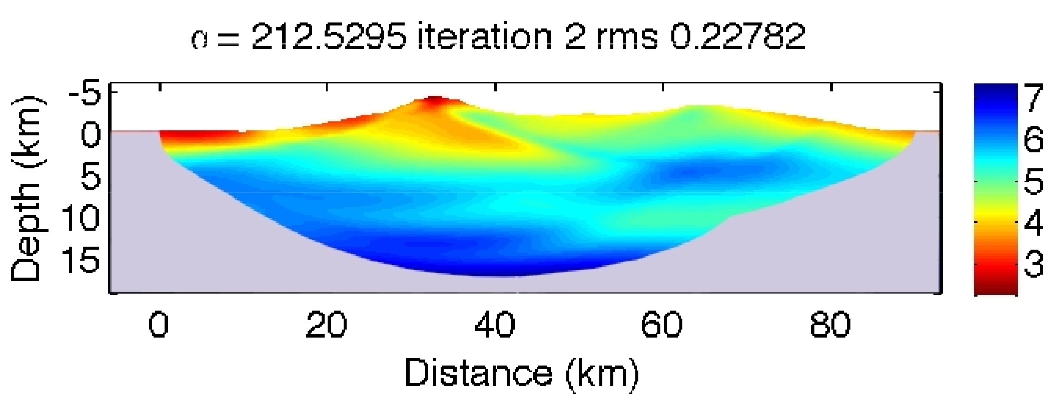

Figure F.42: Velocity model for α = 212.5295, Second Iteration

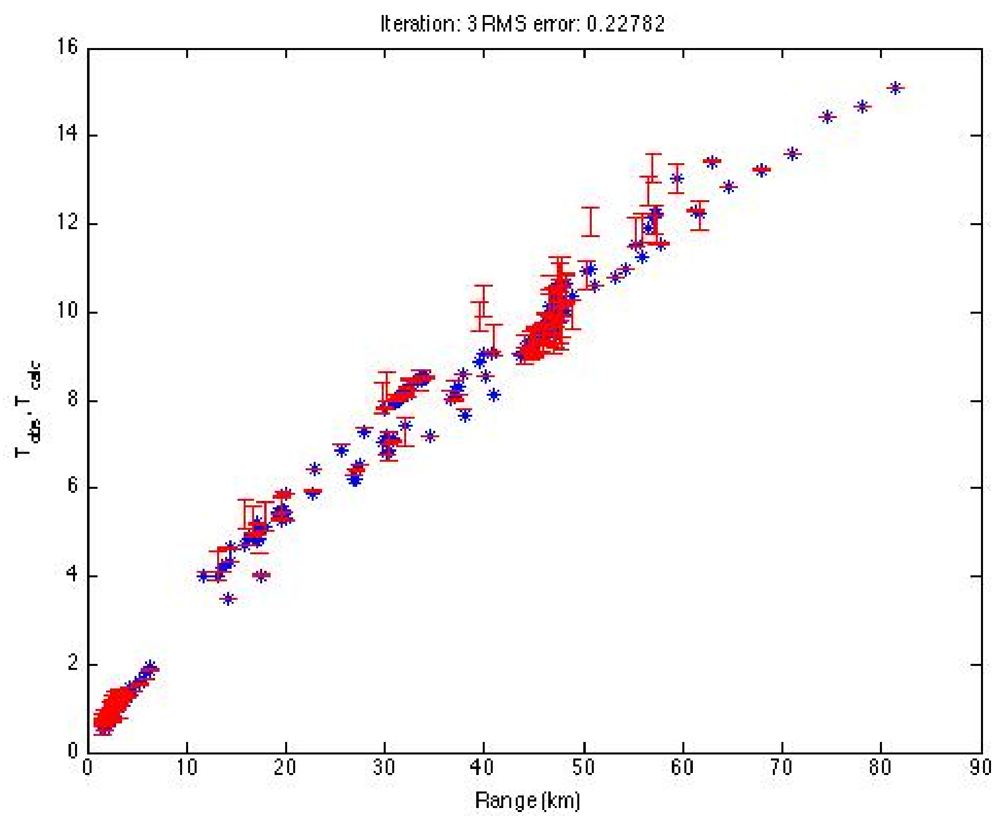

Figure F.43: RMS Error for α = 212.5295, Third Iteration

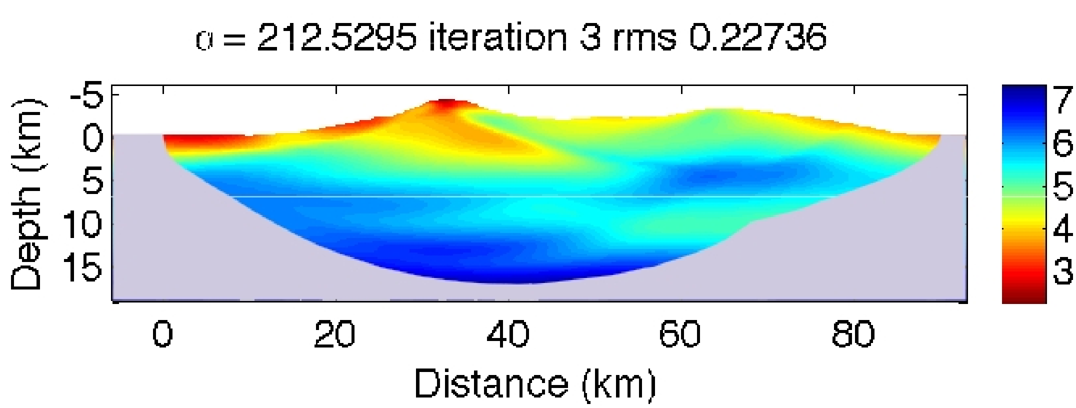

Figure F.44: Velocity model for α = 212.5295, Third Iteration

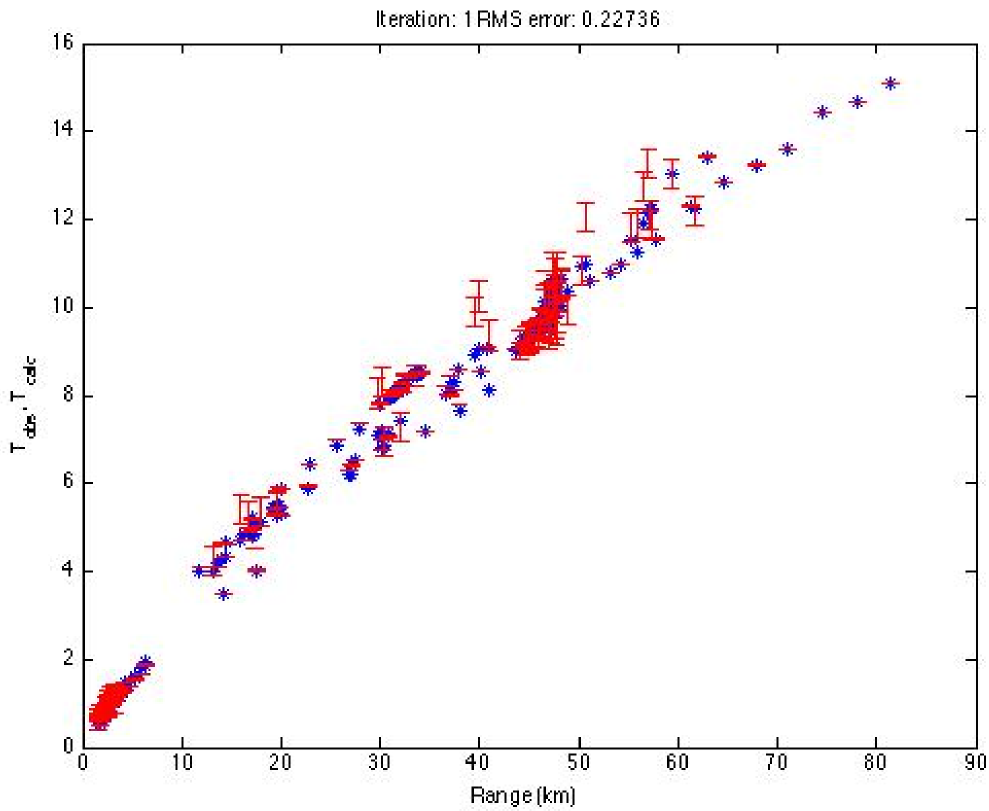

Figure F.45: RMS Error for α = 151.4196, First Iteration

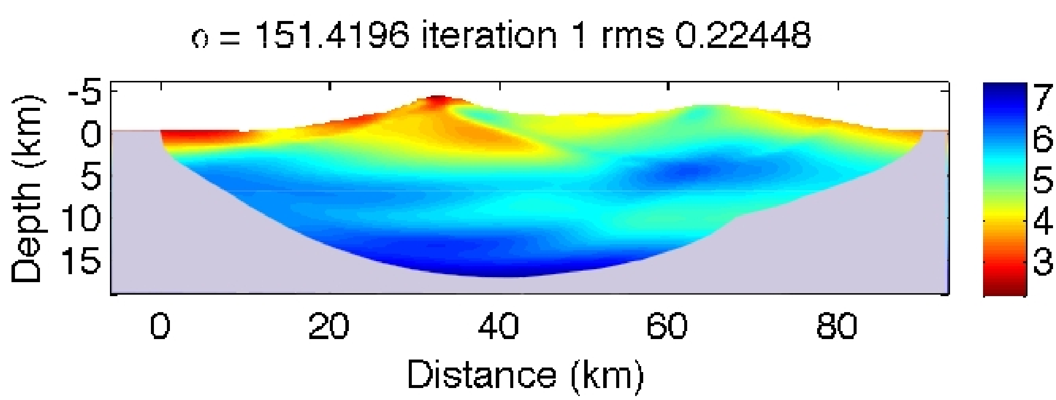

Figure F.46: Velocity model for α = 151.4196, First Iteration

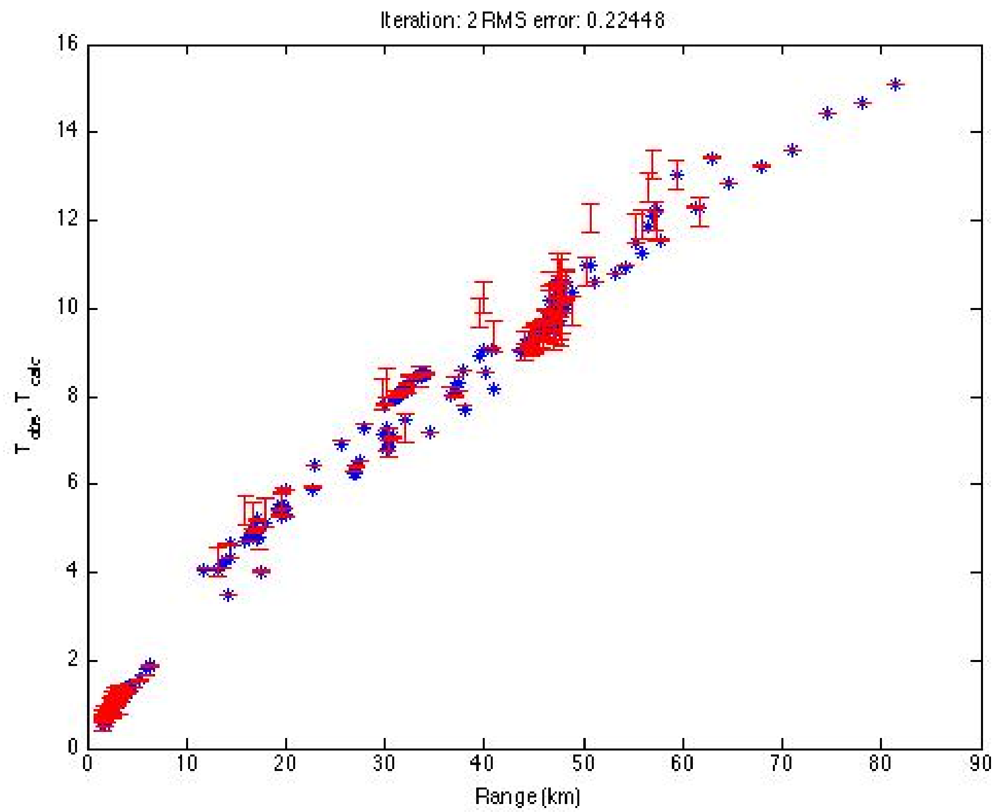

Figure F.47: RMS Error for α = 151.4196, Second Iteration

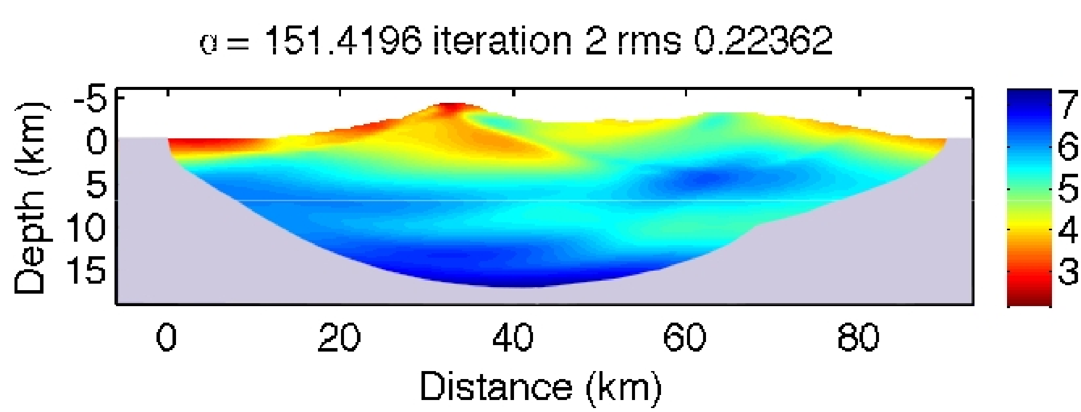

Figure F.48: Velocity model for α = 151.4196, Second Iteration

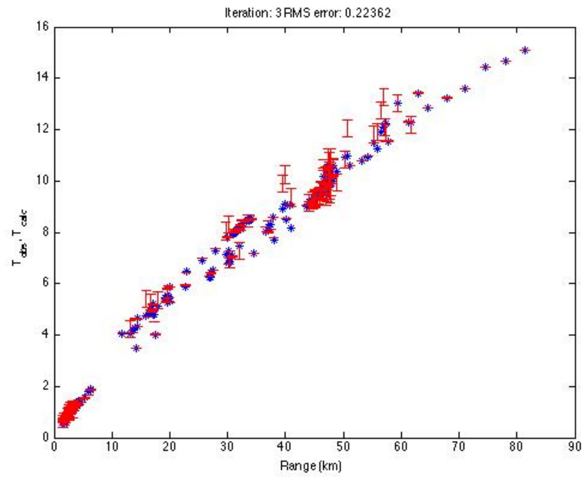

Figure F.49: RMS Error for α = 151.4196, Third Iteration

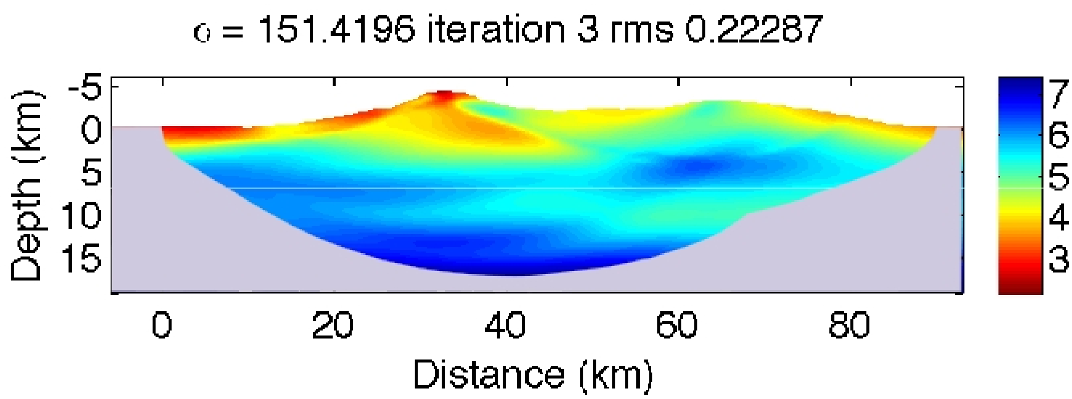

Figure F.50: Velocity model for α = 151.4196, Third Iteration

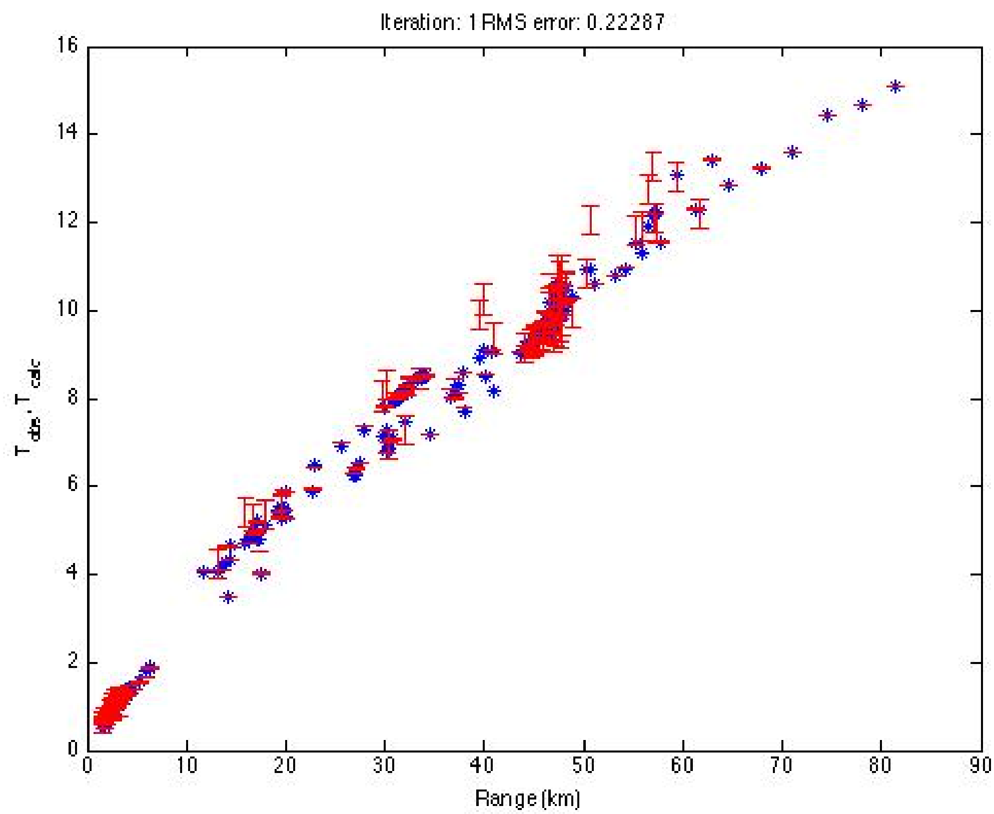

Figure F.51: RMS Error for α = 107.7181, First Iteration

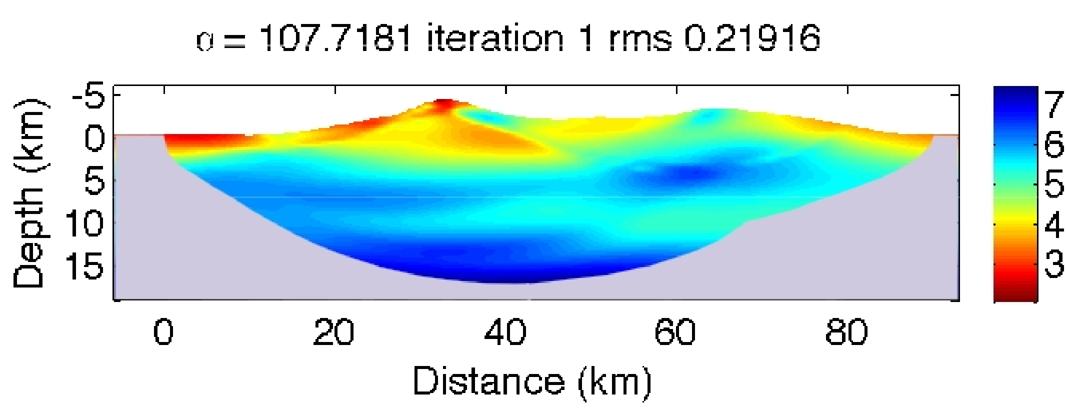

Figure F.52: Velocity model for α = 107.7181, First Iteration

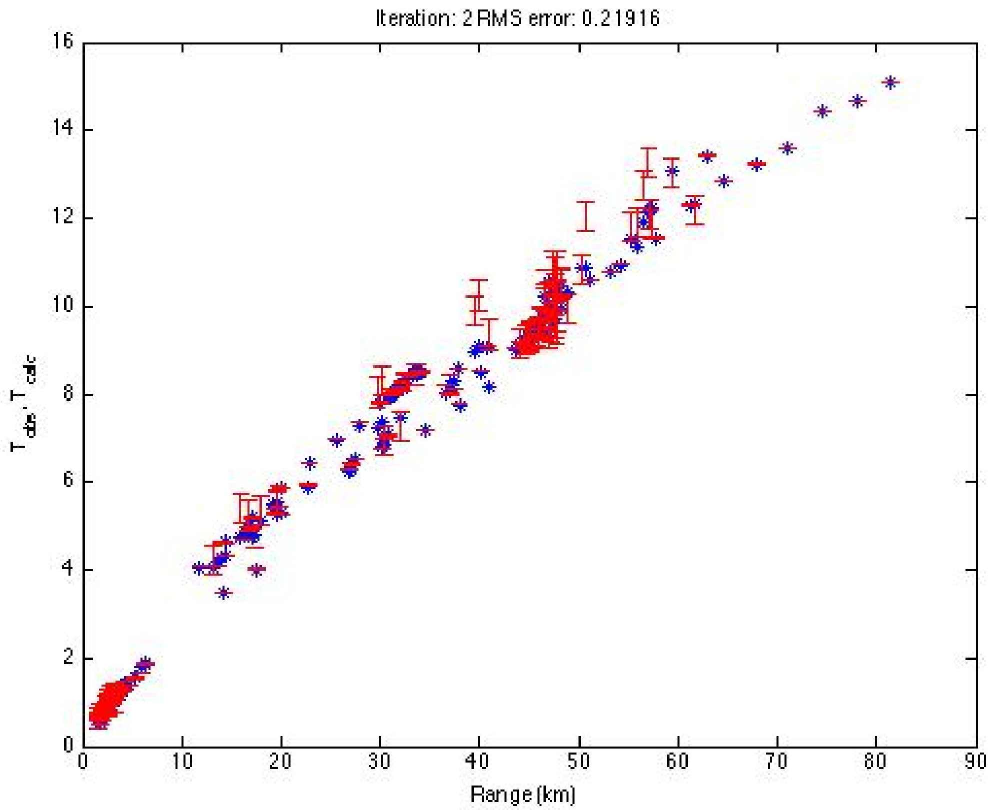

Figure F.53: RMS Error for α = 107.7181, Second Iteration

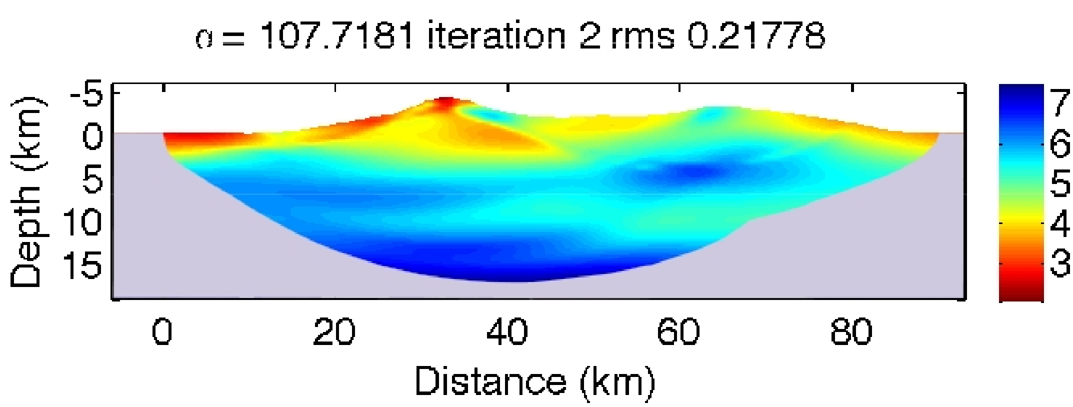

Figure F.54: Velocity model for α = 107.7181, Second Iteration

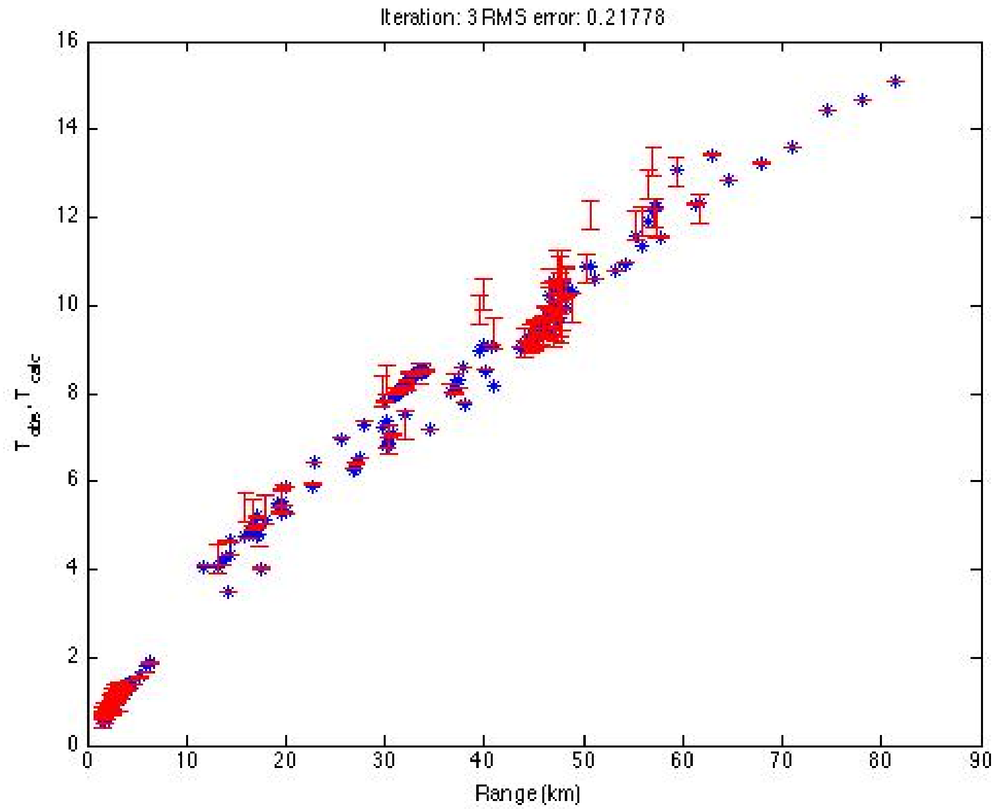

Figure F.55: RMS Error for α = 107.7181, Third Iteration

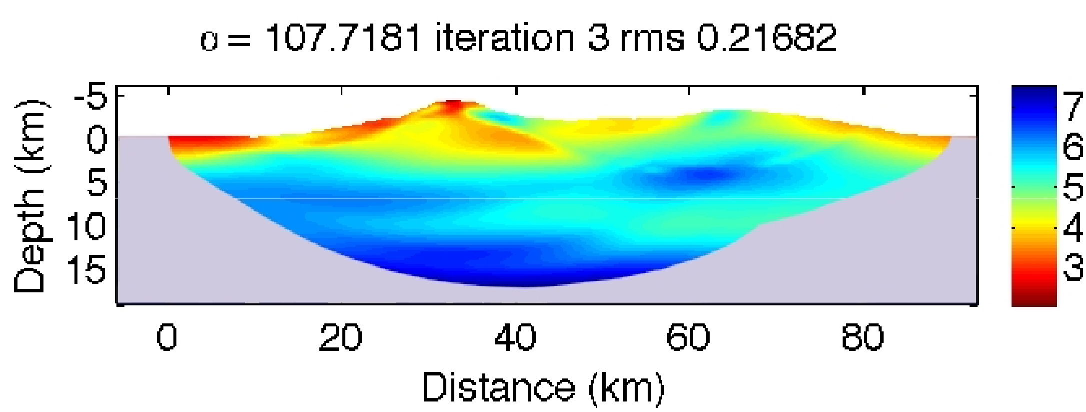

Figure F.56: Velocity model for α = 107.7181, Third Iteration

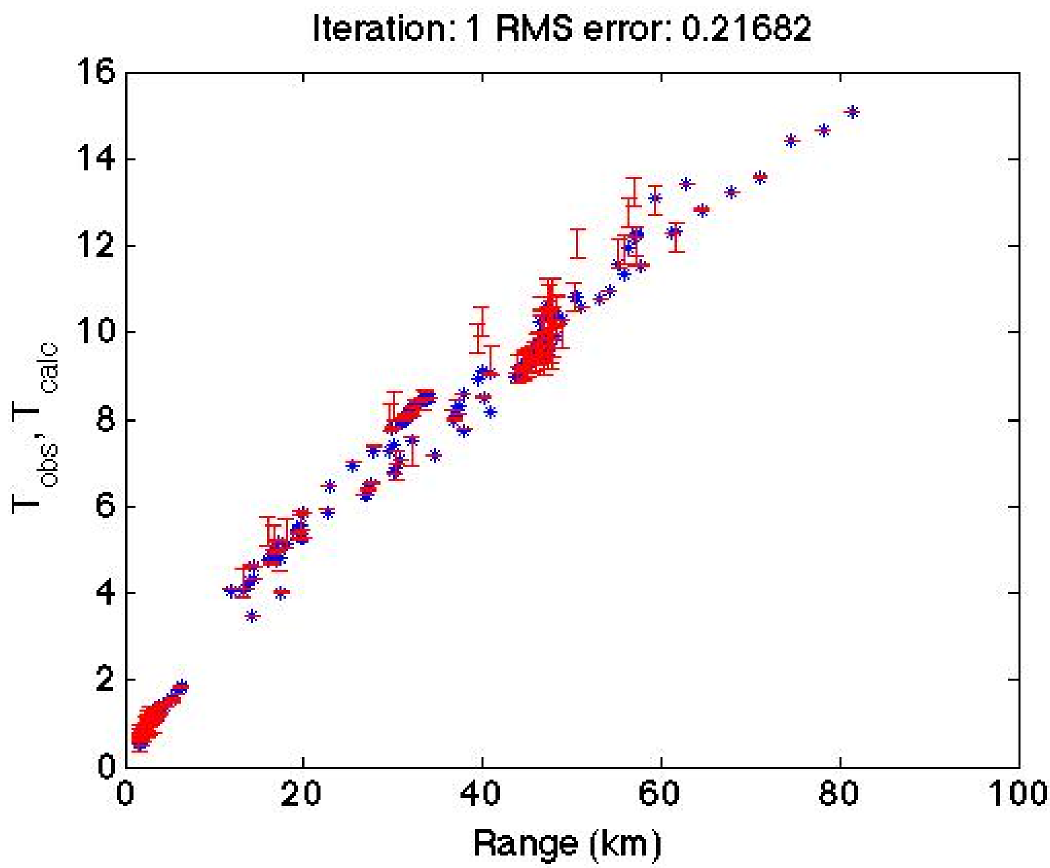

Figure F.57: RMS Error for α = 76.5233, First Iteration

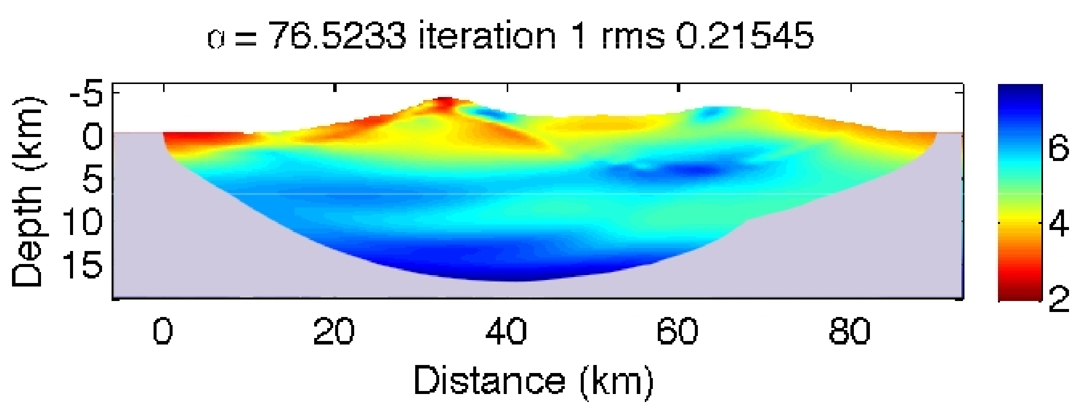

Figure F.58: Velocity model for α = 76.5233, First Iteration

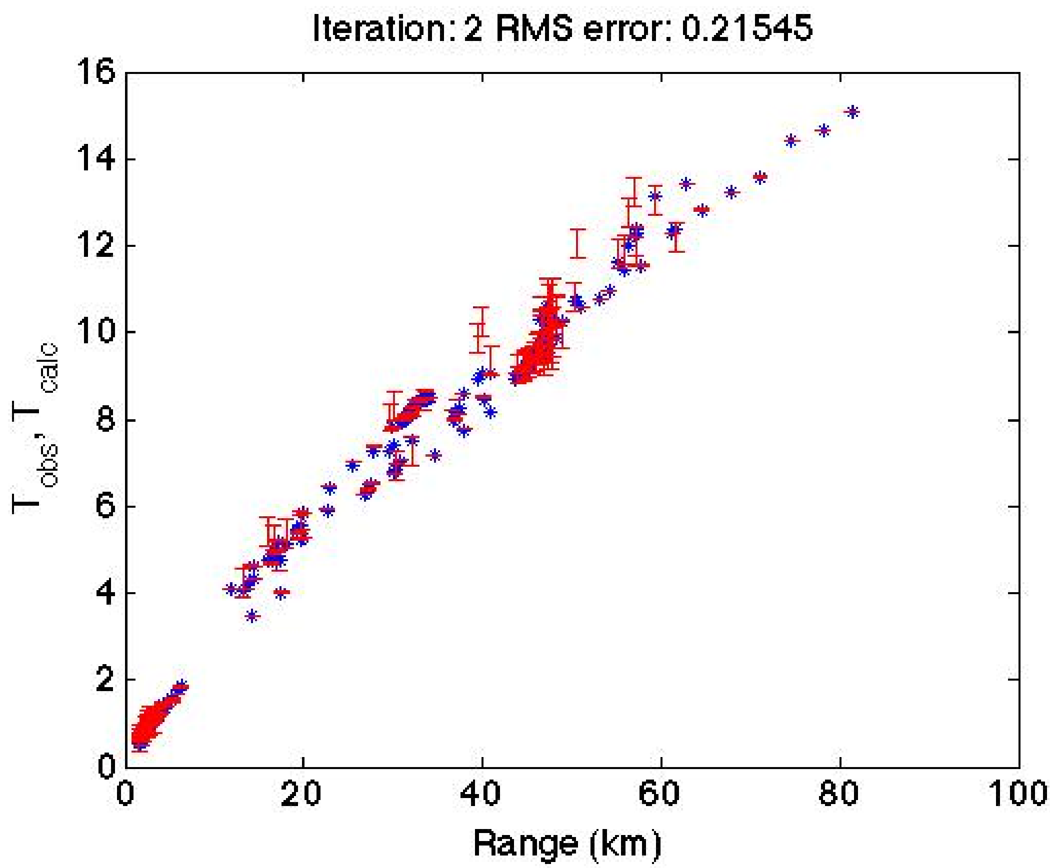

Figure F.59: RMS Error for α = 76.5233, Second Iteration

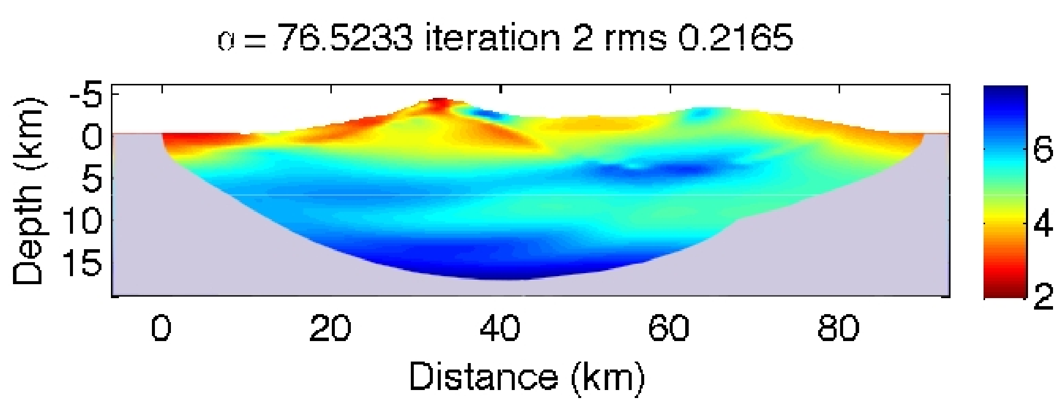

Figure F.60: Velocity model for α = 76.5233, Second Iteration

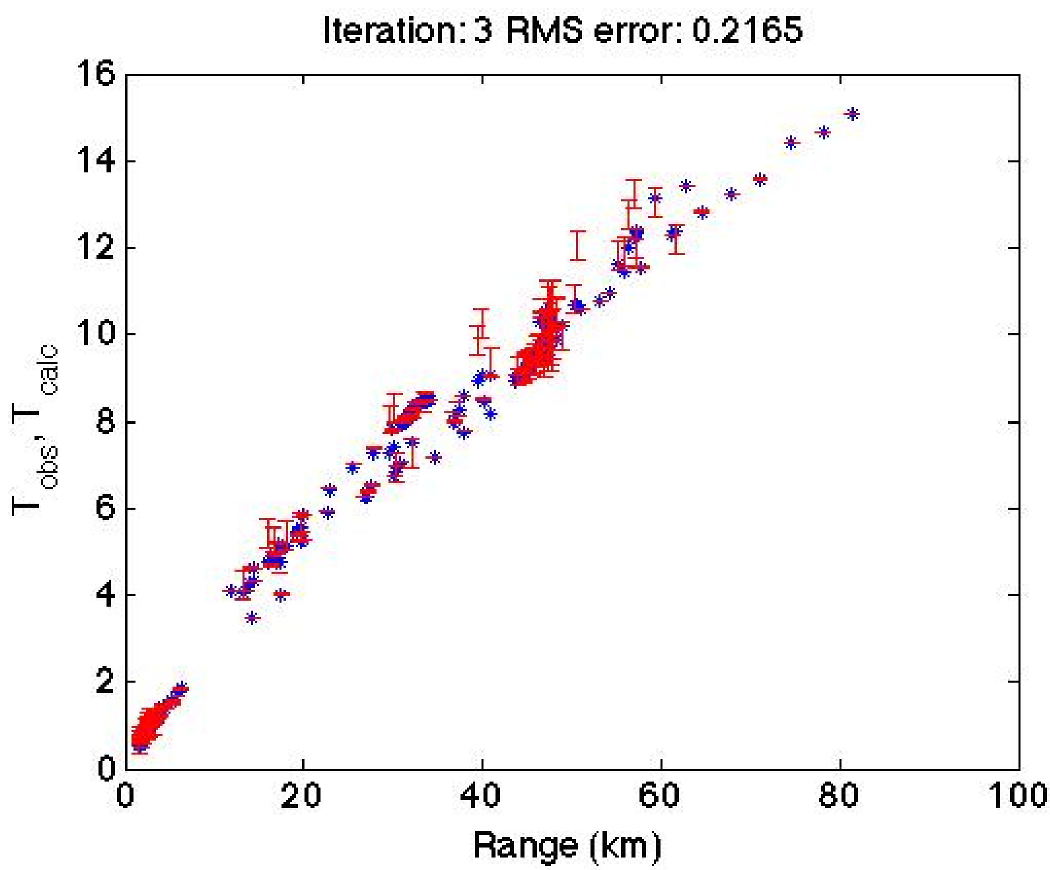

Figure F.61: RMS Error for α = 76.5233, Third Iteration

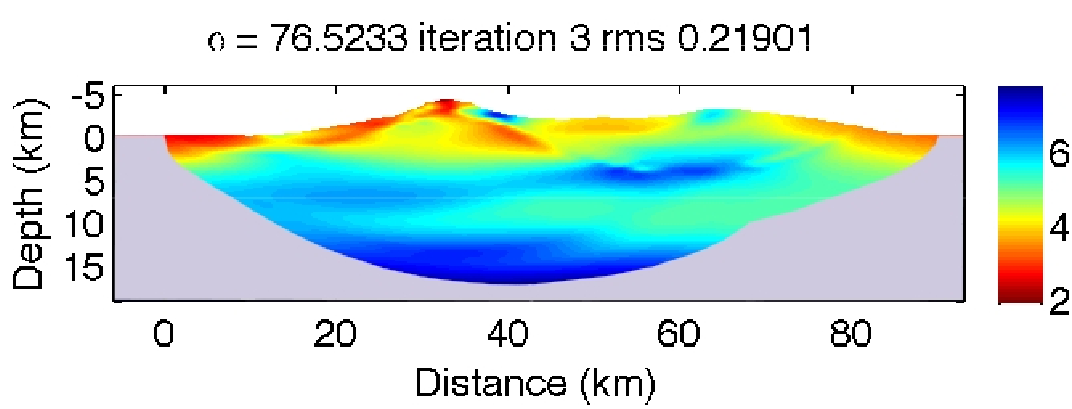

Figure F.62: Velocity model for α = 76.5233, Third Iteration